IDEA League

Master of Science in Applied Geophysics

Research Thesis

Core orientation and seismic anisotropy investigations around the COSC-1 borehole

Luisa M. Bienstein

August 11, 2016

ETH zürich

UPPSALA UNIVERSITET

Core orientation and seismic anisotropy investigations around the COSC-1 borehole

Master of Science Thesis

for the degree of Master of Science in Applied Geophysics at
Delft University of Technology
ETH Zürich
RWTH Aachen University
by

Luisa M. Bienstein

August 11, 2016

Department of Geoscience & Engineering · Delft University of Technology
Department of Earth Sciences · ETH Zürich
Faculty of Georesources and Material Engineering · RWTH Aachen University

IDEA LEAGUE
JOINT MASTER'S IN APPLIED GEOPHYSICS

Delft University of Technology, The Netherlands
ETH Zürich, Switzerland
RWTH Aachen University, Germany

Dated: *August 11, 2016*

Supervisor(s):

Prof. C. Juhlin

Dr. C. Schmelzbach

Committee Members:

Prof. C. Juhlin

Dr. C. Schmelzbach

Prof. E. Slob

Abstract

The COSC-1 drilling project in central Sweden resulted in a 2.5 km deep cored borehole with a core recovery of almost 100 % and was primarily supported by the International Continental Scientific Drilling Program (ICDP) and the Swedish Research Council. With the goal to understand the mountain building processes in the Scandinavian Caledonides a wide range of geophysical and geological investigations have been and are still being performed within this project.
This study focuses on core orientation utilising acoustic televiewer data. Subsequent seismic anisotropy investigations are based on Finite Difference modelling. The geological background model is built according to the lithological drill core description and modelled seismic properties. The main objectives were utilizing small-scale seismic measurements conducted on drill core samples and comparing the resulting synthetically modelled velocity profiles to large-scale field measurements.

The core orientation is successfully performed on core sections of interest. Geological descriptions of nearly horizontal layers in the vicinity of the borehole are supported by the oriented core scans. Sporadically occurring micro-cracks are observed but a determination of characteristics covering the complete borehole was impossible.
Numerical modelling of elastic wave propagation through an anisotropic medium represents the second part of this thesis. The subsurface around the COSC-1 borehole is characterised as vertical transverse isotropic (VTI), meaning that the axis of symmetry is in the z-direction and at the same time representing the direction of the minimum velocity. The simulated zero-offset VSP and the surface-based seismic approach result in velocity profiles with depth and offset, respectively. The comparison to large scale field measurements (high resolution zero-offset VSP and seismic tomography) implies differences in velocity and anisotropy. The simulated velocities for P- and S-waves are generally higher since the geological model is only based on modelled seismic properties, including mineralogy and rock texture of the crystalline rocks, but no micro-cracks. The field measurements indicate an influence of micro-cracks and their induced porosity. Velocities are generally lower with a subsurface including fractures. In the upper 700 m the velocities measured in the field increase gradually with increasing uniaxial pressure and corresponding closure of micro-cracks. The anisotropy of P-wave velocity is weakened by open fractures in the first 500 m since the cracks are not compressed by the overburden pressure, and introduce a more complex anisotropic symmetry. Once the cracks are closed the anisotropy is equal for the measured field data and the modelled velocities. Hence the seismic anisotropy is unaffected by closed micro-cracks but the seismic velocity is still reduced. The shear zone starting at around 1700 m is clearly identified by lower velocities in both the field measurements and the synthetic VSP.

Acknowledgements

First of all, I would like to express my sincere gratitude to my main supervisors, Chris Juhlin at Uppsala University and Cedric Schmelzbach from ETH Zurich. They were always dedicated to help and support me during the work on my project.

Secondly, I want to thank all people at Geocentrum who have participated in this project and provided information, data, and support during my time in Uppsala. Many thanks especially to Bjarne Almquist, Henning Lorenz and Peter Hedin.
Additionally, I want to mention Helge Simon (TU Bergakademie Freiberg) and Felix Krauß (GFZ German Research Centre for Geosciences - Helmholtz Centre Potsdam) for providing the datasets of the seismic tomography and high resolution VSP measurements.

I am thankful for the financial support in form of the tuition scholarship from RWTH Education Fond and DEA Deutsche Erdoel AG. It was a great support during my whole Master studies.

Uppsala University
August 11, 2016

Luisa M. Bienstein

Table of Contents

List of Figures

List of Tables

Acronyms

ABC Absorbing Boundary Condition

AGC Automatic Gain Control

CCT Central Caledonian Transect

COSC Collisional Orogeny in the Scandinavian Caledonides

DIS Drilling Information System

EBSD Electron Backscatter Diffraction (Analysis)

FD Finite Difference

FDTD Finite Difference Time Domain

HiRAT High Resolution Acoustic Televiewer

HTI Horizontal Transverse Isotropy

ICDP International Continental Scientific Drilling Program

IGSN International GeoSample Number

P-wave Compressional (or primary) wave

PDE Partial Differential Equation

S-wave Shear (or secondary) wave

Scandes Scandinavian Caledonides

VSP Vertical Seismic Profiling

VTI Vertical Transverse Isotropy

Chapter 1

Introduction and Background

In this first chapter, I provide an overview of the COSC-1 drilling project. Scientific drilling programs are introduced and their importance for the COSC-1 project is stated. Objectives of the drilling project are described and the thesis outline within this project is defined. Finally, a geological and geophysical summary is given, starting with the geology of the Scandinavian Caledonides, continuing with the local geological setting and finally describing relevant geophysical investigations which have already been conducted.

1-1 Scientific drilling and the COSC-1 project

Scientific drilling projects obtain valuable geological and geophysical data at shallow depths. Typically geophysical datasets are acquired at the surface and result in information about the subsurface, reaching various depth levels. Geological data are also collected at the surface and interpretations about the subsurface are drawn. Data acquired in a drilling campaign enable a comprehensive geoscientific evaluation and a validation of previously acquired surface data. Different infrastructures and platforms support huge drilling projects. The International Continental Scientific Drilling Program (ICDP) is one of those providing the means like operational and funding support, as well as drill facilities and data management support for conducting scientific research. In cooperation with the Swedish Research Council and other partners, the COSC-1 (Collisional Orogeny in the Scandinavian Caledonides) drilling project was performed. Understanding the Caledonian orogeny is important to understand Sweden's geological history and geomorphology.

The COSC Deep Drilling Project was planned with the goal to understand the mountain building in a detailed way, with its dynamics and orogenic processes in general. For the purpose of location decision a wide range of geophysical investigations were performed in advance. Particularly the 36 km long high resolution seismic line resulted in a 2D image of the upper few kilometers that provided detailed information on the subsurface and potential drill sites (Hedin et al., 2012). Furthermore, the 3D reflection seismic interpretation from Hedin et al. (2014) visualised tectonic structures and constrained 3D inverse gravity modelling

supported the interpretation of the Seve Nappe Complex extending no deeper than 2.5 km. After evaluation of all possibilities the COSC-1 borehole (ICDP 5054-1-A) was chosen in central Sweden close to the town Åre in western Jämtland (see Figure 1-3).

The following cross-disciplinary objectives of the COSC project are defined by Lorenz et al. (2015a) and Hedin et al. (2015). Firstly, the establishment of a coherent model of the mid-Paleozoic mountain building, in order to apply this knowledge on modern analogues, especially the Himalaya-Tibet mountain belt. The Scandinavian Caledonides are an example of an inactive mountain belt and an analogue to recently active mountain belts like the Himalaya. The emplacement of high-grade subduction-related allochthons is studied at mid-crustal levels. Furthermore, geophysical interpretations are used to clarify geological structures of the mountain belt and the origin of seismic reflections observed in the high resolution seismic profile. Information on historical climate changes since the last ice age are desired to gain knowledge about climate change at high latitudes. The last objectives are the hydrogeological research of circulation patterns in the mountain belt and analysing microorganisms in different depth levels and varying types of stratigraphy.

The COSC-1 drilling project, described by Lorenz et al. (2015b) as the drilling of a subduction-related allochthon in the Paleozoic Caledonide orogen of Scandinavia, started after a long period of previous investigations and planning with the drilling operations in May 2014 and was finished around four months later (Lorenz et al., 2015a). Down to the driller's depth of 2495.8 m, the hole was fully cored with a core recovery of almost 100 %. Due to technical circumstances, the hole diameter was reduced at a depth of 1600 m. From H-size drilling with 63 mm core and 96 mm hole diameter in the upper part, the drilling process changed to N-size drilling with 48 mm core and 76 mm hole diameter. Each core run has a length of 3 m, respectively 6 m below 1600 m (Rosberg and Lorenz, 2012), consisting of various sections. The 3 m or 6 m core runs can be divided into sections by natural fractures or due to technical reasons during drilling.
To achieve an organized documentation, the following steps summarize the processing workflow of the geological and optical logging procedure of the drill core (Lorenz et al., 2015a):

- Clean drill core
- Fit core pieces in lower half of liner
- Comparison of the top with the bottom of the previous core run → gap identification
- Measuring and marking cores and estimation of core recovery (when looking downwards, the red line is on the left)
- Optical core scan and photograph of core box (+labelling)
- Core logging
- Storage

1-2 Objectives and Outline

To investigate the structures of the Scandinavian mountain belt, as part of the Caledonian orogen, a 2.5 km deep borehole was drilled within the COSC-1 drilling project in central Sweden. The borehole was fully cored from 100 m to about 2500 m and acoustic televiewer data are available along the entire interval. Seismic anisotropy measurements have been performed on certain core sections and these sections are of particular interest. The combination of televiewer data and optical core scans allows an orientation of optical core scans which then enables a geographical relation of physical property measurements performed on the core. However, this relation will not be carried out in detail in the context of this thesis. The core orientation will allow comparison of the small-scale seismic measurements on the core with large-scale field observations. Subsequent seismic modelling represents the second part of this thesis. Modelling of wave propagation in 3D through an anisotropic medium results in synthetic data which can be compared to field measurements. A surface-based seismic acquisition and a VSP simulation allow a generation of velocity profiles.

Particularly the zero-offset VSP (Krauß et al., 2015) and the multi-azimuth walkaway VSP survey and three seismic tomography lines (Simon et al., 2016) are of interest during the comparison and evaluation, presented in Chapter 3-4. These datasets result in velocity profiles which allow the comparison to small scale core measurements. P- (and S-) wave velocity profiles of mainly horizontally and vertically travelling waves are provided in the datasets and those are additionally compared to the velocities generated after the FD seismic modelling. The combination of all datasets validates the anisotropic behaviour of seismic velocities around the COSC-1 borehole.

1-3 Geology and tectonics of the Scandinavian Caledonides

The Caledonides are one of the world's major mid-Paleozoic mountain belts (Lorenz et al., 2015b) extending from Ireland, Britain and other parts of north Europe over the Scandinavian countries to Greenland. The Caledonian orogeny is roughly classified by a beginning in the early Ordovician (490 Ma) and ending in the early Devonian (390 Ma) (Gee et al., 2008).

In the early Ordovician, the Caledonian orogeny began with the progressing closure of the Iapetus ocean, situated between the palaeocontinents of Avalonia, Baltica, and Laurentia (McKerrow et al., 2000). With proceeding closure subduction zones along both margins developed, and the continents Baltica and Laurentia collided and formed the Caledonides by the underthrusting of Laurentia by Baltica in the mid Silurian (Corfu et al., 2014b). Emplacement of the thrust took place over several hundreds of kilometres and high-grade metamorphism influenced the lithology of the allochthons. Originating from the outer parts of the continental margins, the allochthons are placed on the adjacent platform (Lorenz et al., 2015b). After more than 300 Ma of erosion and an uplift during the opening of the North Atlantic Ocean, elements of the Caledonian orogen are contained in the upper crust and partly exposed at the surface.

Presently the Caledonides are most prominently present in western Scandinavia and the eastern parts of Greenland, with East-vergent and West-vergent thrust systems, respectively (Gee et al., 2008). The Scandinavian Caledonides form a 1500 km long belt (Corfu et al.,

2014a) and are built up on top of the autochthonous crystalline basement of Precambrian age (Gee, 1975), the adjacent platform. The tectonic units (highest transport distance on top) can be divided into four groups. After Gee and Sturt (1985) the groups of the thrust sheets are the Lower, Middle, Upper and Upper-most Allochthons. Beginning in the Lower Allochthon, the grade of metamorphism increases towards the Middle Allochthon but rapidly decreases again in the overlying units, the Iapetus-derived allochthons (Gee et al., 2010). Figure 1-1 sketches the tectonostratigraphy of the Scandinavian Caledonides and the profile relates the basement (autochthon) to the allochthons.

The Seve Nappe Complex can be assigned to the upper part of the Middle Allochthon (Figure 1-1) and originates from the outer margin of the continent of Baltica (Gee et al., 2010). Since the Seve Nappe Complex is appearing in the area and depth of interest, the lithology will be described further. The lower Seve Nappe, consisting of ductilely deformed rocks from the amphibolite facies, indicates a similar lithology as the underlying Särv Nappe which shows metasandstones and dolerites as protoliths. The Seve Nappe's central and upper parts are characterized by migmatites and paragneisses, and respectively amphibolite-dominated units with psammites and mica-schists (Lorenz et al., 2015a). In northern Jämtland (Figure 1-1) the lower to middle Seve Nappe Complex of middle Ordovician age is characterized by ultra-high-pressure metamorphism (Lorenz et al., 2015b). Further south microdiamonds were found in the migmatitic gneisses of the granulite facies (Lorenz et al., 2015b). These findings have a great impact on interpretations of the orogenic events in the hinterland, where a second subduction took place in the final phase of the Scandinavian collision (Klonowska et al., 2015).

For a detailed description of the local geology, the operational report from Lorenz et al. (2015a) is used. The core recovery of almost 100 % during the COSC-1 drilling allows a precise determination of the lithology. The drill core lithology is roughly determined as primarily consisting of gneisses with varying compositions down to 1700 m. A distinction into felsic gneiss, calc-silicate and amphibole gneiss is possible and often the gneisses are garnet and diopside bearing. Between 500 m and 1000 m layers of meta-gabbros and amphibolites generate seismic reflections. Partly there are occurrences of marbles, pegmatite dykes, and mylonites found in the drill core, mainly in the lower parts. Fracture zones appear occasionally. Below 1700 m there are first indications for the thrust zone below the Seve Nappe and the mylonite thickness increases up to 1 m (1900 m to 2000 m depth) until they represent the dominating lithology below 2100 m. Mylonitized quartzites and meta-sandstones constitute the lowest part of the drillcore. A simplified core lithology is illustrated in Figure 1-2. The top 1700 m are characterized as gneisses of varying composition. Amphibole, felsic, and calc-silicate gneisses are present with varying thicknesses. The lower part contains mainly mylonitic rocks with layers of low-grade metamorphic rocks of intermediate thickness, indicating the upper boundary of the shear zone.

1-4 Relevant geophysical investigations around the COSC-1 borehole

The geophysical downhole logging operations were performed in several campaigns by Lund University and ICDP. During drilling breaks, the borehole was partly logged down to the current drillers depth and afterwards the drilling continued. This approach prevents total data loss in case of an unseen event like a hole loss that prohibits logging after drilling the complete borehole. Using this approach the acoustic televiewer images and other logs like the reference Gamma Ray log were acquired. Geophysical logging of the core was performed directly after coring and scanning the core.

The two following field measurements are the most important ones regarding this thesis. The high resolution zero-offset VSP from Krauß et al. (2015) reveals the P- and S-wave velocity of mainly vertically travelling waves. A receiver chain with 15 three-component geophones was utilised in a way that the final receiver interval was 2 m. The hydraulic hammer source (VIBSIST) was located 30 m away from the top of the borehole. The picked travel times allowed a calculation of velocity profiles which will be compared to the FD modelling results, assuming a vertical borehole.

The seismic tomography approach from Simon et al. (2016) generated three P-wave velocity profiles considering mainly horizontally propagating waves. All three lines are up to 10 km long, centred around the borehole and all approaching different directions on the surface. First arrival travel time inversion, consisting of shortest path ray tracing and a regularized non-linear inversion approach, was applied to obtain the P-wave velocity profile for each of the three lines. The study also investigated the influence of anisotropic behaviour within the seismic wave propagation. The results from different acquisition methods are explained by introducing a simple anisotropic model. Vertical transverse isotropy verifies direction-dependent velocities in wave propagation.

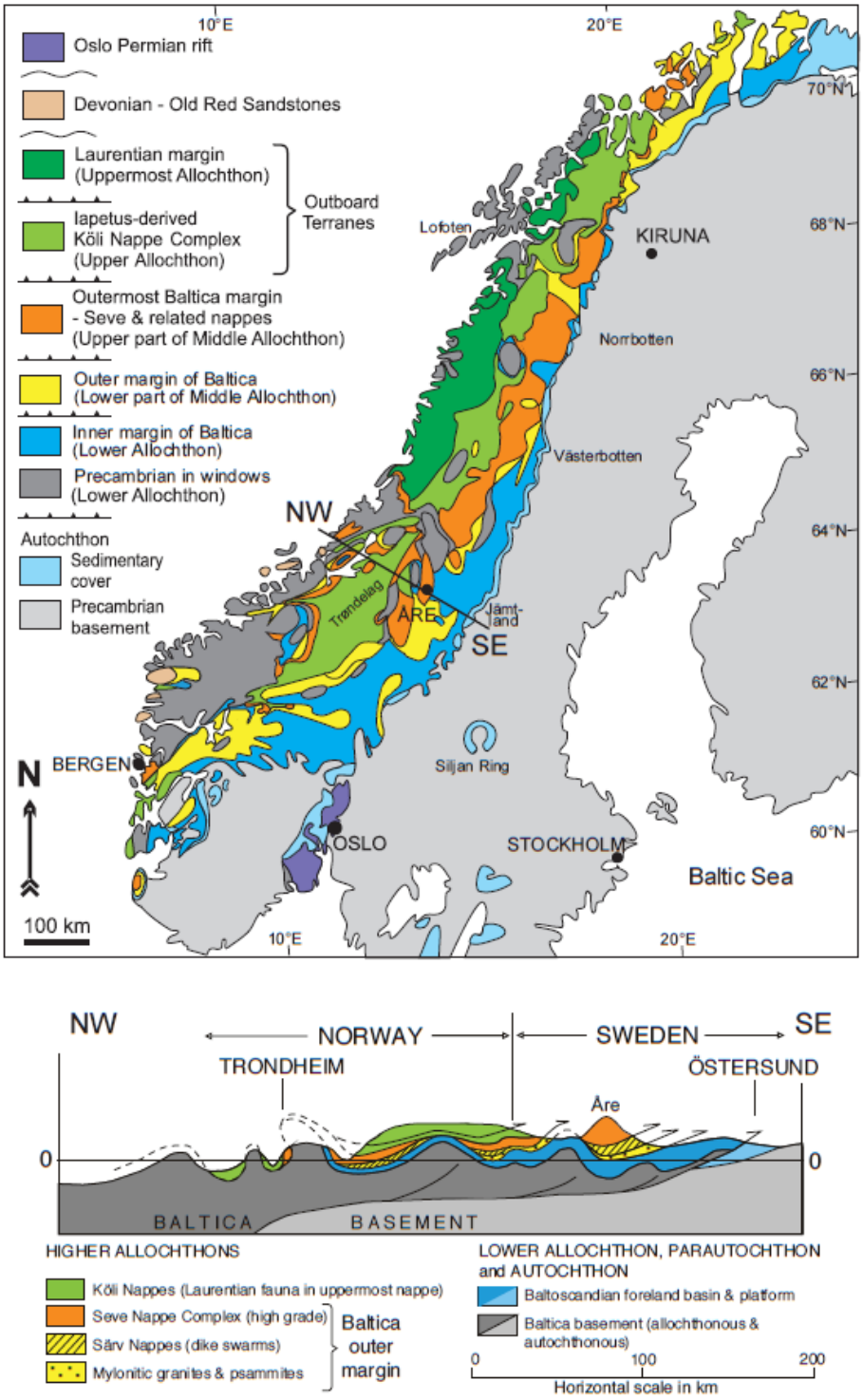

Figure 1-1: Tectonic map and schematic cross section of the Scandinavian Caledonides. The profile crosses Åre, where the COSC-1 borehole is located and is five times vertically exaggerated (adapted from Gee and Sturt (1985) and Gee et al. (2010)).

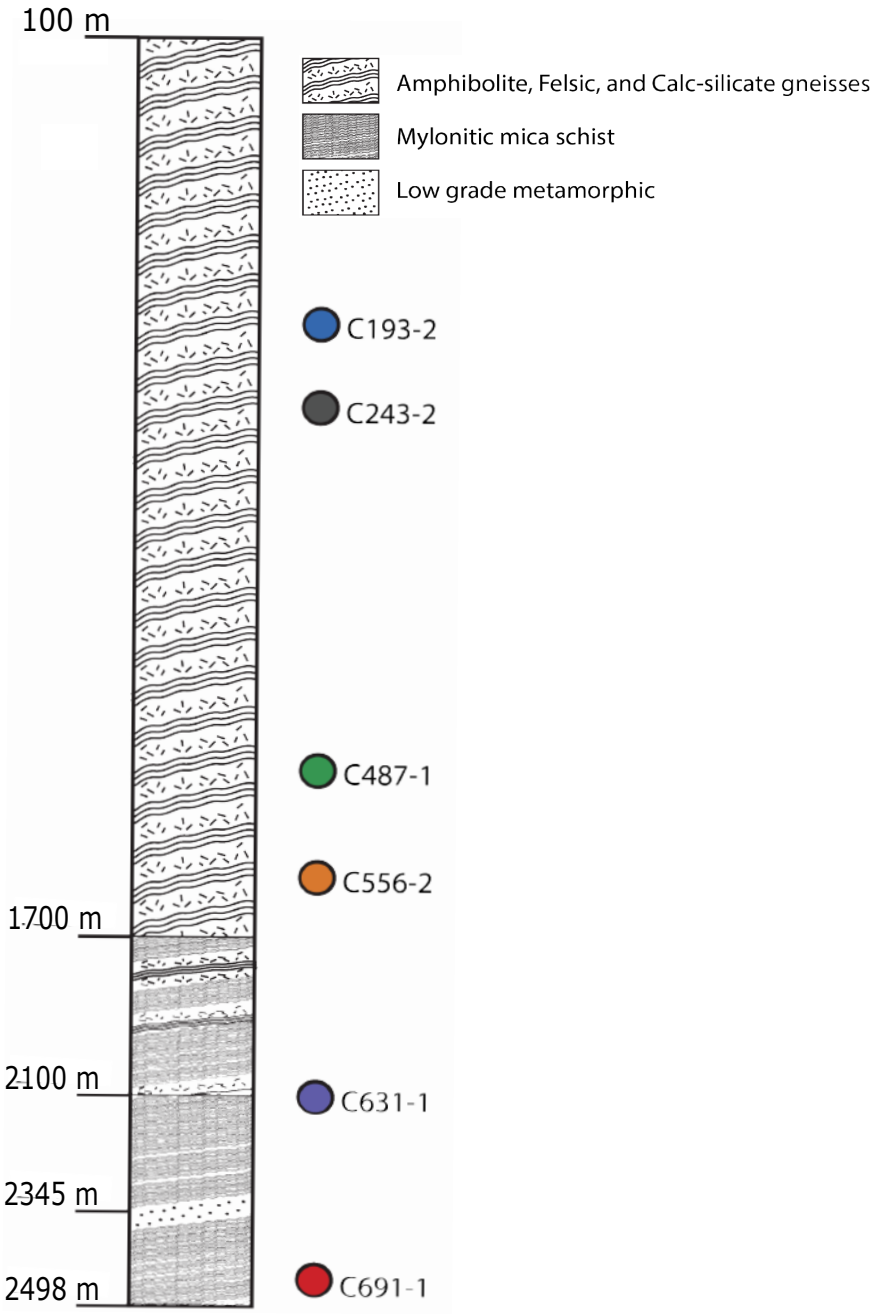

Figure 1-2: Lithology of the core adapted from Wenning (2015) and Lorenz et al. (2015a). Core samples were taken at the six marked locations for seismic anisotropy measurements as described in Chapter 3-1.

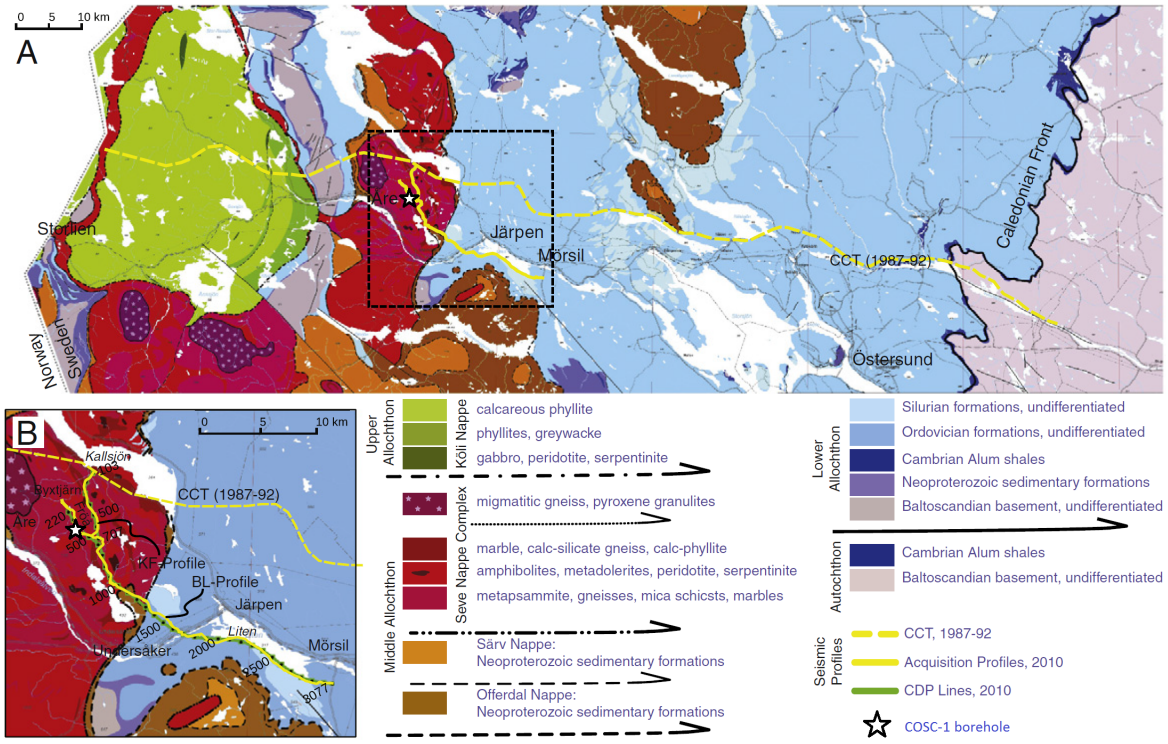

Figure 1-3: (A) Regional geology along the CCT (Central Caledonian Transect, a deep seismic reflection line across the Scandinavian Caledonides in Sweden and Norway (Hedin et al., 2012)).
(B) Local geology around the location of the COSC-1 borehole. Figure changed after Hedin et al. (2012). The maps are based on Strömberg et al. (1994).

Chapter 2

Core orientation

2-1 Acoustic televiewer data and core scans

Acoustic Televiewer

During most drilling campaigns the core recovery hardly reaches a sufficient percentage or, in other projects, a drill core is not even acquired due to high costs. A poor core recovery or drill-cuttings may provide sufficient information about lithology and composition but tectonic and structural information are not available.

Imaging the borehole wall is an essential method for identifying structures, fractures and lithology changes within the vicinity of a borehole if drill cores are not available (Gaillot et al., 2007). Different techniques of borehole imaging exist: optical televiewer (video camera), electrical televiewer (micro-electrical imagers) and acoustic televiewer (ultrasonic scanners) (Hayman et al., 1998). The acoustic televiewer acquires a sonar image of the borehole wall. 360° images showing the amplitude and travel time of the signal reflected at the borehole wall are split vertically along magnetic north. The data is oriented by the magnetometer included in the measurement device.

The first logging campaigns were realized using the High Resolution Acoustic Televiewer (HiRAT) from Robertson Geologging. Due to limitations in usage when exceeding certain pressure and temperature environments, the borehole was logged from 100 m (base of casing) to the depth of 1600 m with this device. Thus the equipment changed approximately at the boundary from the wider to the smaller borehole diameter. The televiewer data until 1600 m was acquired in 7 different campaigns, divided into 3 runs. During the first logging run within the COSC project no data was collected, but the second run resulted in images from the base of the casing down to around 1090 m. The next run acquired the data until 1465 m and the last one finally until 1610 m. Below 1610 m the logging equipment changed to the acoustic borehole imager QL43 ABI by Mount Sopris and ALT (Advanced Logic Technology).

Both acoustic televiewer sondes acquire oriented acoustic images of the borehole wall. The continuous high resolution ultrasound data consist of amplitudes and travel time images of the reflected acoustic signal. A fixed acoustic transducer and a rotating acoustic mirror generate a

focused beam, scanning the borehole wall. The travel time image log can be seen as a 360-arm caliper log, indicating the smallest deviations from the ideal borehole diameter (Geologging, 2016). Minor and major breakouts have been identified using the travel time logs (Wenning et al., 2016). The sonic wave amplitude of the reflected signal provides information about the acoustic impedance of the formation. The remaining energy of the emitted sonic pulses is attenuated by the formation (Milloy et al., 2015).
For all downhole surveys, there is one depth reference in form of a composite log of total natural gamma measurements. The *GR_DDL_Master* log is used to correct for differences in depth between different types of geophysical logs and provides the depth calibration basis for all acquired logs during the different campaigns. Since the televiewer probes also include a GR measurement device, the calibration is straightforward.

Core scans
Rolled on a DMT CoreScan3 scanner, the core sections were scanned by a line-scan camera. The scans have a spatial resolution of 10 pixels/mm and a spectral resolution of 8 bit/channel. The results of the core scanning are 360° images (TIFF and JPEG) of each core section. After completion, the unrolled core scans were transferred to the Drilling Information System (DIS). Since it was not possible to assign accurate depth information to the core scans on-site it was necessary to depth reference the image logs. Prior to this thesis, the core scans were labelled with the correct depth indication.

Both core scans and televiewer images display a three-dimensional object as two-dimensional images. Hence dipping events like fracture planes have a sinusoidal shape. Steeply dipping events are characterized by a high amplitude curve. Figure 2-1 illustrates this aspect.

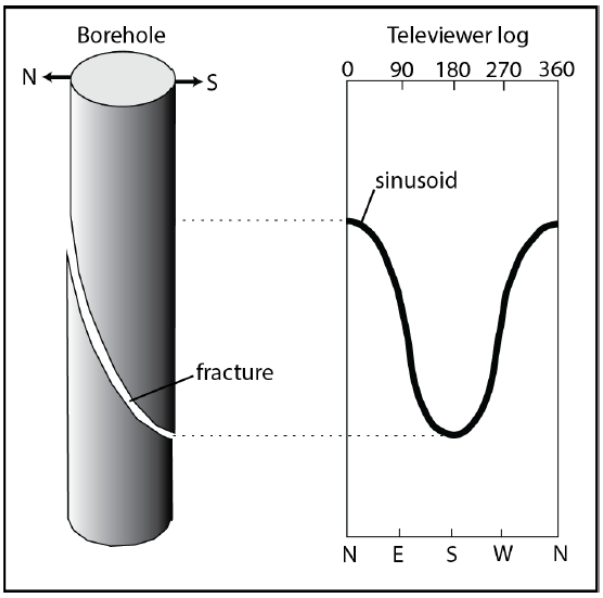

Figure 2-1: Visualization of a N-S dipping fracture zone in televiewer images after Milloy et al. (2015). The fracture plane is displayed as an oriented sinusoidal curve.

2-1-1 Theory of core orientation

WellCAD, a composite log package, is approached in areas like core description, geophysical and image logging, drilling and wellsite geology. WellCAD version v5.1 by ALT (Advanced Logic Technology) is used for the core reorientation during this study. To start with orienting the core, the amplitude log of the acoustic televiewer data is imported to WellCAD. The televiewer images are already oriented and therefore a reference for the core orientation. The core scans are imported as image logs, containing the correct depth declaration. For the purpose of this study, only the image logs of core runs which seismic property analyses have been performed on are oriented. The limited amount of time did not allow the orientation of core scans along the complete borehole. Table 2-1 summarizes the relevant sections.

Table 2-1: Core samples on which EBSD and modelling of seismic properties have been performed on.

Core run	Section (slot)
149	4
193	2
243	2
366	3
403	2
487	1
556	3
631	1
664	2
691	1

For preparation purposes, the core scan image logs are mirrored in order to correct for different perspectives while recording the data. The televiewer data was acquired within the borehole and the cores were scanned on the outside, with an 180° turn in perspective.

For both the televiewer image and the core scan a structure log is created overlying the relevant log. It enables to mark the (sinusoidal) structures in each of the logs. After marking all obvious structures, two values can be determined. Firstly the dip angle of the structure and secondly the azimuth (dip direction). Comparing both logs the dip angle should theoretically be consistent since a different dip direction does not have an impact on the angle. The azimuth of the structure in the core scans is then compared to the one of the televiewer image and afterwards manually adjusted by rotating the image log. The difference in drillhole and core diameter explains the variation in amplitude of the sinusoidal structures between the televiewer and core scan images.

When no characteristic features appear in the section listed in Table 2-1, the scans of all four to six sections for the corresponding core run are oriented. Starting with the ones containing

the most striking features, the weaker signals are used for verifying the results afterwards. The boundary between 2 sections can be used as a reference revising the results. Only core sections with no structural features are oriented along the boundaries with respect to the adjoining sections. Following this procedure, the results should be considered with least confidence.

2-2 Core orientation results

Reorientation of core scans delivers important information regarding tectonics, structure, and lithology (Ureel et al., 2013). Indicating only changes in amplitude (and travel time), the acoustic televiewer data provides changes in structure but no direct lithology identification. In fact, different lithologies have different surface characteristics which change the amplitude of the reflected ultrasonic signal but no specific identification of the lithology type is possible.

Figure 2-2 depicts those changes in lithology. Between 1688.8 m and 1689.9 m the lithology including texture, color and composition varies. The photograph of the core clearly shows various transitions from brighter to darker (more mafic) rocks. The different types can be observed with the acoustic televiewer as changes in amplitudes from higher to lower amplitudes. Although there are changes in amplitude the lithological type can not be identified with considering the televiewer image individually. Only the combination with optical scans allows a distinct classification. This shows the importance of combining different datasets and illustrates disadvantages of using certain methods individually.

Furthermore, the same figure demonstrates the weak points of the televiewer data when interpreted without any other reference. In a depth of 1688.64 m, there is a clear lithology change in form of a thin band that is producing only extremely minor changes in amplitude. When the televiewer images would be the only source for lithology identification, the rock would be classified as homogeneous. This is obviously a misinterpretation due to incorrect information from the amplitude log.
Assuming these structures would be the only ones existing in a particular depth interval, the core orientation would be impossible. Without having at least one prominent structure in both, the televiewer and the core scans, it is almost not possible to orient the core scans. It might be possible to utilize core sections with some distance, but the orientation along the core run boundaries gets increasingly unconfident and imprecise. Fortunately all core sections of interest that contain a sample for seismic measurements present at least one structure that is characterized by at least a medium confidence. This means that there are structures visible in both the core scan and the televiewer image and one is able to pick them.

Figure 2-3 gives an impression about the orientation procedure. The structure log within the oriented televiewer image indicates the true dip and azimuth of the structure. The feature at a depth around 513.7 m is characterized by dip direction of 198° and a 68.56°. The non-oriented structure in the core scan shows values of 336.94° and 67.65°. The angle of rotation (the difference between both dip directions) is 138.94°. The next core section begins already at 513.82 m and had to be rotated for 5.17° only. Clearly, the angle of rotation is arbitrary, even within a single core run. The reference lines (blue and red) do not always show a consistency since the core sections move on the geological working table while marking and scanning. Summarized, the orientation around core section 149-4 was performed with high confidence due to the presence of defined features like micro-cracks.

Problems appeared when picking structures in the televiewer log of core run 403. The structures are not consistent and appear quite noisy. In opposite to the unclear image, the core scans show regularly but slightly dipping banded gneisses. Hence a correlation is challenging. Due to the very fine bands within the gneiss, the televiewer is most likely not able to resolve those properly and the signal gets irregular. Still, it was possible to pick a few events to enable a fairly good orientation, although the accuracy of the results needs to be treated with

caution. Similar difficulties appeared at core run 691 (Figure 2-4. Only in the last section, there is a feature to pick with a medium confidence. Since the rest of the run appears without any distinct sinusoidal structures, the remaining orientation was performed along the section boundaries after orientating the lowest section manually.

The other oriented sections are not exemplified in the thesis. They mainly show the same characteristics as the examples given in Figures 2-2 to 2-4. It was always possible to pick at least one feature with satisfying confidence. This results in a finalised core orientation of ten core runs.

The main conclusions are stated as follows. Both the acoustic televiewer log and the core scans lead to the conclusion that the bedding of the layers in the depth levels of the chosen samples is fairly horizontal. This reflects the overall situation of the lithological setting around the COSC-1 borehole and will be an important fact to be considered during subsequent seismic anisotropy investigations. The horizontal foliation is only interrupted by steeper dipping fractures, cracks or similar features. These features can be observed particularly in Figure 2-3 whereas the fairly horizontal foliation is visible in Figure 2-2 of core run 556 and in core run 691 (Figure 2-4).

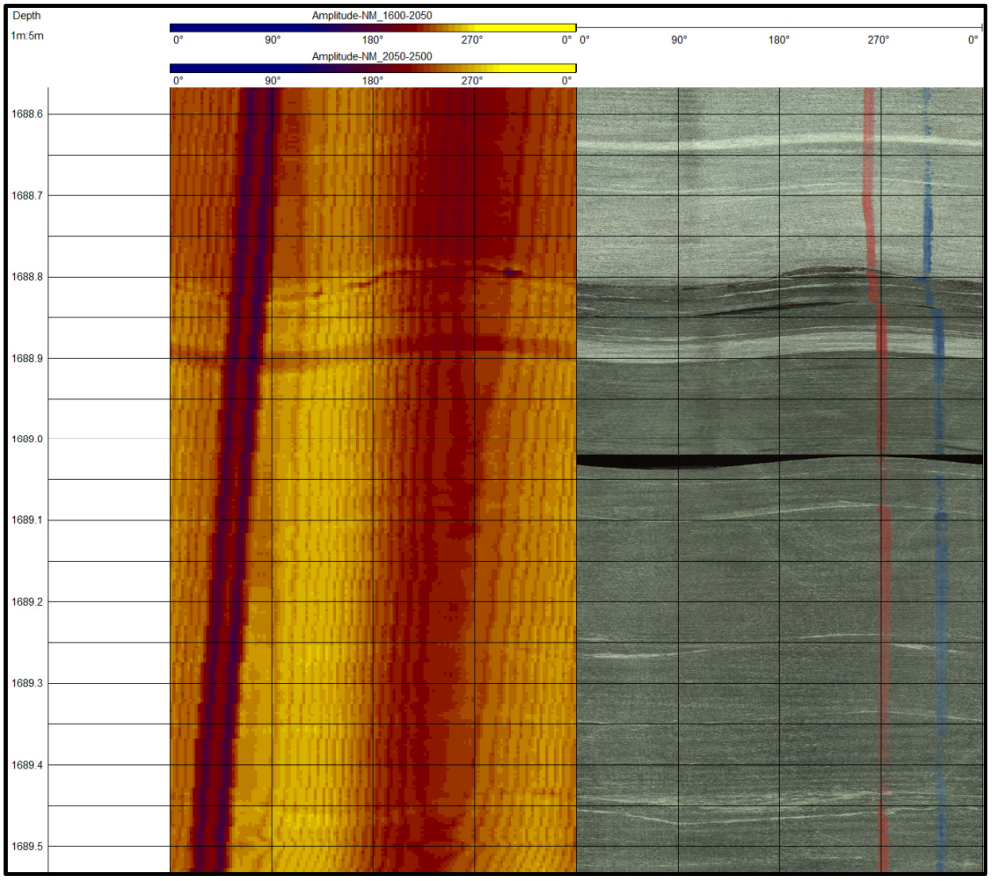

Figure 2-2: Detail of oriented core run 556 in WellCAD. Main changes in Lithology (see color changes in the core scan) can also be observed qualitatively in the acoustic televiewer data. From left to right: Depth, Amplitude of acoustic televiewer, oriented core scan.

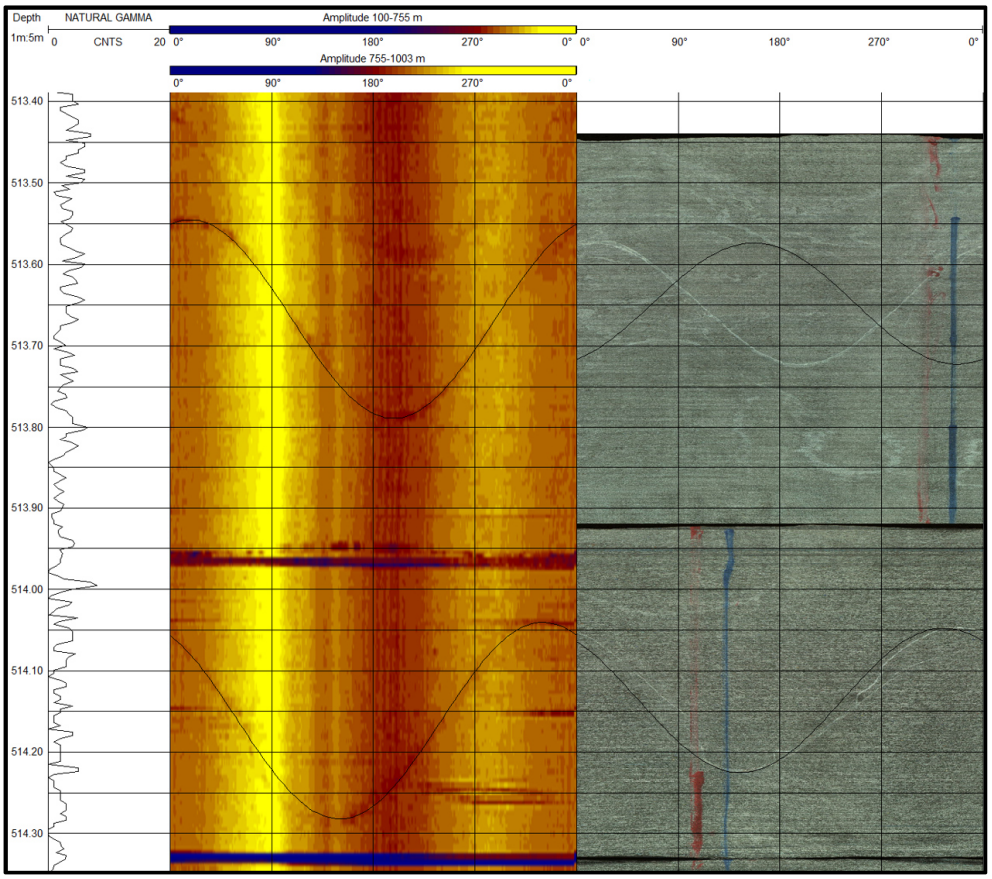

Figure 2-3: Detail of oriented core run 149 in WellCAD. The structure logs (black lines) show the structures in the oriented televiewer and the structures in the core before orientation. From left to right: Depth, Master Gamma log, Amplitude of acoustic televiewer, oriented core scan.

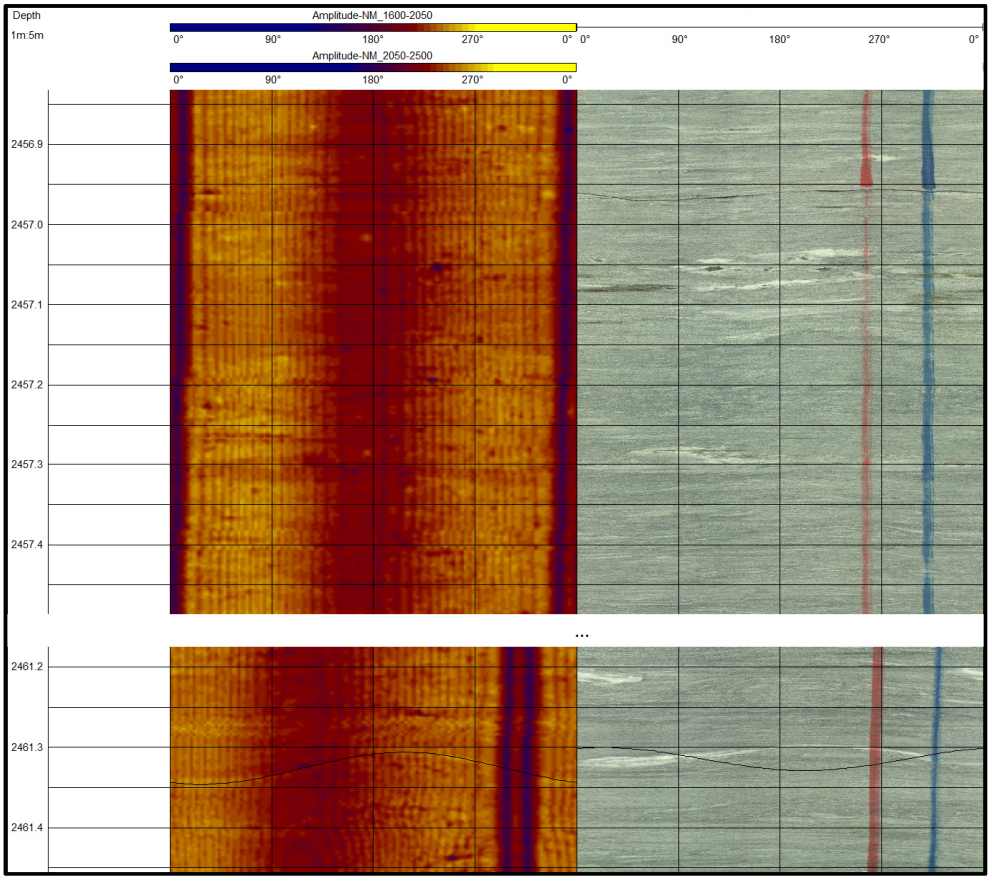

Figure 2-4: Detail of oriented core run 691 in WellCAD. Only one fairly weak feature was orientable (2461.3 m). From left to right: Depth, Amplitude of acoustic televiewer, oriented core scan.

2-2-1 Quality control of automatic core orientation device

During drilling, an automatic drill core orientation tool was tested. For the lowest sections, the Devico Devidrill BBT device (R&D collaboration) oriented the core. Around 20 runs were oriented by using the gravity field. Each extracted core section is marked manually and the orientation (ranging from $0° - 360°$) is noted. The last section from table 2-1 was oriented manually approaching the procedure explained before (in WellCAD). Thereafter the result is compared to the values from the automatic orientation device. The mark is visible in the core scan and is measured manually in WellCAD after reorientation.

691-1 is the sample that has been oriented manually and with the orientation device. The comparison of both methods gave exactly the same result. Only a few tenth of degrees difference is rather accurate, considering that one of the methods is executed manually with identifying structures just by eye. Also, the marked point at the end of the core section after automatic orientation introduces inaccuracies since the mark already is a few tenth of degrees thick. Summarized, both methods result in a surprisingly great consistency.

After this satisfying match the remaining core sections of the lower part of the borehole were firstly oriented manually in WellCAD and then compared to the automatic orientation results. Unfortunately, the consistency can not be confirmed. Not a single comparison lead to the same value. Excluding any regularities in the difference between automatic and manual orientation, the orientation in WellCAD was set as trustworthy, since the optical evidence and documentation clearly demonstrates a well performed orientation of the core scans. The variations between both methods appear randomly distributed and the first guess of a systematic error was eliminated. At this point, there are no explanations about reasons for the presumably incorrect automatic orientation.

Chapter 3

Seismic anisotropy investigations

3-1 Theory: Elastic seismic modelling through anisotropic media

A variety of rock property investigations have been performed on sections of the COSC-1 drillcore in advance. Anisotropic behaviour in seismic properties was observed and measured during those studies. Certain representative core sections have been selected in order to measure P- and S-wave velocities in different directions to determine the seismic anisotropy of major lithologies. Since the lithology of the area shows lineation and foliation perpendicular to each other, velocities were measured in three orthogonal directions. The x_3 direction is perpendicular to the foliation of the rock and additionally there are two samples taken in parallel to the foliation. The x_1 direction is parallel to the lineation and hence x_2 is perpendicular to the lineation (Wenning et al., 2016). The studies from Wenning et al. (2016) stated P-wave velocity anisotropies between 3 % for the calc-silicate gneiss and 19 % for the mica-schist. The velocity measurements on core samples under different pressure conditions show that the velocities approach a constant value with increasing pressure. Fractures close and the anisotropic velocity is only defined by the (invariant) crystal orientation. The anisotropy in S-wave velocity is 2 % for the calc-silicate gneiss and reaches a maximum of around 20 % in the mica-schist.

In general, it is legitimate to consider a vertical transverse isotropy (VTI) without velocity differences in the horizontal plane (Wenning, 2015; Simon et al., 2016). This symmetry assumes that the medium for wave propagation is horizontally layered without azimuthal changes of velocity parallel to the layering. Thus there are two different directions with x_3 being the axis of symmetry. Generally, the velocities along this axis are the slower ones since the direction of wave propagation is perpendicular to the foliation. Directions x_1 and x_2 are parallel to the foliation, both showing the same velocity. They are characterised by a faster propagation than the waves propagating in the x_3-direction. However, a few samples, like the amphibolite, show a tendency to orthorhombic behaviour regarding seismic anisotropy, with different velocities in x_1 and x_2. Since those differences in x_1 and x_2 are minor even in that case, the whole lithology is finally characterized to be vertical transverse isotropy. This will be taken into account during the anisotropic seismic modelling.

For the following simulations, the results from Wenning et al. (2016) are not utilised but modelled seismic properties that are determined mainly from the crystal orientation and mineral composition. The dataset is listed and explained in more detail later following in Chapter 3-2-1. The VTI-symmetry is already considered and only the fastest and slowest velocities are defined for each wave. Velocities are modelled for each main lithology occurring in the area of interest and used to build the geological model.

With an exception of the mica-schist the anisotropy for both, P- and S-wave velocity, remain below 20%. 10 % - 20 % anisotropy specifies the case of weak anisotropy after Thomsen (1986). Following Wenning et al. (2016) the mica-schist reaches 24 % anisotropy for the shear wave. All other lithologies remain below the boundary value and although the mica-schist exceeds 20 % the weak anisotropy is assumed to be valid for the entire subsurface model. Respecting that assumption, equations simplify considerably for establishing the elastic behaviour, including a calculation of the Thomson parameters. Equations and relations will be declared in the next sections.

The open-source software package *Madagascar* is used in this part of the thesis. Its main attention on multidimensional data analysis and reproducible computational experiments is especially suitable for the purpose of this work. Mainly focusing on geophysical, approaches the program delivers a wide range of applications, particularly in seismic modelling and imaging.

3-1-1 Elasticity of anisotropic media

The elastic wave equation is utilised when modelling the seismic wave propagation in anisotropic media (Weiss and Shragge, 2013). Preliminarily to deriving the equation of motion for elastic wave propagation, additional equations and relations need to be considered. The elastic behavior is derived from the general form of Hooke's law as given in Equation 3-1 (Juhlin, 1995; Mavko et al., 2009; Danek et al., 2000).

$$\sigma_{ij} = c_{ijkl}\epsilon_{kl} \tag{3-1}$$

with σ_{ij} describing the stresses and ϵ_{jl} being the stains in the medium. Another formulation for the elements of the linear stress tensor is $\epsilon_{kl} = \frac{1}{2}[\partial_k u_l + \partial_l u_k]$ where u stands for the wavefield displacement (Weiss and Shragge, 2013). The 81 constants c_{ijkl} in the elastic modulus tensor describe the elasticity of a medium (Thomsen, 1986). Taking the advantages of symmetry and the Voigt recipe, the tensor is simplified to a 6 x 6 matrix $c_{\alpha\beta}$ (Thomsen, 1986). For different media with changing anisotropic behaviour the number of independent constants within $c_{\alpha\beta}$ changes. Following Upadhyay (2004) the general form of $c_{\alpha\beta}$ contains 36 independent components. Simplified for a medium with vertical transverse isotropy the matrix can be degraded to the following form given in Equation 3-2 (Mavko et al., 2009). From 81 independent constants in the most general form the symmetry reduces the number to only 5 independent constants.

$$c = \begin{bmatrix} c_{11} & c_{12} & c_{13} & 0 & 0 & 0 \\ c_{12} & c_{11} & c_{13} & 0 & 0 & 0 \\ c_{13} & c_{13} & c_{33} & 0 & 0 & 0 \\ 0 & 0 & 0 & c_{44} & 0 & 0 \\ 0 & 0 & 0 & 0 & c_{44} & 0 \\ 0 & 0 & 0 & 0 & 0 & c_{66} \end{bmatrix} \tag{3-2}$$

With Equations 3-3 the 5 independent values can be determined. Entry c_{12} is not independent, in fact, it is to be calculated considering c_{11} and c_{66}. Different velocity measurements enable to calculate the remaining 5 constants, applying the relationships

$$\begin{aligned} c_{12} &= c_{11} - 2c_{66} \\ c_{11} &= \rho V_P^2(90°) \\ c_{12} &= c_{11} - 2\rho V_{SH}^2(90°) \\ c_{33} &= \rho V_P^2(0°) \\ c_{44} &= \rho V_{SH}^2(0°) \\ c_{13} &= -c_{44} + \sqrt{4\rho^2 V_{P(45°)}^4 - 2\rho V_{P(45°)}^2(c_{11} + c_{33} + 2c_{44}) + (c_{11} + c44)(c_{33} + c44)} \end{aligned} \tag{3-3}$$

Figure 3-1 visualizes the elasticity matrix for a VTI medium. The first quarter characterises the anisotropic behaviour of the P-wave velocity v_P whereas the last quarter denotes the v_S anisotropy.

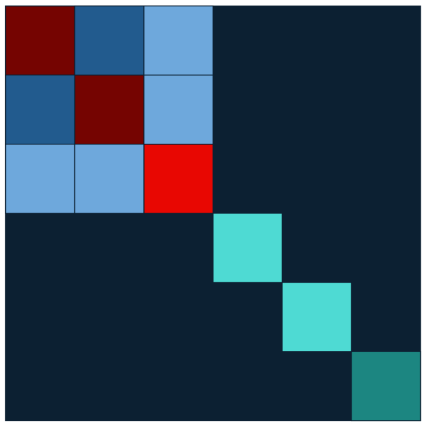

Figure 3-1: Visualisation of the 36 component elasticity matrix for VTI media (Equation 3-2). Entries of equal color specify the same value. For instance, the dark red represents c_{11} and c_{22}, which are in fact equalised for the vertical transverse isotropy.

Thomsen parameters, named after Thomsen (1986) and characterising the magnitude of anisotropy (Tsvankin et al., 2010), are valid for weak anisotropic media. The first parameter ϵ describes the fractional difference between horizontal and vertical P-wave velocity of a medium and hence expresses the P-wave anisotropy (Equations 3-4. Secondly, γ expresses the fractional difference for the SH-wave propagating parallel and perpendicular to the symmetry

axis. This is equivalent to using the S-wave propagating in the direction of the symmetry axis, once polarized parallel and the other time orthogonal to the axis of symmetry. The third parameter, δ, does not give such an illustrative interpretation, however, it contributes to P-wave velocity variations in near vertical direction and the SV-waves angular dependency in velocity (Mavko et al., 2009).

$$\begin{aligned} \epsilon &= \frac{c_{11} - c_{33}}{2c_{33}} \approx \frac{V_P(90°) - V_P(0°)}{V_P(0°)} \\ \gamma = \frac{c_{66} - c_{44}}{2c_{44}} &\approx \frac{V_{SH}(90°) - V_{SV}(90°)}{V_{SV}(90°)} = \frac{V_{SH}(90°) - V_{SH}(0°)}{V_{SH}(0°)} \\ \delta &= \frac{(c_{13} - c_{44})^2 - (c_{33} - c_{44})^2}{2c_{33}(c_{66} - c_{44})} \end{aligned} \tag{3-4}$$

Having all parameters that describe the anisotropic behaviour of the medium, the elastic wave equation is needed to simulate the wave field propagation within that medium. Equation 3-1 and the relationship $\epsilon_{kl} = \frac{1}{2}[\partial_k u_l + \partial_l u_k]$ can be combined together into the equation of motion:

$$\rho \partial_t^2 u_t = \partial_j \sigma_{ij} + F_i \tag{3-5}$$

where u_t is the wave field displacement at a certain time step t and F_i represents the body force per unit volume.

3-1-2 Numerical modelling

Numerical modelling in geophysics is a forward problem and the response towards a defined model can be predicted. A synthetic geological model is created and the theoretical process of wave propagation is simulated. Results as developing wave fields at distinct times and the recorded synthetic seismograms are used in research and exploration of elastic or acoustic wave propagation.

Finite Difference method

Introducing Finite Differences (FD), the equations in Chapter 3-1-1 are discretized and a numerical solution is implemented. With the capability of solving Partial Differential Equations (PDEs) and thus providing accurate numerical solutions, Finite Differences are a robust and widely applied numerical modelling method. A Finite Difference Time Domain modelling scheme is applied by approximating differential equations by approximating its derivatives.

A truncated Taylor series expansion is the most straightforward procedure for expressing derivatives numerically. The derivative $\partial_x f(x)$ is approximately

$$\partial_x f(x) \approx g[f(x + \Delta x) - f(x - \Delta x)] \tag{3-6}$$

for a second order accurate solution with a grid spacing of Δx. In order to have a convergence to the analytical solution of $\partial_x f(x)$ when $\Delta x \to 0$, the scalar coefficient g is chosen in a suitable way. The Taylor series centred around x (second order) yields to the expression

$$g[f(x+\Delta x) - f(x-\Delta x)] = g[2\partial_x f(x)\Delta x + \frac{2}{3!}\partial_x^3 f(x)\Delta x^3 + ...] \tag{3-7}$$

where g is chosen to be:

$$g = \frac{1}{2\Delta x}. \tag{3-8}$$

Following Fichtner (2011) the general form of a 2^{nd} order accurate central difference stencil in one dimension is formulated as in equation 3-9. The first derivative of $f(x)$ with respect to x is approximated by taking the difference between the two neighbouring points of x and dividing the result by its spatial difference.

$$\partial_x f(x) \approx \frac{f(x+\Delta x) - f(x-\Delta x)}{2\Delta x} + \mathcal{O}(\Delta x^2) \tag{3-9}$$

Valid for centred differences of variable orders the generalised equation 3-6 is valid for A grid points around x and g being variable, depending on the order of accuracy.

$$\partial_x f(x) \approx \sum_{\alpha=1}^{A} g_\alpha [f(x+\alpha\Delta x) - f(x-\alpha\Delta x)] \tag{3-10}$$

Numerical grid and implementation in the FD code

The computational grid defines the numerical framework and formulated as N_x x N_y x N_z, with a total amount of N_t time steps. In Cartesian coordinates one grid point location within the computational grid at a certain time is accordingly discretely defined as $[x, y, z|t] = [p\Delta x, q\Delta y, r\Delta z|n\Delta t]$, where the integer counters range from the first to the last grid point, e.g. $p = 1, N_x$. Hence $u_i\ |_{x,y,z|t} \approx u_i^{p,r,q|n}$ describes the wave field displacement on the discretized grid (Weiss and Shragge, 2013; Moczo et al., 2007).

This fairly straightforward scheme, given in 3-10, is then applied to the partial differential equation describing the wave field propagation. Equation 3-5, describing the wave propagation, needs to be discretized to be furthermore implemented in the modelling code. Therefore the first derivative of the displacement (right-hand side) is approximated by a centred difference approach which delivers an 8^{th} order accurate solution. The following equation represents the solution for the derivative with respect to x (in 1D).

$$\partial_x u_j \approx D_x[u_j^{p,q,r|n}] = \frac{1}{\Delta x}\sum_{\alpha=1}^{4} W_\alpha (u_j^{p+\alpha,q,r|n} - u_j^{p-\alpha,q,r|n}) \tag{3-11}$$

In this equation W_α contains the polynomial weights $\mathbf{W} = [\frac{4}{5}, \frac{-1}{5}, \frac{4}{105}, \frac{-1}{280}]$ (Weiss and Shragge, 2013; Fichtner, 2011) resulting from the approximation of the derivatives. The second time derivative is again approximated in a centered difference approach with a simple 2^{nd} order accuracy.

$$\partial_{tt}^2 u_j \approx D_{tt} u_j^{p,q,r|n} = \frac{1}{\Delta t^2}[u_j^{p,q,r|n+1} - 2u_j^{p,q,r|n} + u_j^{p,q,r|n-1}] \tag{3-12}$$

Figure 3-2 depicts the Finite Difference stencil for the 8^{th} order accurate approximation of the first spatial derivative. This illustrates the complexity involved in the simulations running on such a high accuracy. Rearranging and implementation of equations 3-11 and 3-12 enables to calculate the wavefield at a forward timestep $u_j^{p,q,r|n+1}$ when having the wavefield from the actual and previous time step, $u_j^{p,q,r|n}$ and $u_j^{p,q,r|n-1}$, respectively. Also the neighboring data points (Figure 3-2) of the actual wavefield, $u_j^{p,q,r|n}$, need to be given (Weiss and Shragge, 2013).

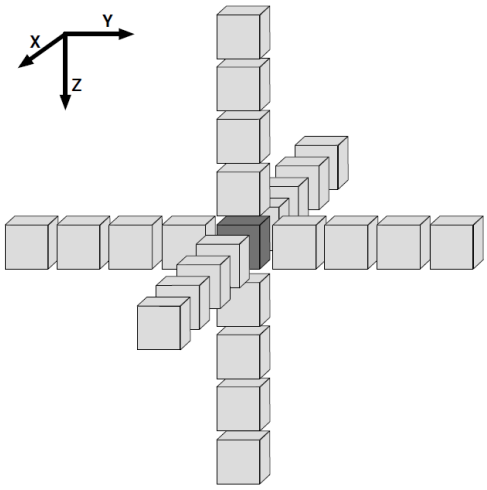

Figure 3-2: Finite Difference stencil. The 8^{th} order accuracy of the spatial derivative approximation requires 25 data points to solve the problem for a certain time step (after Weiss and Shragge (2013)).

Stability

An essential aspect to consider using a FD scheme is the stability problem. The numerical discretisation needs to satisfy certain criteria to stay stable. Having a certain grid spacing and time step, the simulated information can not propagate faster than the "velocity of the mesh". Taking the Nyquist frequency $f_{max} \leq \frac{v_{min}}{2\Delta x}$ into account, the grid spacing should at least satisfy the condition $\Delta x \leq \frac{v_{min}}{2f_{max}}$. Considering 2 samples per wavelength as given in the Nyquist condition, spatial aliasing is theoretically avoided. Still, numerical stability is not secured. In more general, the following equation with variable n grid points per wavelength describes the spatial stability criterion.

$$\Delta x \leq \frac{1}{n} \frac{v_{min}}{f_{max}} \tag{3-13}$$

Following Alford et al. (1974) 5 grid points per wavelength are considered to be sufficient for a fourth order accurate scheme in order to avoid artefacts resulting from numerical methods in seismic modelling. This definition will be applied in the following, even though the accuracy in space is of eighth order.

For stable and dispersion-free solutions the Courant-Friedrich-Lewy (CFL) criterion is introduced by Courant et al. (1928). The Courant number C is a necessary condition and

restriction for numerical stability when chosen smaller or equal to 1 in 1D media.

$$C = \frac{v_{max}\Delta t}{\Delta x} \leq 1 \tag{3-14}$$

The CFL criterion, however, does not ensure stability for different complexities (higher dimensions) of the numerical problem. Hence the largest possible time step is calculated with the CFL criterion $\frac{v_{max}\Delta t}{\Delta x} < \frac{1}{\sqrt{D}}$ which is rearranged to:

$$\Delta t < \frac{1}{\sqrt{D}} \frac{\Delta x}{v_{max}} \tag{3-15}$$

where D is the dimension of the model domain. Satisfying all the introduced criteria, the FD modelling runs without instabilities in the wave field.

Boundary Conditions

Boundary conditions are introduced to decrease the influence of non-physical reflections from the model boundaries. Although artificial boundaries are essential for calculating solutions of partial differential wave equations, they generate unwanted reflections. Boundary conditions reduce these reflections and are furthermore needed to generate a unique and well-posed solution (Engquist and Majda, 1977).

The first condition considered is the free surface. Generally, the air-solid boundary is represented on the top side of the computational domain (Virieux et al., 2012). Implementation of the topography-free surface is fairly straightforward. Directly on the surface, the normal vector points in z-direction (x_3). Using that assumption, the stress can be set to zero: $\sigma_{i3} = 0$, with $i = 1, 2, 3$ in a three-dimensional medium (Weiss and Shragge, 2013).

All other boundaries are defined by an absorbing boundary condition (ABC) which is derived from the one-way wave equation. The basic principle is taking advantage of the wave equation in the opposite direction in the boundary in order to attenuate the signal (Yang, 2014). The second operator is an exponential damping sponge layer on each side (Weiss and Shragge, 2013). The sponge layer is 90 grid points wide. Unfortunately, the size of the computational model increases with increasing width of the sponge layer and hence these boundary condition makes the simulation computationally more expensive. A reasonable balance between computational time, size of sponge layer and reduction of boundary reflections is found with 90 grid points for the sponge layer.

3-2 Seismic modelling around the COSC-1 borehole

3-2-1 Data: Modelled seismic properties

To model the seismic elastic wave propagation around the COSC-1 borehole, data from the drill core is provided. Representing all main lithologies in the area, Table 3-1 gives an overview of the data. 9 samples from various depth levels are taken and seismic properties are modelled. From rock texture and mineral composition, representative densities and seismic velocities are determined. The metamorphic rocks are characterised by preferential alignment of minerals, introducing a directional dependency of seismic velocity. The two different P-wave velocities are perpendicular (min. v_P) and parallel (max. v_P) to the foliation. For the S-wave velocity two different polarizations are calculated. The first polarization (v_{S1}) being faster than the second one (v_{S2}). Again, the maximum value for each polarizations is the velocity propagating in the horizontal plane (parallel to foliation) and the minimum value gives the velocity perpendicular to the foliation. Furthermore the max. v_{S1} is horizontally polarized and the S-wave with the velocity of max. v_{S2} is vertically polarized.

Chapter 3-1 and the results stated in Wenning et al. (2016) already confirmed the validity of a VTI medium. S-wave propagation in z-direction is not polarized and thus the velocities min. v_{S1} and min. v_{S2} should be the same, which is approximately true. Differences between 1 % and 4.5 % are justifiable when accounting for measurement inaccuracies during the small-scale seismic measurements conducted on the core and the fact that modelled properties represent an ideal averaged value. The average of both values describes the vertical S-wave velocity. Max. v_{S1} gives the fastest horizontal velocity.

Having modelled seismic velocities and the respective density, the elasticity constants, and the Thomsen parameters are calculated. Table 3-2 lists all three Thomsen parameters (ϵ, δ and γ) for each sample determined after Equations 3-3 and 3-4. The elastic constants are determined with $V_P^2(90°)$ and $V_P^2(0°)$ corresponding to max. and min. v_P, respectively. The input parameters $V_{SH}^2(0°)$ and $V_{SH}^2(90°)$ in Equation 3-3 refer to the average of min. v_{S1} and v_{S2} and respectively the value of max. v_{S1}. As already stated in the results of the core orientation (Chapter 2-2) the layering is fairly horizontal. Assuming it is valid for the complete depth of the borehole, the minimum modelled seismic velocities are perpendicular to the layering and represent therewith the vertical P- and S-wave velocities that are needed as the main input for the anisotropic seismic modelling. All other input parameters are additionally listed in Table 3-2.

Table 3-1: Modelled seismic properties from rock texture and mineral composition.

Sample	Lithology	Depth top (m)	Density (g/ccm)	Min. v_P (km/s)	Max. v_P (km/s)	Av_P (%)	Min. v_{S1} (km/s)	Max. v_{S1} (km/s)	Av_{S1} (%)	Min. v_{S2} (km/s)	Max. v_{S2} (km/s)	Av_{S2} (%)
COSC_149	amphibolite	552.7	2,936	6,431	6,842	6,193	3,661	3,802	3,779	3,608	3,688	2,193
COSC_193	amphibolite	652.5	2,982	6,333	7,014	10,205	3,601	3,877	7,382	3,564	3,698	3,690
COSC_243	calc-silicate	794.0	2,67	6,204	6,498	4,629	3,688	3,825	3,647	3,638	3,729	2,470
COSC_403	felsic gneiss	1252.2	2,655	5,927	6,359	7,032	3,837	4,006	4,310	3,696	3,924	5,984
COSC_487	calc-silicate	1498.8	2,726	6,358	6,608	3,856	3,653	3,775	3,285	3,606	3,694	2,411
COSC_556	amphibolite	1698.0	3,004	6,282	7,118	12,478	3,578	3,937	9,554	3,536	3,73	5,340
COSC_631	amph-gneiss	2107.9	3,078	6,454	7,343	12,887	3,651	3,934	7,462	3,614	3,764	4,066
COSC_664	qtz-mylonite	2304.7	2,633	5,917	6,297	6,222	3,973	4,106	3,292	3,851	4,079	5,750
COSC_691	mica-schist	2467.5	2,788	5,121	7,029	31,407	3,195	4,35	30,616	3,054	3,612	16,742

Table 3-2: Vertical P- and S-wave velocity, Density and calculated Thomsen parameters for all main lithology types.

Sample	Lithology	Epsilon	Gamma	Delta	Density (10^{12} kg/ckm)	v_P (km/s)	v_S (km/s)
COSC_149	amphibolite	0.066	0.047	0.136	2.936	6.431	3.635
COSC_193	amphibolite	0.113	0.086	0.219	2.982	6.333	3.583
COSC_243	calc-silicate	0.049	0.045	0.102	2.670	6.204	3.663
COSC_403	felsic gneiss	0.076	0.066	0.154	2.655	5.927	3.767
COSC_487	calc-silicate	0.040	0.041	0.085	2.726	6.358	3.630
COSC_556	amphibolite	0.142	0.113	0.264	3.004	6.282	3.557
COSC_631	amph-gneiss	0.147	0.086	0.272	3.078	6.454	3.633
COSC_664	qtz-mylonite	0.066	0.051	0.136	2.633	5.917	3.912
COSC_691	mica-schist	0.442	0.469	0.562	2.788	5.121	3.125

3-2-2 The geological background model and modelling parameters

The model is based on the lithology of the drill core. On-site lithology determination for the different core sections reveals interval thicknesses ranging from several centimetres to one meter. This irregularly distributed classification contains 4311 data points in total. In order to build a realistic, but still simple model a coarser division in 6 m intervals is chosen. For each interval, the representative lithology is chosen from the on-site description. For the uppermost 100 m, no drill core exists so there is no lithology description. Preliminary geological investigations result in a classification of felsic gneiss for that part. Since the core description thereafter starts with 40 m of gneissic rocks it seems reasonable. The outcome of rescaling the on-site lithology description is a 1D lithology log with 415 data points (Table A-1 in the appendix). The modelled seismic properties are assigned to the according lithology and the 1D log is extended to a 3D model block with horizontal layers. The geological and geophysical surveys in the area confirm fairly horizontal layers and the core reorientation confirmed this assumption. In both the acoustic televiewer images and the core scans the lithological boundaries are almost horizontal. Only micro-cracks were identified with varying dipping angles. Since cracks are not considered in this model, horizontal layers are a valid simplification. In total, the model dimensions reach 3000 m in each lateral direction and 2490 m in depth.

The geological model contains horizontal layers of different lithologies. Varying mineral composition and rock texture are the reasons for the anisotropic behaviour of the six rock types. In reality, a range of factors has to be considered, which introduces a high complexity to anisotropic modelling. Not only the intrinsic mineralogy dependent anisotropy needs to be accounted for. Another component is direction-dependency of seismic velocities by fracture systems and micro-cracks. Due to high complexity, they are not considered. All models are illustrated in the following figures. It is necessary to build 3D models of both vertical v_P and v_S, the density and all three Thomsen parameters.

Figure 3-3: P-wave velocity model extracted from the on-site lithology log and extended in a 3D model block with horizontally extending layers.

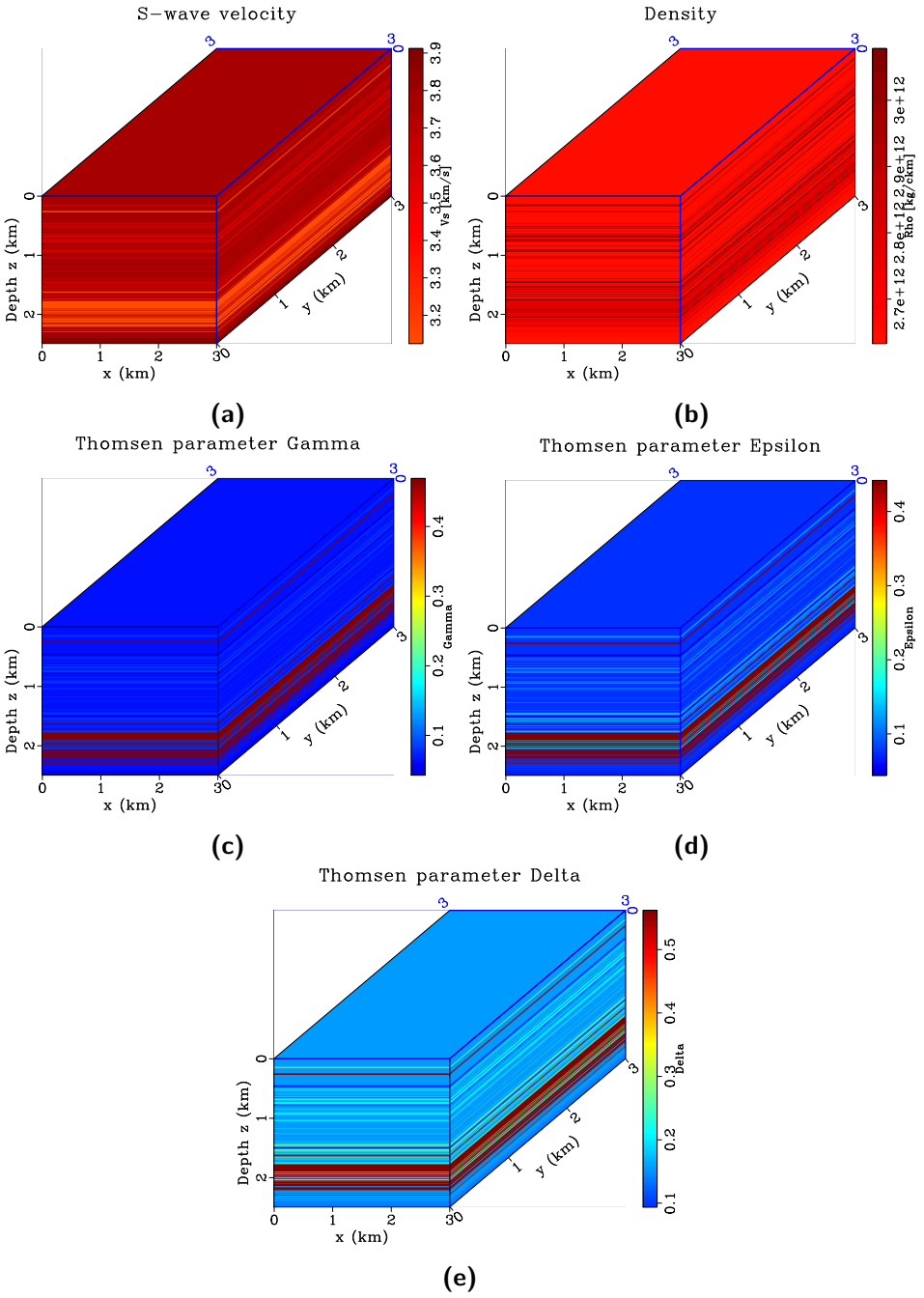

Figure 3-4: a) S-wave velocity model extracted from the on-site lithology log and extended in a 3D model block with horizontally extending layers. b) Density model extracted from the on-site lithology log and extended in a 3D model block with horizontally extending layers. c) Model of the Thomsen parameter γ. d) Model of the Thomsen parameter ϵ. e) Model of the Thomsen parameter δ.

Modelling parameters

In total the numerical discretisation comprises a total of 104,416,416 grid points (416 x 501 x 501) with a grid size of 6 m in each direction. This grid satisfies the spatial stability analysis very well, presuming a maximum frequency of 100 Hz (see Equation 3-13). Applying the CFL stability criteria given in Chapter 3-1-2, a sample rate of 0.45 ms is implied. In order to reach a recording time of at least 1.5 seconds, 3500 time steps are chosen. The recording of the slower S-wave going through the entire medium is secured with the chosen recording time. Table 3-3 lists all model parameters and Table 3-4 summarises source and receiver coordinates.

Table 3-3: Parameters for the FDTD modelling.

Grid points in x-direction (nx)	501
Grid points in y-direction (ny)	501
Grid points in z-direction (nz)	416
Grid size in x-direction (dx)	6 m
Grid size in y-direction (dy)	6 m
Grid size in z-direction (dz)	6 m
Number of time steps (nt)	3500
Time step (dt)	0.45 ms
Frequency	50 Hz

Table 3-4: Source and receiver coordinates.

	Surface-based	Zero-offset VSP
Source (x,y,z)	60 m, 60 m, 30 m	1500 m, 1500 m, 30 m
Receiver spacing	6 m	6 m
Receiver geometry	2D mesh at z = 30 m	1D line at x = y = 1500 m

The high resolution 2D seismic reflection profile (Hedin et al., 2012) is referred to when choosing the parameters for the source implementation. During the survey the seismic signal is generated by a mechanical source (VIBSIST) and therefore the implemented source signal generates a movement in z-direction only. Figure 3-5 depicts the source wavelet. In the horizontal plane there is no amplitude, since this would represent an exploding source and not a signal produced from a vertical vibrating source. The dominant frequency content of the seismic data was determined to be 50 Hz (Hedin et al., 2015) and therefore a 50 Hz Ricker-wavelet (zero-phase) represents the source.

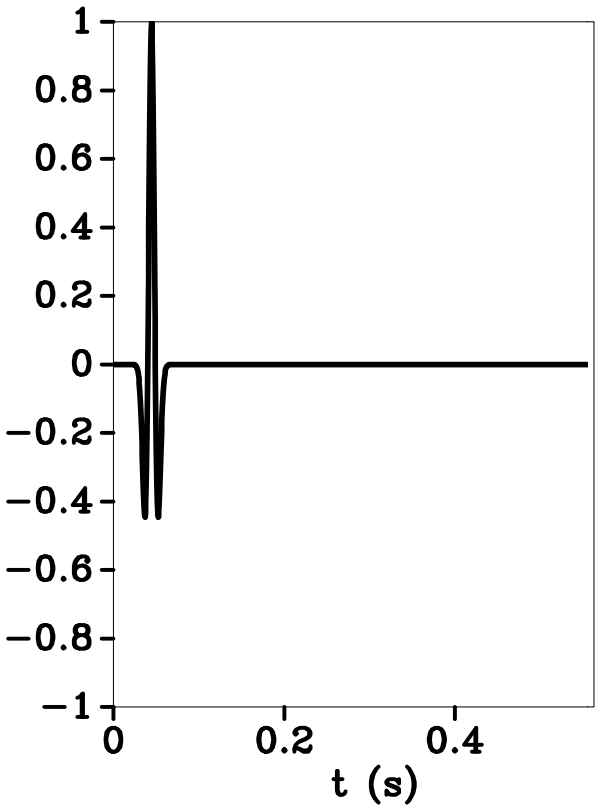

Figure 3-5: 50 Hz Ricker wavelet representing the z-component of the source.

3-3 FD modelling results

This chapter is about the modelling results. In a first step a simple model is generated to test the FD code and the implementation of the SConstruct, which is a script written in *Python* and generating the numerical grid, source and receiver locations and the source signal within *Madagascar*. The FD modelling code (*ewefd3d*) is called in the SConstruct and commands for plotting the results are specified. The SConstruct for the final models is listed in the appendix. The final simulations contain one surface-based seismic survey and one zero-offset VSP and the results are discussed in the following chapters. The geological model (see Chapter 3-2) is the same for both final simulations, since it reflects the simple but realistic geological model of the area around the COSC-1 borehole.

3-3-1 A simple 3D anisotropic model

One of the first tests in 3D is conducted on a model with half the size of the final model (1.5 km x 1.5 km x 1.245 km). The numerical grid has the same increments and time discretisation as the final model. All boundary conditions are established as absorbing boundaries with a sponge layer of 90 cells. The set up is a three-dimensional block containing three layers, the first and third one representing the felsic gneiss embedding a 400 m thick layer of mica-schist. These two lithologies are chosen because they show one of the largest acoustic impedance contrasts. An additional reason is the main presence of felsic gneisses in the upper part of the borehole and an especially high amount of mica-schist in the lower part where the shear zone begins. The vertical P-wave velocity model is shown in Figure 3-6.

Wave propagation through the medium is modelled for 0.675 seconds and the snapshot in Figure 3-7 depicts the displacement wave field after 0.225 s. The image on top illustrates the displacement in z-direction and the waveforms are identified. The first signal propagating is the compressional wave (P), followed by the slower shear wave (S). When the P-wave arrives at the first boundary, the reflected waves are a P-wave (P-P) and the conversion to a SV-wave (P-S). In the x-z plane in the bottom left image, the conversion from the P-wave to a transmitted S-wave is slightly visible. A complementary effect is given for the primary S-wave arriving at the same boundary. The reflected waves are a S-wave (S-S) and a converted P-wave (S-P). The x-z plane in the bottom left image already indicates the conversion from the S-wave to a transmitted P-wave. The P-wave is faster and starts separating from the transmitted S-wave. The recorded shot record is given in Figure 3-8. The first signal is the direct P-wave and the signal with the highest amplitude is the S-wave. Thereafter reflected waves are shown in the x-t and the y-t plane. Highlighted are the recordings of the reflected waves that are explained in the wave field snapshot above.

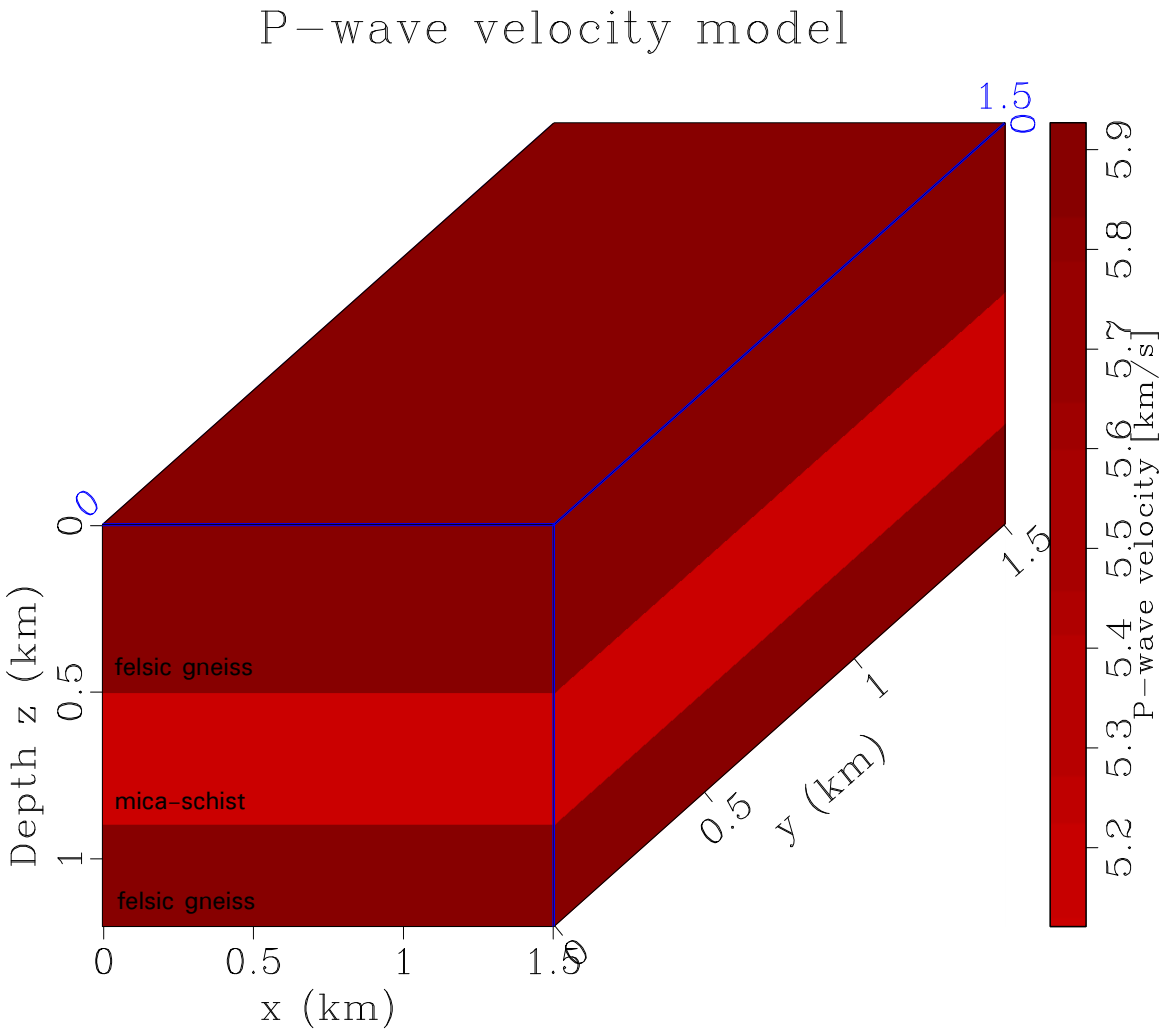

Figure 3-6: Three layer P-wave velocity model with a 400 m mica-schist layer embedded in felsic gneiss.

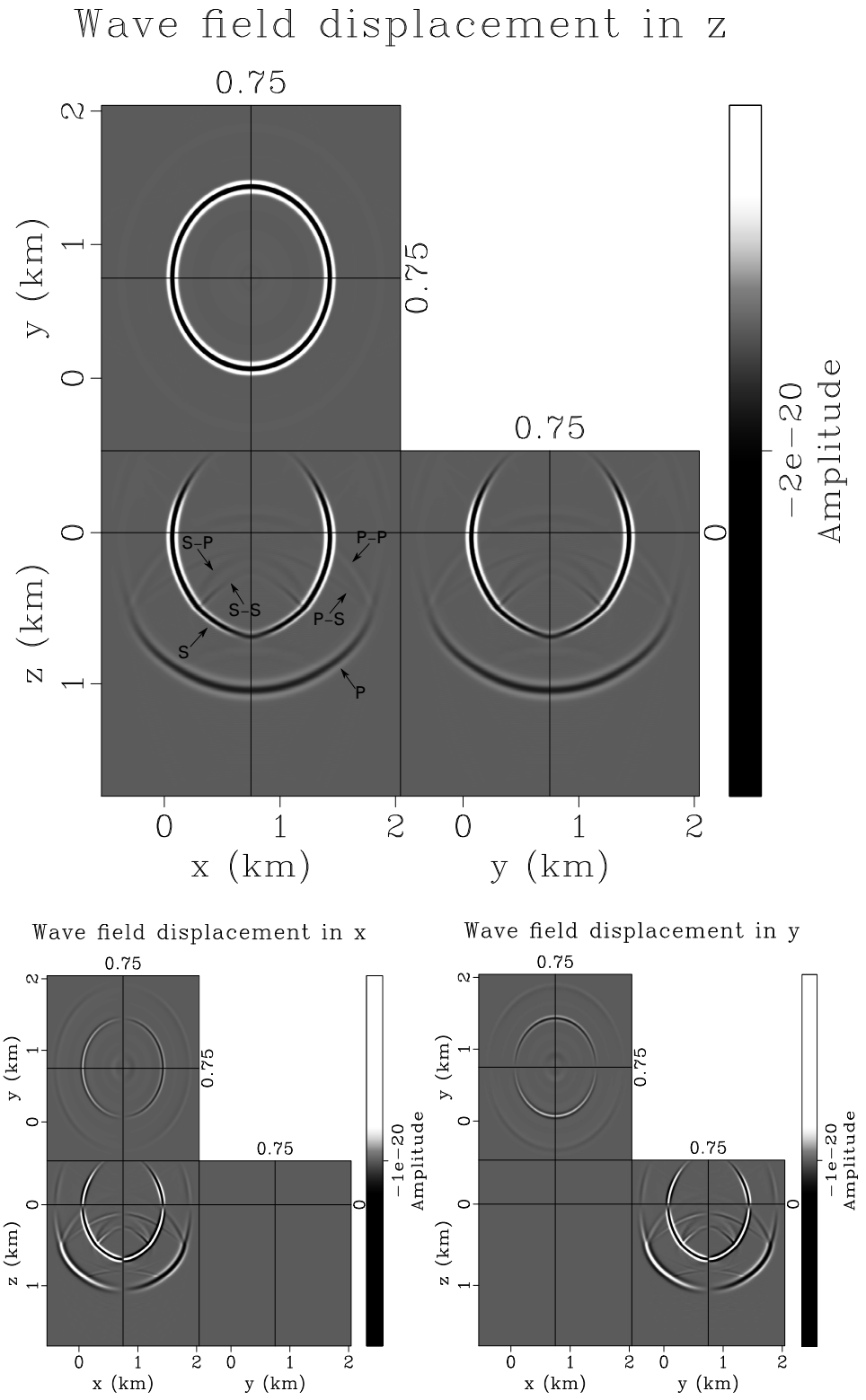

Figure 3-7: Wave field displacement in z-direction (top), x-direction (bottom left) and y-direction (bottom right) at time t =0.225 s. The upper image marks the P- and S-wave generated by the source and travelling through the medium (P and S). Marked are also the reflected waves at the first boundary. The reflected P-wave (P-P) and S-wave (P-S) from the incoming P-wave and the reflected P-wave (S-P) and S-wave (S-S) from the incoming S-wave.

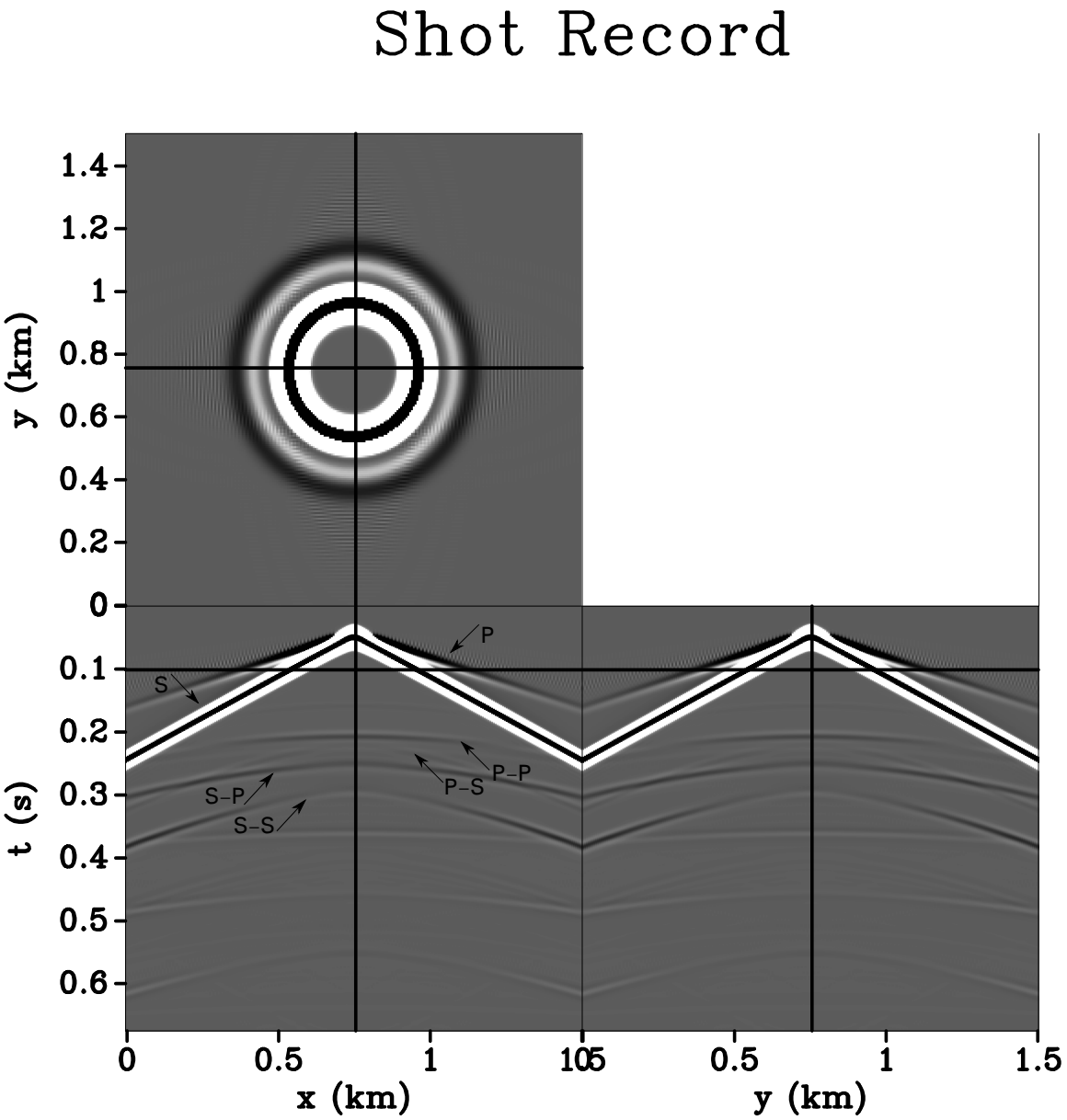

Figure 3-8: The shot record depicts the signal recorded by the receivers at the surface. Marked are the same features as in the wave field displacement snapshot of Figure 3-7.

Numerical dispersions

For a first simulation including the free surface boundary condition, the wave field after several time steps is displayed in Figure 3-9. The boundary condition is set to the free surface on top and the remaining ones are absorbing boundaries with a sponge layer of 90 grid points in each direction. Obviously, the waves propagating close to the surface show distinct influences of numerical dispersion. Since the stability criteria, in general, are satisfied, the solution is stable. In fact, the free surface boundary condition introduces unwanted signals. The same simulation is run again with an absorbing boundary condition on the surface. The dispersions completely disappear. This indicates a numerical problem within the implementation of the free surface. Changing and testing a wide range of different parameters that are still justifiable could not enhance the results significantly. Probably a reduction of frequency and time step simultaneously with increasing the grid size in lateral directions would show improvements. A few different configurations were tested in such a way and minor improvements were observed. On the other hand, changing the source frequency would interfere with the objective of modelling the field data. Additionally, when reducing the size of the time steps the computational time increases drastically. This is not efficient any longer since the regular simulation with the parameters given in Table 3-3 takes more than 7 hours already.

Since the dispersions could not be excluded when changing the numerical discretisation and other modelling parameters, a closer look was taken into the FD code provided by the *Madagascar* software-package. The free surface is implemented in a way that stresses at the surface are all set to zero (for all propagation directions). The stresses txx, tyy, and txy are set to zero, although this is not the correct free surface boundary condition. Due to time limitations and a quite late detection of the erroneous implementation, the boundary condition at the surface is set to an absorbing boundary condition (ABC). This does not reflect the most realistic case, but it is not crucial for achieving satisfying results. Subsequent processes are not dependent on true amplitudes. In fact, the most important factors are recorded travel times and those are not compromised by the absorbing boundary condition.

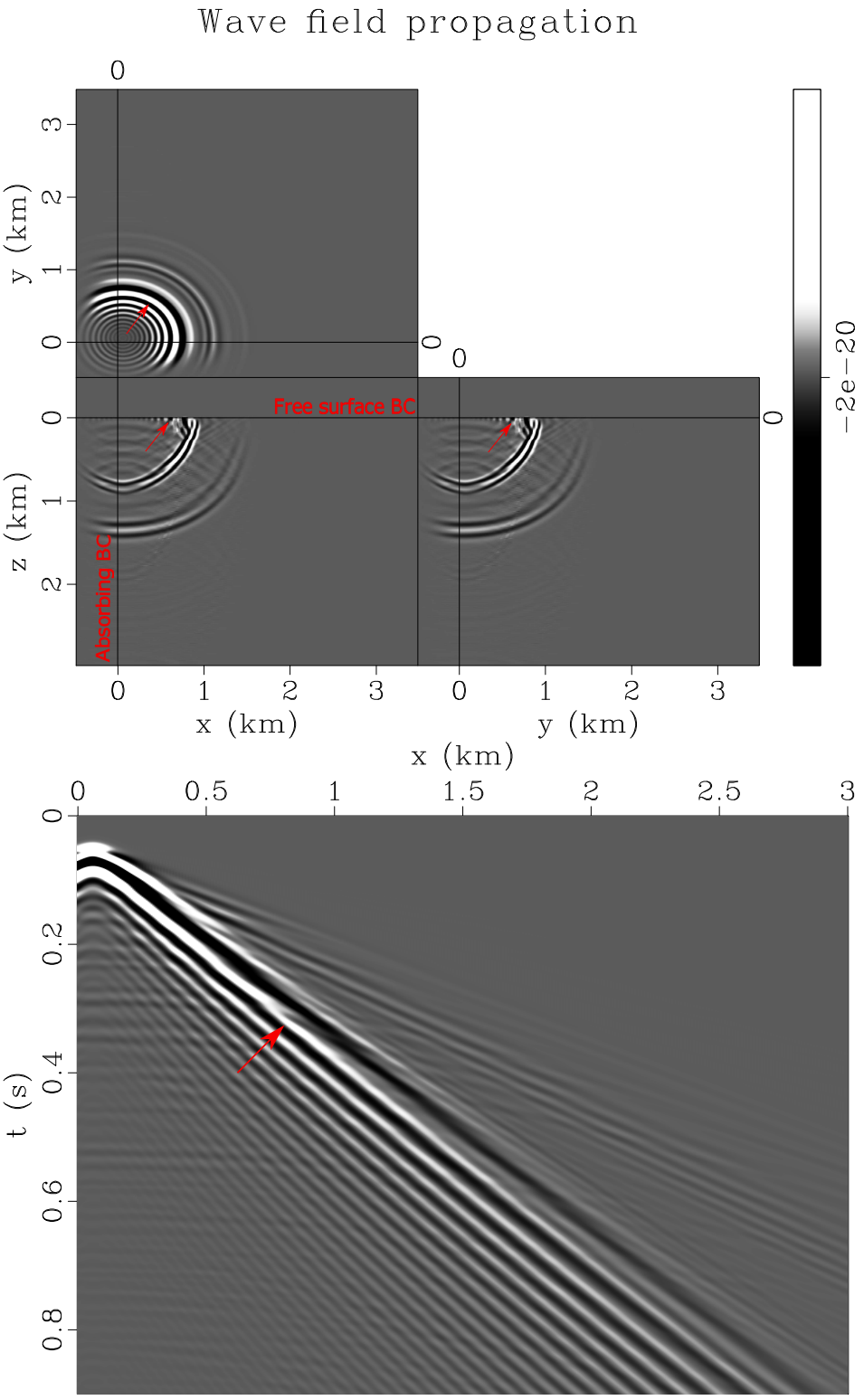

Figure 3-9: Top: Numerical dispersions in the wave field displacement snapshot when applying the free surface condition. Close to the surface major noise is introduced by the Finite Difference solver (red arrow).
Bottom: Recorded signal from the receivers placed 30 m below the surface when applying the free surface condition in the FD code. The noise from numerical dispersion (red arrow) overlays the signal in the shot record.

3-3-2 Result 1: Surface-based seismic simulation

In order to analyse the seismic shot record, an initial look is taken at the elastic wave field propagation. The following Figures 3-10 and 3-11 in this chapter depict the particle displacement in each of the three directions x, y and z. Firstly the z-component of the displacement is shown, followed by the x- and y-component.

Variations from a linear polarization of the wave modes can be introduced by anisotropic velocities and amplitude changes (Yan and Sava, 2009). The wave field is clearly characterised by the intrinsic anisotropy of the geological model. Rather than building up a perfectly circular wave front, the generated elastic waves propagate elliptically. The seismic velocities are faster in the lateral direction than in depth, given by the seismic modelled properties. Mineral composition and rock texture determine the wave to propagate with greater velocity parallel to the foliation, namely in the horizontal direction.

Figures 3-10 and 3-11 illustrate the wave field propagation after 0.1575 s and 0.4725 s, respectively. In all figures, the line at 0 km represents the border to the absorbing boundary layer. Note that the source is not directly set on this boundary, but a few grid points into the model. The pressure wave is the first signal propagating through the medium and is followed by the slower shear wave. Due to changes in acoustic impedance (AI) when arriving at a new lithology, both the P-wave and the S-wave are partly reflected and partly transmitted at those transitions. The reflected wave field is propagating upwards and subsequently recorded by the receivers at the surface. A weak reflection from the boundary at x =0 m is visible in the snapshot. Here the absorbing boundary condition is not powerful enough to provide a total energy decay. The boundary reflection could have been avoided with the implementation of another boundary condition or larger boundary zones, which on the other hand would have been followed by higher computation times. Further work mostly focusses on first arrival times of the direct P- and S-wave. Thus the boundary condition with its reflection does not require more improvements.

The modelled upgoing wave fields are recorded at the surface with a dense grid of receivers. The recorded signal is given in Figure 3-12 as an example for a 2D x-z-slice through the source location. As already observed in the wave field snapshots, the P-wave is characterised by a very weak amplitude. Hence the signal is also weak in the raw shot record. The S-wave first arrival, on the other hand, is characterised by a high energy content and a high amplitude. Both reflections from the P- and the S-wave are displayed by strong hyperbolas at later times.

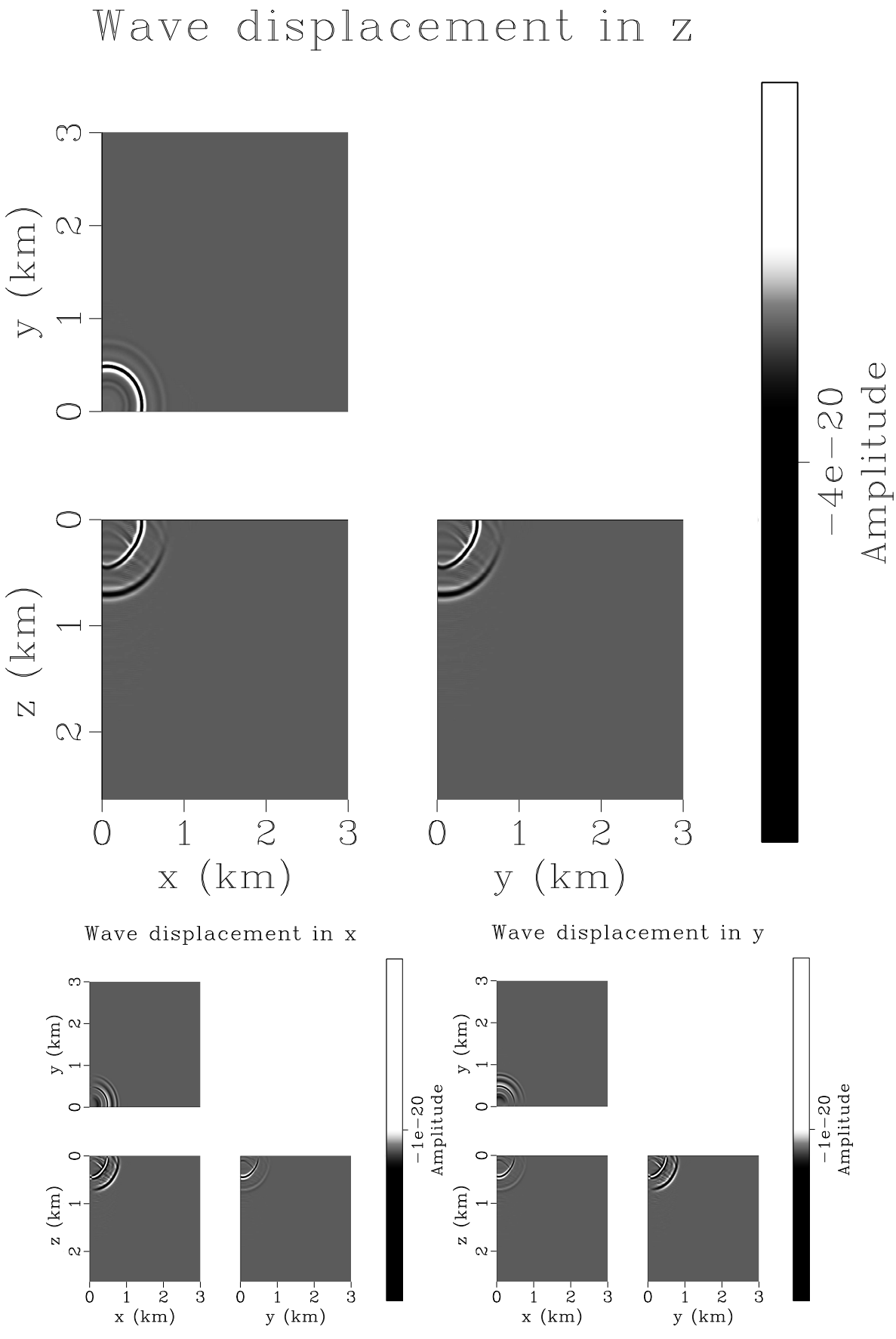

Figure 3-10: Wave field at time t=0.1575 s with a source located 5 grid points below the surface and 10 grid points laterally into the model.

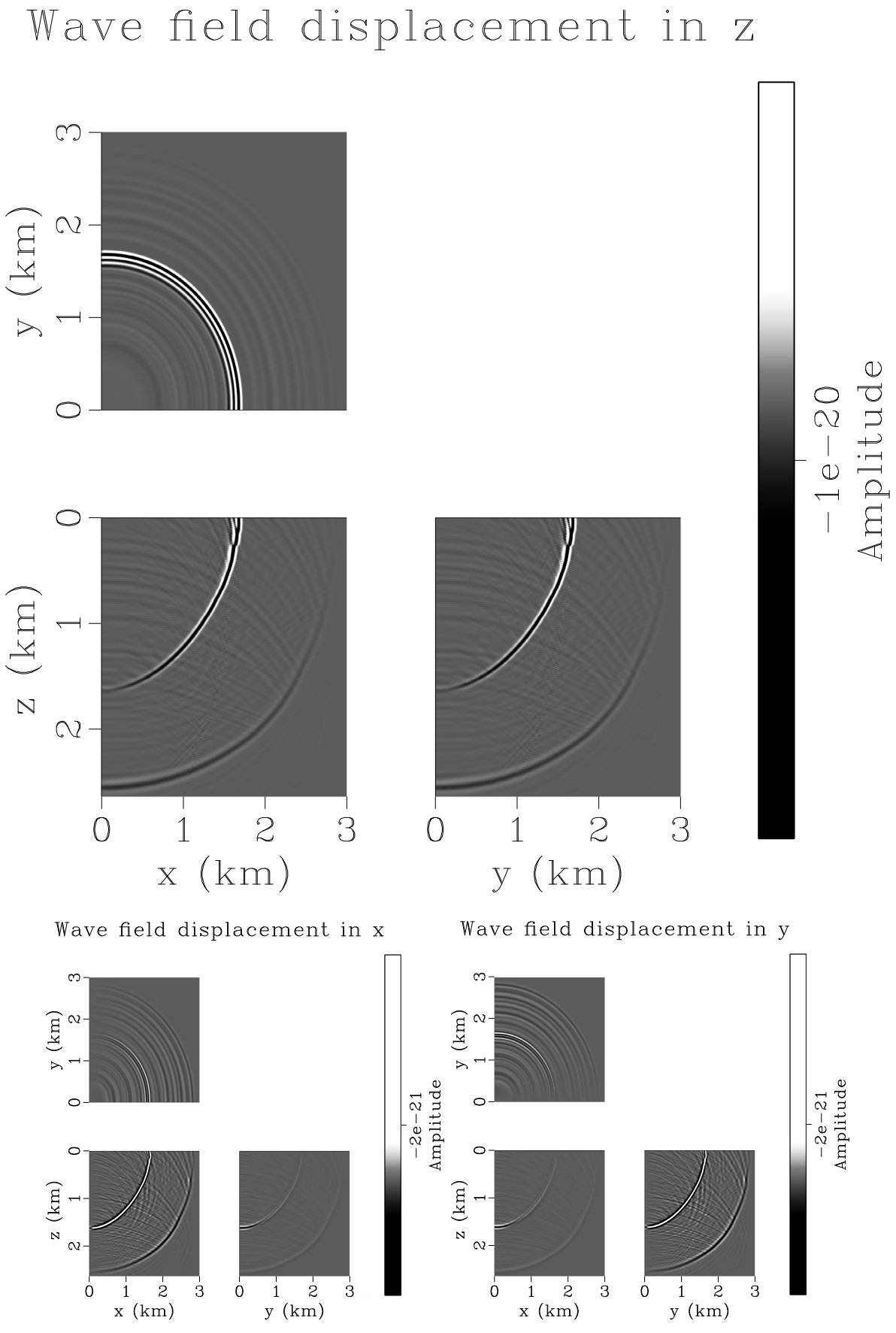

Figure 3-11: Wave field at time t=0.4725 s with a source located 5 grid points below the surface and 10 grid points laterally into the model.

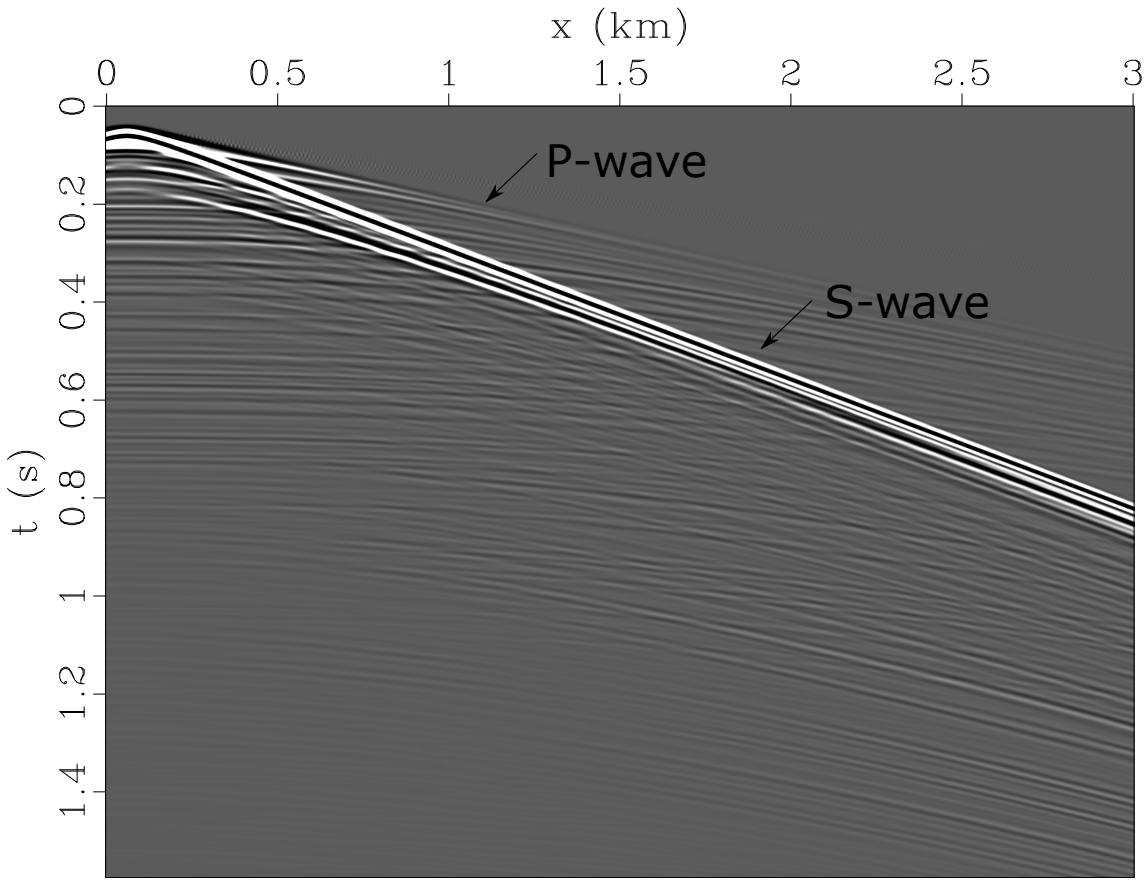

Figure 3-12: Shot record as a 2D slice (x-t-plane) through the source location. The S-wave first arrival is identified by the highest amplitude and the P-wave characterises the overall first arrival, with decreasing amplitude with offset.

3-3-3 Result 2: VSP simulation

For the VSP simulation, the same background model as in Chapter 3-3-2 is chosen and therefore the wave propagation is not shown and described again. The only differences are the source and receiver locations.

The final modelling result is again a 2D shot record. Since the receivers are on a one-dimensional line down from the surface in the center of the model, the record is a function of depth and time. The seismic wave, generated without a lateral offset to the receivers, is travelling down along the receiver line and simulates a zero-offset VSP. The record is shown in Figure 3-13. Both first arrivals are clearly visible for the P- and S-wave, which was expected when observing the wave field propagation. Only at early times the modes are not easily distinguished because the wave modes start separating after around 0.05 s. The z-component at the lowest points of both wave fronts shows high amplitudes. The S-wave is denoted with a strong decrease in amplitude, whereas the p-wave only shows a slight decrease. The noise recorded (red ellipse) before the first P-wave arrival is a numerical issue and will be eliminated with a top mute when further processing the data.

The up-going wave field, generated by reflections at lithological boundaries, is characterised by longer recording times with decreasing depths. Hence these reflections have a different dip than the direct waves in the shot record.

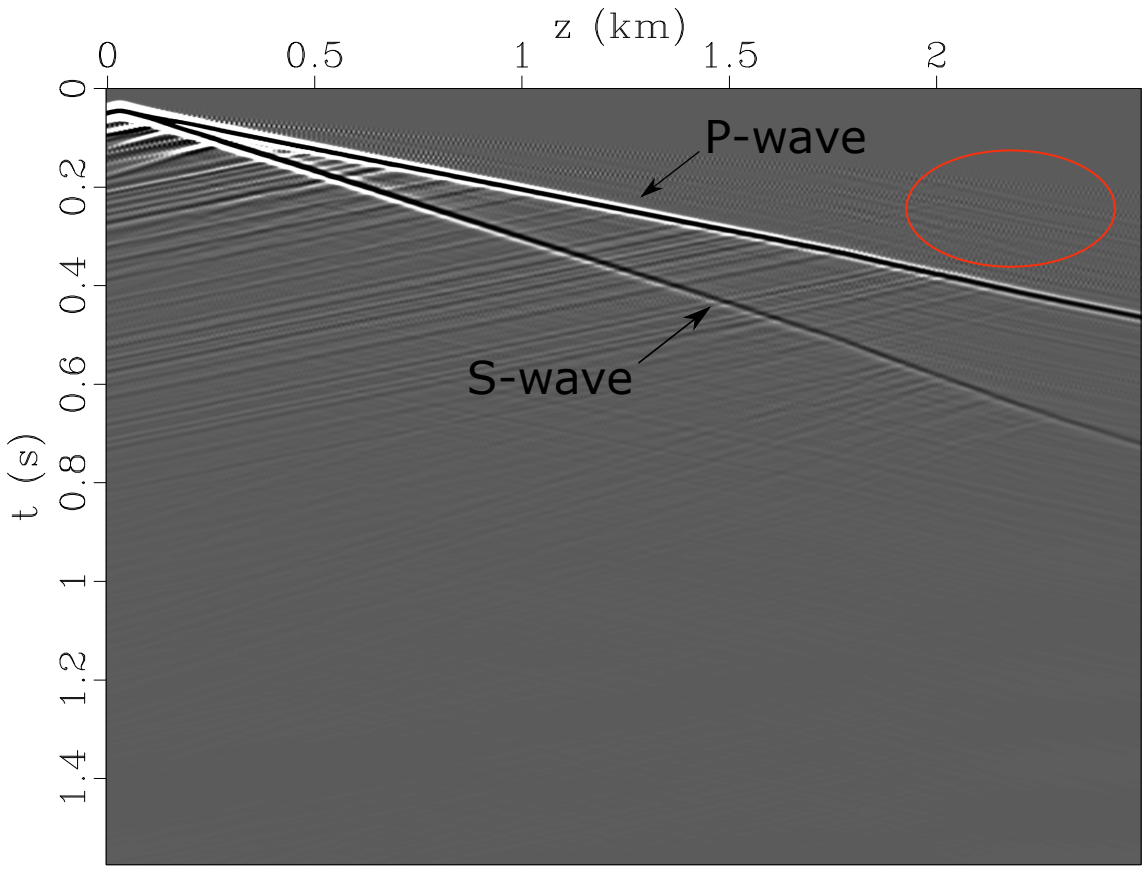

Figure 3-13: Shot record as a 2D slice (z-t plane) through the source location. The P-wave introduces the first signal recorded at each trace an the S-waves first arrival is identified by a pronounced decrease in amplitude with depth. The red ellipse highlights the numerical noise.

3-4 P-wave and S-wave velocity

GLOBE Claritas is a seismic processing software package for 2D and 3D land and marine data. New Zealand's geoscience provider developed the program over 20 years ago. A 2D slice from the shot records generated in *Madagascar* is extracted through the source location and saved in the SEG-Y format. It allowed importing the synthetic data to *GLOBE Claritas* and preparation of the data for further investigations.

3-4-1 First break picking of P- and S-waves

Surface-based seismic simulation

Prior to picking the first arrivals an Automatic Gain Control (AGC) is applied. The normalisation of amplitudes visualises weak first breaks of the pressure wave. Secondary reflections and decreasing amplitude with offset of P- and S-waves are reinforced in amplitude. The most suitable window length is found to be 50 ms. After applying the AGC pronounced noise appears before the first P-wave arrival. This might be noise introduced by the AGC process. More likely it is amplified noise generated by the numerical modelling method, since it is also weakly observed in the wave field snapshot. The polarisation of every second trace is flipped within the noisy section of the recording. When arriving at the first reasonable signal, the polarisation abruptly changes to be reasonable and constant again. Before launching the first break picking algorithm, this noise was removed by applying a top mute to the data. In order to avoid a discontinuous velocity profile with large variations, generated after the first break picking, all traces were resampled to 0.1 ms. The shot record with applied AGC, but still including the noise before the first arrivals, is given in the appendix (Figure B-1).
However, the P-waves first break is characterised by a trough and the S-wave by a peak. The picks are displayed in Figure 3-14. With the automatic picking routine, the peaks and troughs were picked and a few picks had to be corrected manually. Particularly picking of the P-wave close to the source location revealed problems. The arrival is not clearly visible and the different waveforms interfere in a way that allows no identification of first breaks for the P-wave in the first 50 traces. Random picks produced by the automatic picking algorithm were deleted manually in those traces. On the other hand, the S-wave was entirely picked by the automatic picking routine and there is no evidence of erroneous picks in a single trace. After identification of the travel times for the first breaks, the interval velocities can be determined for both wave modes. Calculation of the velocity v at a certain offset (receiver position) is given by the difference in offset divided by the difference in travel time in comparison to the receiver before.

$$v_i = \frac{d_i - d_{i-1}}{t_i - t_{i-1}} \tag{3-16}$$

For the surface-based simulation d is the horizontal distance from the origin of the model and for the VSP in the following part, d is the depth of the receivers with respect to the surface at z=0 m. The spatial sampling rate is high and many data points are acquired. Large variations are visible in the raw data when calculating the velocity for every receiver interval and to achieve a more general velocity trend with offset, the velocity is not calculated for every

receiver interval, but for every eighth receiver, resulting in a spacing of 48 m. Respecting the minimum wavelength of 70 m for the S-wave (with f=50 Hz and v_{min}=3.5 ms), the huge variations of the raw data are a numerical issue and can be eliminated by taking a more averaged curve with larger intervals. The velocity profile is displayed in the next chapter and the velocity profile including the raw data is given in Figure B-3 in the appendix.

VSP simulation

The same procedure as for the surface-based simulation is applied to the synthetic VSP data. The same AGC process with a window length of 50 ms and a top mute are applied. Again the two first arrivals are denoted by a different polarization. The P-wave arrives with a peak and the S-wave with a trough, as illustrated in Figure 3-15. The automatic picking routine had fewer difficulties than before. For every single trace, the arrivals were picked. Just directly close to the source the two wave modes are not easily distinguished and required manual corrections. However, the results are consistent after being improved manually. Velocities are again calculated after Equation 3-16 for intervals of 8 receivers. In the equation, d denotes the respective depth below the surface and the spacing of 8 receivers yields a velocity profile with a velocity measurements every 48 m.

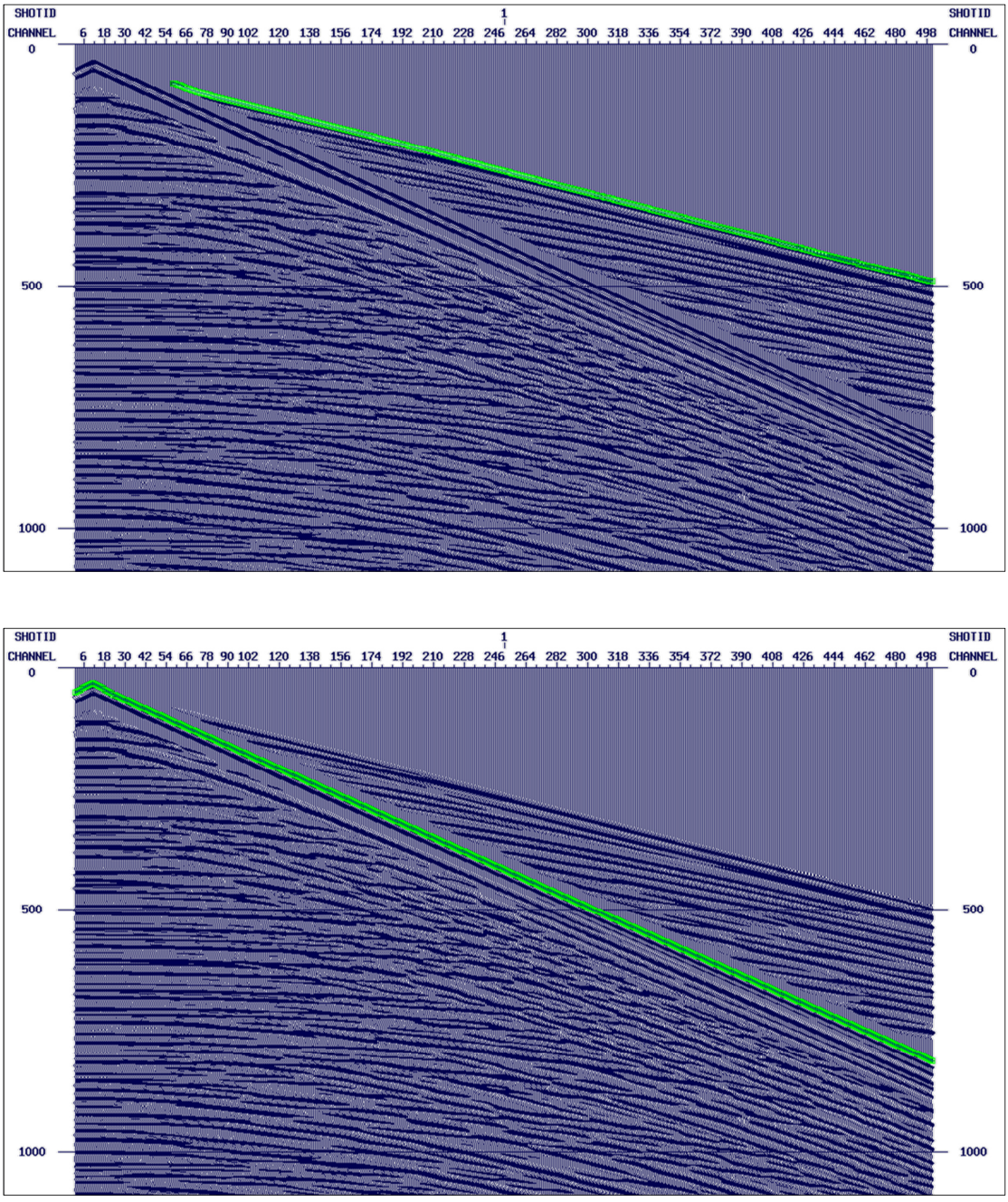

Figure 3-14: First break picks of the P-wave (top) and S-wave (bottom) after application of a top mute and the AGC for the surface-based seismic acquisition.

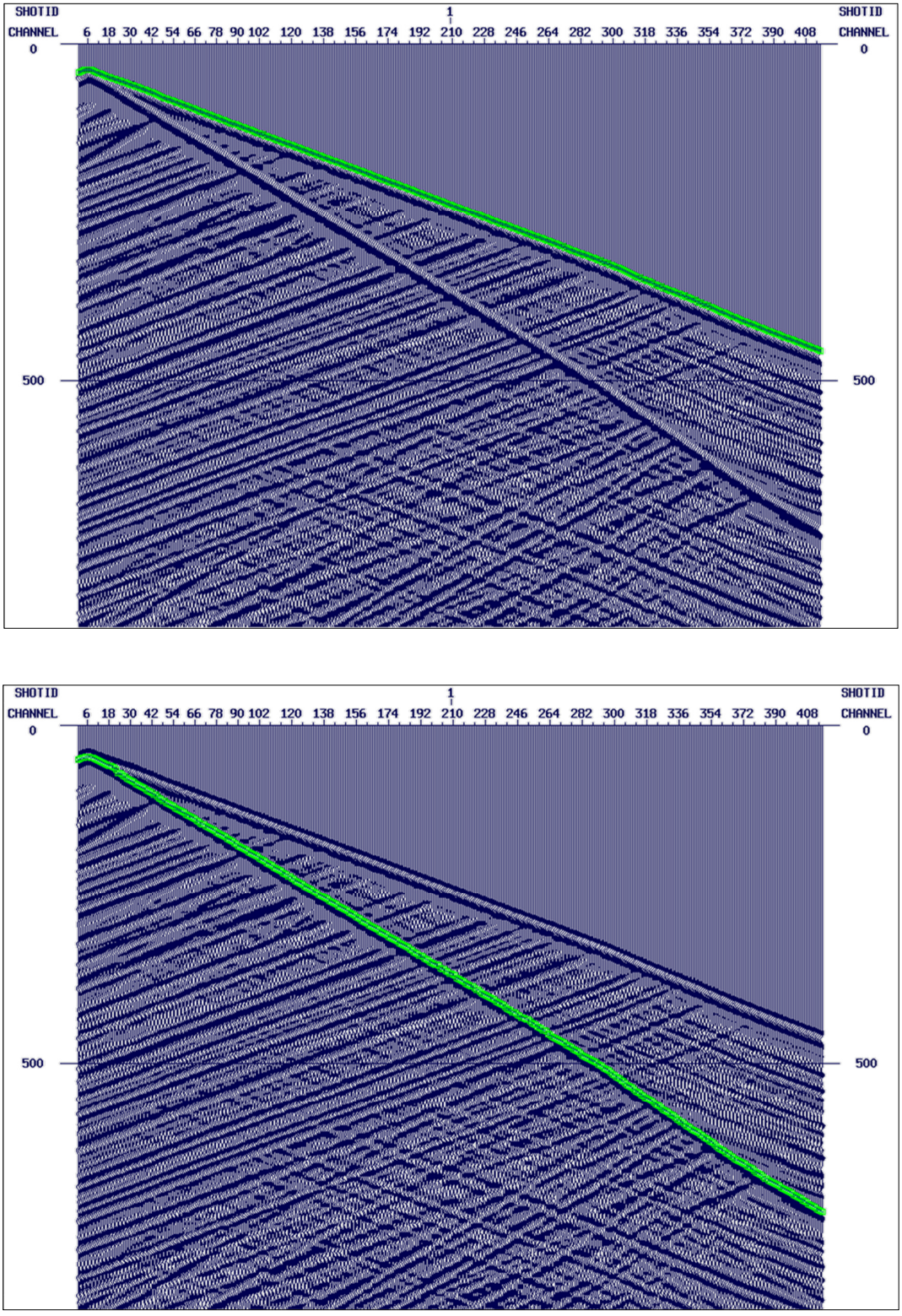

Figure 3-15: First break picks of the P-wave (top) and S-wave (bottom) after application of a top mute and the AGC for the synthetic VSP.

3-4-2 Velocity comparison to field measurements

Small-scale seismic measurements and synthetic VSP velocities

A zero-offset VSP acquisition considers mainly vertically travelling rays. Recorded is the travel time from the source to the respective receiver. Depth intervals of 48 m (8 receivers) are chosen for the velocity determination and the velocity is calculated by dividing the interval length in meters by the interval time in seconds. The results are a P- and S- wave velocity profile over the borehole length of almost 2500 m. The calculated velocity profiles from the synthetic VSP are displayed and described in this chapter.

The shear-wave velocity (black lines in Figure 3-17) ranges roughly from 3100 m/s in the lower part of the borehole to a maximum of almost 5000 m/s at a depth of about 100 m. In the first 1000 m, the velocity is fairly constant with around 3800 m/s, followed by S-wave velocities which strongly vary and a zone of lower velocities starting at 1700 m. From 2000 m to the end of the borehole the S-wave velocity shows and increasing trend from 3100 m/s up to 4000 m/s. The red curve in the same figure displays the small-scale seismic measurements performed on the drill core, representing the FD modelling input. The log is extracted from the 3D model in Figure 3-4a. Both the black and red curve coincide quite good. The broader interval spacing of the modelling output implies differences in the velocity distribution.
However, the vertical P-wave velocity is characterised by much higher variations (black lines in Figure 3-16), ranging from 4800 m/s to 6760 m/s. The general trend begins in the uppermost 700 m with relatively high velocities changing from highest velocities of more than 6700 m/s down to almost 5400 m/s. Then, from 700 m down to 1700 m the velocity is fairly constant between 5500 m/s to 6400 m/s, followed by a zone of low velocities, but great variations. The lowest 400 m level off at around 6000 m/s. The higher range of velocities is already predictable when considering the modelling input. Again the log is extracted from the 3D model (Figure 3-3) and both curves agree with each other. Since the synthetic velocity log is averaged over a larger interval, the values not always reach the small-scale seismic measurements.

VSP field measurements

The P- and S-wave velocity profiles of vertically travelling rays can be compared to a zero-offset VSP field measurement (Krauß et al., 2015) performed at the COSC-1 borehole. The 2 m receiver spacing generated a velocity profile with many data points over the whole borehole length. Hence the profile is smoothed by the Matlab “moving”-function. The P-wave profile required an averaging of 50 receivers to achieve a comparable result to Simon et al. (2016). His tomography results are later on used for the evaluation of the surface-based seismic data. The S-wave profile of the high-resolution VSP only required an averaging over 25 receivers in order to gain a fairly continuous curve without being influenced by strong outliers.

Comparison of field and synthetic VSP velocities

A general trend can be observed when comparing both P-wave velocity profiles (image on the right in Figure 3-16). The tendency to more constant velocities in the central part is clearly visible in both profiles. The velocity in this depth interval beginning at 800 m and ending with the trough at 1600 m the velocity remains approximately 6000 m/s, with a tendency for lower values in the field measurements. From 1700 m the logs are varying again. Still, there is a comparable course. The two minima in the high resolution zero-offset VSP observed at a depth of 1860 m and 2120 m are characterised by a velocity of 5600 m/s. The first depression

is a distinct minimum in the synthetic VSP at a depth of 1840 m and a value of 4800 m/s. The second one is located at 2140 m with a velocity of just below 5000 m/s.

The most obvious difference between the synthetic and acquired data is the upper part until a depth of 700 m. The high resolution VSP is characterised by a continuous increase in velocity with depth with a few variations and the synthetic VSP shows varying but high velocities without the continuously increasing tendency. Summarized are the velocities generally higher for the modelled VSP, particularly in the uppermost 700 m. In the lower part of the borehole, below 1700 m, the field measurements show slightly higher velocities but a comparable trend.

The S-wave velocity profile measured during the high resolution field VSP starts again with an increase in velocity with depth until 600 m (green curve in Figure 3-17). Continuing to the bottom depth of the borehole the S-wave velocity is fairly constant with variations between 3100 m/s and 4000 m/s. Observable are two distinct minima at 1500 m and 1650 m and three minima when arriving at the final depth. Those three minima might be comparable to the three minima in the synthetic VSP (black curve) down at 2160 m, 2300 m, and 2450 m. Although the features are distributed over a wider depth range and giving different velocities, the trend is similar. The remaining velocity profile from the synthetic VSP is not comparable to the real measurements in a straightforward approach. Only the velocity values itself are in the same range, roughly between 3000 m/s and 4000 m/s. The synthetic VSP velocities are slightly higher than measured velocities for both, the P-wave and the S-wave, and an increase in velocity with depth in the uppermost 600 m to 700 m is only observed in the field measurements. The synthetic data are characterised by relatively high values in this upper zone.

Comparison of horizontally travelling waves

Figure 3-18 (left image) depicts two different acquisition approaches for seismic velocities of horizontally travelling waves. The figure on the left represents the velocity profile of the compressional and shear wave based on the first arrival times during the surface-based seismic modelling. First breaks are picked and velocities deduced from travel times and offset over 8 receiver spacings, resulting in an interval velocity every 48 m. This method results in a velocity profile providing the P- and S-wave velocity as a function of offset from the origin of the model. Since the source is next to the origin, the difference can be neglected. A striking difference is noticeable between both curves in the left figure. The direct S-wave is travelling with a constant velocity close to the surface, with a mean of $v_S = 3780$ m/s. In contrast to that, the P-wave shows more variations. The determined velocity from the direct P-wave range from 6000 m/s to more than 7500 m/s. These highly varying values are suitably characterized by a mean of $v_P = 6350$ m/s.
The seismic tomography results (Simon et al., 2016) are displayed in Figure 3-18 on the right. The P-wave velocity profile for each of the three tomography lines is given. For the uppermost 700 m, all three profiles have an increase in velocity from 5100 m/s to 6300 m/s. Between 300 m and 500 m, the curves differ from each other with minor deflections but the overall trend remains fairly similar. When comparing the P-wave velocity with offset to the P-wave velocity in the upper part of the tomography, the average synthetic velocity is considerably higher with $v_P = 6350$ m/s compared to 4800 m/s - 5200 m/s in the uppermost 100 m for the three lines.

Comparison of vertically and horizontally travelling rays

Simon et al. (2016) compared seismic velocities of horizontally and vertically propagating waves by utilising the results of the seismic tomography and the zero-offset VSP from Krauß et al. (2015). The comparison revealed crucial differences in P-wave velocity between the two directions of propagation. Horizontally propagating waves show higher velocities over the whole measured depth, noticing that the horizontal velocities are only provided until a max. depth of 1100 m. Roughly, the difference between both directions is 500 m/s at a maximum.

Following, the synthetic VSP velocity profile (with vertically travelling P-wave), which is already discussed in Figure 3-16, is compared to the tomography results in Figure 3-19. As already mentioned earlier, the modelled velocities from the VSP are higher than the measured ones. Also, the velocity increase in the upper 700 m is not observed in the synthetic data. This is why the VSP velocity, this time, is equal and even higher than the ones from the tomography. Beginning at 800 m depth the measured horizontally travelling are faster than synthetic vertically travelling waves.

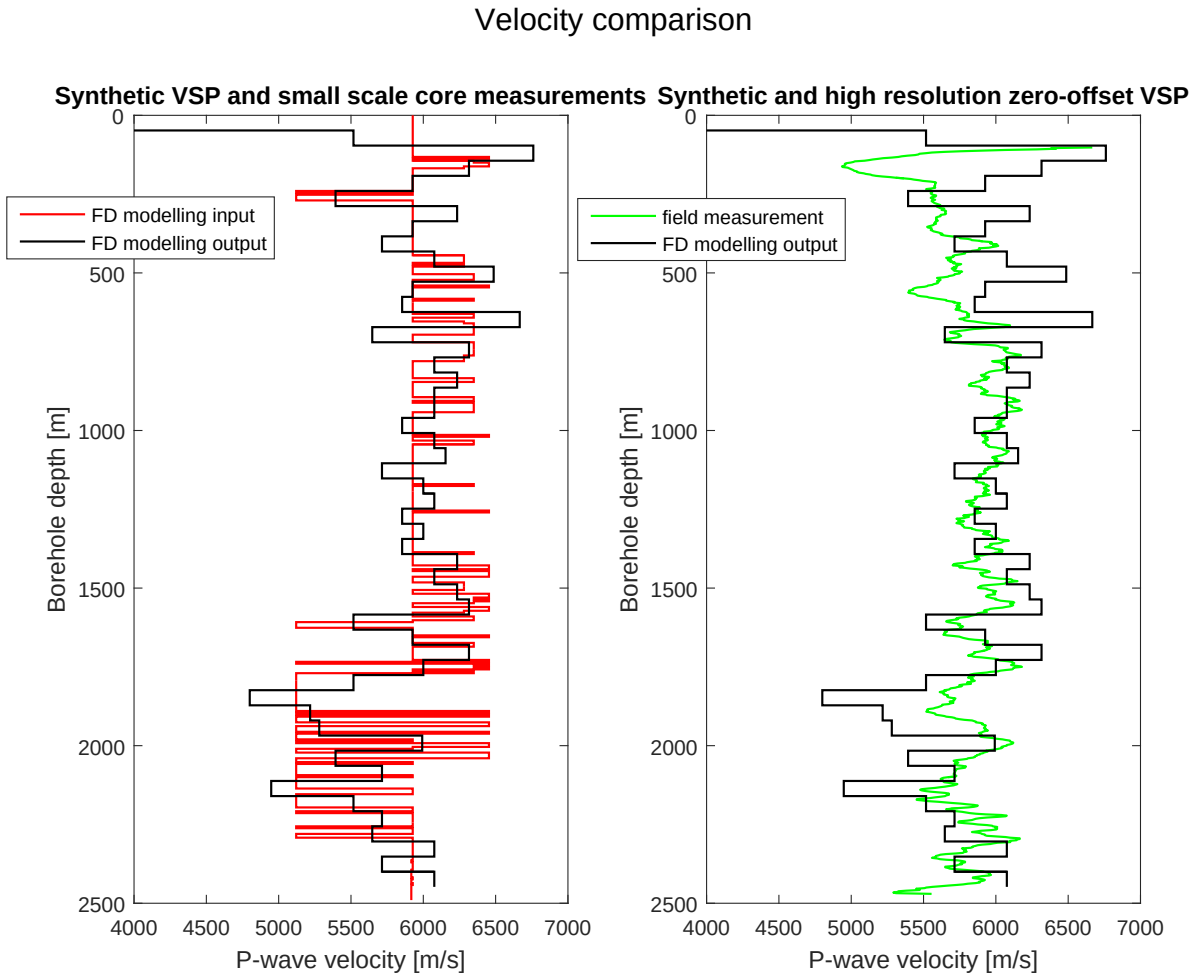

Figure 3-16: Left: P-wave velocity derived from the synthetic zero-offset VSP simulation in black and the modelling input velocity in red. The input velocity (red) represents small-scale seismic measurements on the core.
Right: P-wave velocity for the zero-offset VSP (data from Krauß et al. (2015) measured in the field and a smoothing applied to the data after Simon et al. (2016)) in green. The black line describes again the P-wave velocity derived from the synthetic zero-offset VSP simulation.

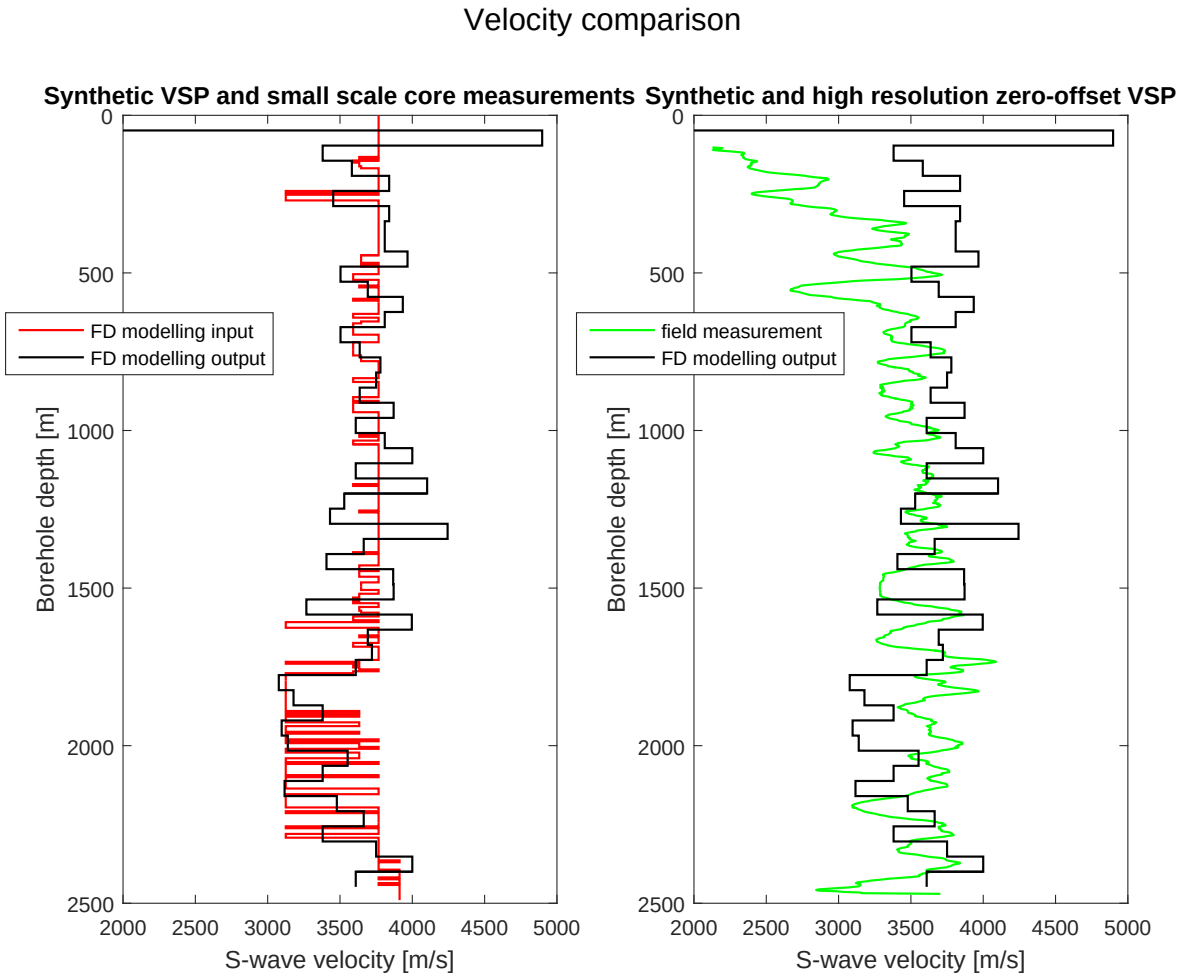

Figure 3-17: Right: S-wave velocity derived from the synthetic zero-offset VSP simulation in black and the modelling input velocity in red. The input velocity (red) represents small scale seismic measurements on the core.
Left: S-wave velocity for the zero-offset VSP (data from Krauß et al. (2015)) measured in the field with a smoothing applied to the data in green. The black line describes again the S-wave velocity derived from the synthetic zero-offset VSP simulation.

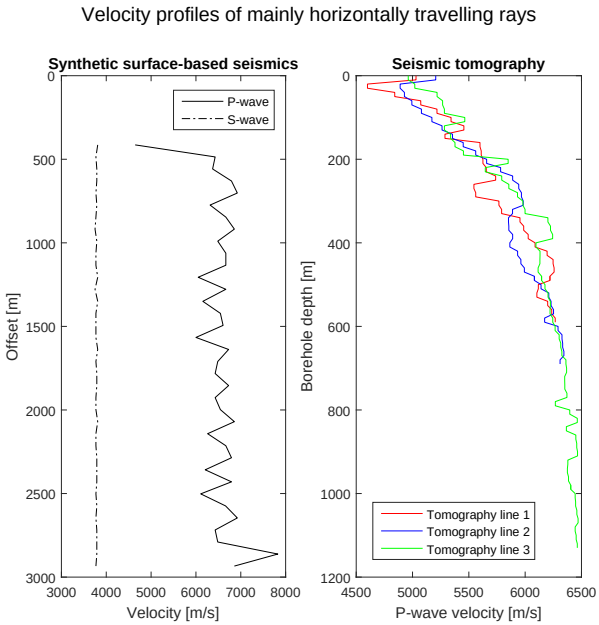

Figure 3-18: Left: Synthetic P- and S-wave velocities determined from first break picks shown in Figure 3-14. The profiles show the wave velocity with respect to offset. Right: P-wave velocity from three tomography lines after Simon et al. (2016). The profiles show the P-wave velocity with respect to the borehole depth.

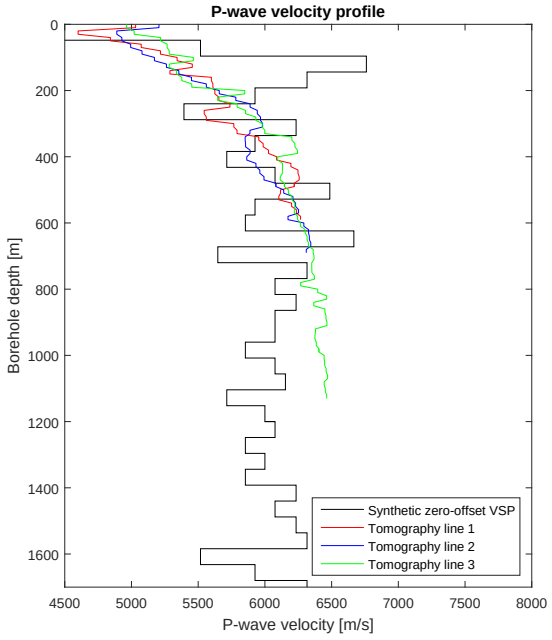

Figure 3-19: Comparison of horizontally (tomography lines) and vertically (synthetic VSP) travelling rays. P-wave velocity determined from simulated zero-offset VSP is represented by the black curve and P-wave velocities from three tomography lines after Simon et al. (2016) are coloured. The profiles show the P-wave velocity with respect to the borehole depth.

Chapter 4

Discussion, Conclusions and Outlook

4-1 Discussion of modelling results in comparison to field measurements

The main difference between the zero-offset VSP measurements and the synthetic velocities is situated in the uppermost 700 m below the surface. Both the P- and S-wave velocities are comparatively high for the synthetic dataset and the measured velocities increase with depth. To explain this increase and also the overall higher values within the synthetic dataset, the impact of fractures, cracks and porosity on seismic velocities needs to be investigated in detail (Bamford and Nunn, 1979).

The influence of fractures on propagation of seismic waves is complex. Parameters like fracture length and orientation, fractional fracture surface in contact and the type of filling material are important factors to be considered when evaluating seismic velocities (Boadu and Long, 1996). In fact, the influence of fractures on velocity is a combined aspect controlled by porosity, pressure, depth, mineralogy and density. Rock porosity has an effect on the seismic wave velocity that exhibits a wealth of studies in the literature, for instance by Barton (2007). Generally, porosity and velocity describe an inversely proportional (often almost linear) relationship. With increasing porosity, the velocity decreases. However, there exist exceptions when the clay content increases in sedimentary rocks or high pressure dominates the regime. The influence of porosity is especially strong when it comes to igneous rocks. Here the porosity is mostly produced by joints and cracks and those decrease the velocity rapidly with assigned porosities of only a few percent (Barton, 2007).
The depth below the surface determines the uni-axial stress, compressive strength, or simply the overburden pressure. The deeper the rock, the higher the pressure caused by the overburden. The pressure has a high impact factor on porosity and density and therefore changes the measured acoustic or elastic wave velocity significantly. When a porous rock is exposed to increasing pressure, the porosity decreases exponentially. This has again an influence on the density since decreasing pore space implies higher densities at the same time. Combining all relations, the seismic velocity increases with depth because pressure and density increase and the porosity decreases drastically, especially in near surface zones.

Micro-cracks, how they appear in the zone of interest, describe the porosity in the COSC-1 area. Since the lithology mainly consists of crystalline (igneous and metamorphic) rocks, nearly no primary porosity exists. The processes described above are pronounced in the measured velocities of the high resolution zero-offset VSP. For both the P- and S-wave velocity profile the first 700 m are described by an increase in velocity. Just below the surface the micro-cracks are still open and provide porosity within the rock. Due to increasing pressure with depth the closure of cracks proceeds and the velocity increases.

Further remarks on anisotropy should be noted for the following discussion. Generally, for sedimentary rocks the anisotropy is either determined by horizontal layers, vertically aligned fractures or a combination of both, describing a vertical or horizontal transverse isotropy (VTI and HTI) or an orthorhombic symmetry, respectively (Tsvankin, 1997). For metamorphic rocks, this can not be generalised so easily. Additional anisotropy is introduced by preferential alignment of minerals and metamorphic foliations within the rock, implying a directional dependence of seismic wave velocity (Schijns et al., 2012). This intrinsic anisotropy is the main contribution within the geological model and other influences are discussed in more detail in this chapter.

The modelled seismic properties introduced in Chapter 3-2 are based on mineralogy and rock texture. They represent the ideal velocity without the influence of porosity or cracks in the system. When building the geological model considering the core lithology and the modelled properties, no fractures were included at all. Also, the modelled properties represent average values for each lithology. One lithology is always substituted by one ideal value for each parameter. This information are accounted for when evaluating the general comparison of measured and synthetic velocity profiles.

The overall velocities are considerably higher for the synthetic data in comparison to the field measurements. Fractures are occurring irregularly over the complete borehole length. Nevertheless, the general trend between measured and synthetic data is comparable which means that the geological model represents the true subsurface, even though it is a simplified representation. Noticeable are the vertically travelling P-waves of the synthetic VSP which result in higher velocities than the measured horizontally propagating waves. This is another indication that the input velocities for the geological model are too high for the numerical modelling approach (see Chapter 3-2). The symmetry of anisotropy, however, should provide higher velocities in the horizontal direction. In the study from Simon et al. (2016), the same comparison is conducted with real measurements and the VTI velocities are approved, giving slower vertical velocities.
In case the influence of cracks would have been considered during the FD modelling, the results would converge more to the field measurements. Presumably, all velocities would be lower by trend and more approaching the measured values. Still, the seismic anisotropy is to evaluate since all previous measurements on core sections confirm anisotropic seismic velocities.

The horizontally travelling direct P-wave from the surface-based seismic simulation reveals higher values than the uppermost velocities from the seismic tomography. Since the direct wave travels close to the surface, impact factors like weathering and non-compacted fractures and pores have to be considered. In the synthetic model, the ideal velocities are implemented and these result in higher velocities.

Comparing the uppermost meters for horizontal and vertical P-waves (synthetic), the horizon-

tally propagating waves are the faster ones. This is also supported by the field measurements introduced above. Generally, the assumption of the seismic anisotropy being described by a VTI symmetry is confirmed by this study. Only the simplification that the anisotropy is only introduced by internal anisotropy produced by the mineralogy can not be affirmed by the numerical modelling results. Especially in the uppermost 700 m, the influence by proceeding closure of fractures on the seismic velocity and anisotropy has to be accounted for. On the other hand, it can not be proven at this point whether fracturing of the rock induces a more complex anisotropic symmetry than the internal VTI symmetry or just a general decrease in velocity. Presumably, this could be investigated when accounting for fractures, cracks and the influence of pressure during forward modelling experiments. Although, it might not be worth the expenditure of time and computational effort building real models since the results with the given model imitates the real situation in a satisfying way.

The fact that the appearance of all VSP velocity curves changes at 1700 m is due to the shear zone that initially occurs at this depth and continues at least until drillers depth. The vertical velocity input for the numerical modelling (red curve in both figures) already indicates the lithology change with a decrease in velocity. All four velocity curves in Figures 3-16 and 3-17 (black curves) imply the change at this depth which again supports the overall impression that the synthetic VSP approach is an adequate simplification of the field measurements.

A possibility to evaluate the anisotropic behaviour is the determination of the measured anisotropy, assuming that the vertical waves during the zero-offset VSP approach propagate within the slowest direction and the horizontal ones from the tomography lines in the fastest. Another assumption for this approach is that the velocities are generally not varying (with azimuth) the horizontal plane within one lithology (VTI). The anisotropy calculation is expressed as

$$Av_p = \frac{v_{P,max} - v_{P,min}}{0.5(v_{P,max} + v_{P,min})} * 100 \tag{4-1}$$

and Figure 4-1 depicts the seismic P-wave anisotropy with respect to the borehole depth. The black curve in the same figure illustrates the P-wave anisotropy generated by the modelled seismic properties which are the input for the Finite Difference modelling. Unfortunately, there is no velocity profile for horizontally travelling waves generated during the synthetic experiments. Therefore it was not possible to create an anisotropy distribution after the seismic simulations. However, the given datasets are not ideal, but still comparable and conclusions can be drawn. In the upper 500 m the anisotropy for the three tomography lines, respecting the VSP velocities, is ranging from nearly zero (isotropic) to partly 15 %. The modelling input anisotropy is generally higher, with values between 5 % and 15 %. Below 500 m the anisotropy curves for the tomography lines and the modelled seismic properties show a good fit.

The comparison of anisotropies supports the hypothesis that the open micro-cracks in the uppermost few hundred meters have an influence on the anisotropic behaviour of seismic wave propagation. Decreased anisotropy in the upper zones during the measurements confirms that the existing cracks lower the anisotropy. In case a medium includes vertical fractures (HTI, horizontal transverse isotropy) the fastest velocity is no longer in the horizontal plane, but in direction parallel to the fractures. Hence the vertical velocity is generally faster than the one in the horizontal direction. In this way the cracks in the vicinity of the COSC-1 borehole introduce a second type of anisotropy, which results in a more complex symmetry, decreasing

the resulting anisotropy. Since the anisotropy below 500 m aligns with the values of the modelled properties it is to assume that the cracks are closing in answer to the overburden pressure and those closed cracks seem to have no impact on anisotropy. However, as stated earlier, they still have an influence on the velocity itself.

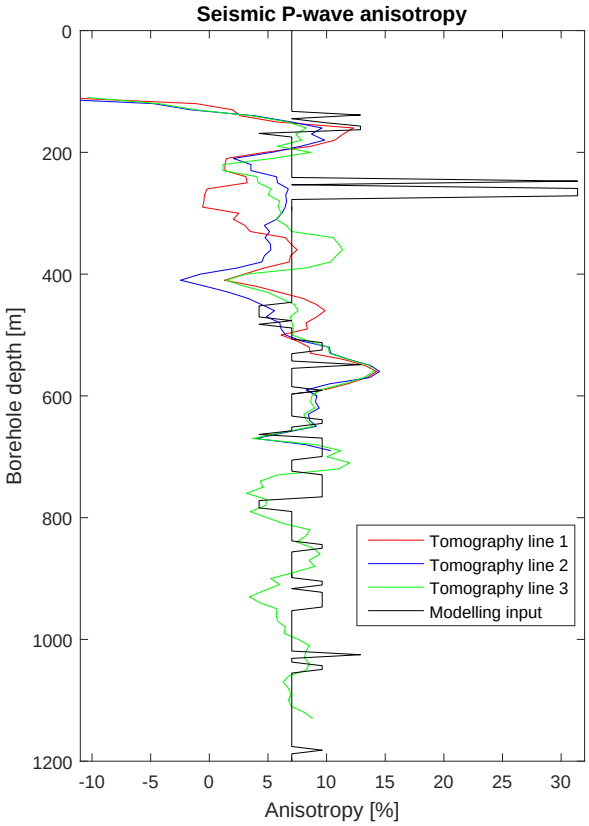

Figure 4-1: The black line displays the maximum P-wave anisotropy calculated from the modelled seismic properties as included in the Finite Difference modelling. The coloured lines represent the anisotropy calculated from the zero-offset VSP (v_{min}) and the tomography lines (v_{max}).

4-2 Conclusions

The core orientation of ten core sections was performed selecting micro-cracks, lithological changes or similar features in the acoustic televiewer image and the core scan. This allowed a manual reorientation of the scans along the automatically oriented televiewer data. Information gained from the core orientation were implemented in the Finite Difference seismic modelling and are described as follows. The layering of different rock types is fairly horizontal. This was already stated in geological reports but the work with televiewer data and core scans confirmed the assumption. Furthermore, the datasets revealed that micro-cracks occur sporadically with varying azimuths. The few core sections from the core orientation did not allow judging frequency of occurrence or characterisation of the cracks.

A simple horizontally layered model based only on the lithological core description was built, including the intrinsic anisotropy introduced by mineralogy. Modelled seismic properties and densities allowed a determination of the Thomsen parameters to account for the internal anisotropic behaviour. Fractures and its associated influence on the wave velocity and additional potential anisotropy were not considered because the complexity of the model would increase drastically and the characteristics of fractures were not given in detail. The elastic seismic modelling through the anisotropic medium resulted in a simulated surface-based seismic dataset and a zero-offset VSP. Subsequent velocity calculations resulted in a velocity profile with depth for vertically propagating waves and a velocity function with respect to offset for horizontally travelling waves, providing direct P- and S-wave velocities.

The comparison to field measurements allows conclusions regarding seismic velocity and anisotropy. Especially comparing synthetic and measured VSP velocities proves that the upper few hundred meters are controlled by fractures which proceed closing with increasing depth. These are not accounted for in the modelled VSP data. The generally higher velocities for the synthetic data are justified by the generated background model. Modelled seismic properties based on mineralogy give an ideal value and no influence of porosity, cracks, changing composition or other parameters are included. Since the general trend between both datasets is similar, the main set up of the geological model is reasonable. Also, the VTI symmetry is a suitable approximation for the anisotropic behaviour, although anisotropy introduced by cracks in the subsurface might have to be considered when performing more realistic modelling around the COSC-1 borehole. The comparison of measured and the input anisotropy exemplifies the influence of micro-cracks on anisotropic wave propagation close to the surface. When cracks are not closed yet due to overburden pressure, the anisotropy is weaker than in deeper zones with closed cracks. Thus, cracks do not only decrease the velocity itself but also decrease the anisotropic behaviour of wave propagation.

Summarized, the almost horizontal layering around the COSC-1 borehole is observed during the core orientation and there is no evidence appearing during the seismic modelling that disfavours this simplification for the purpose of this work. The VTI assumption can be verified when comparing the Finite Difference modelling results to field measurements conducted in the vicinity of the COSC-1 borehole. The influence of the micro-cracks within the crystalline rocks was not considered during the simulations, due to high complexity. However, after comparing simulated velocity profiles to the measured data, the influence of cracks and porosity, in general, is observable. Seismic velocities and anisotropy are reduced by the influence of associated pore space. Especially the uppermost 700 m show a constant increase in velocity

with depth due to closure of the micro-cracks that were observed during the core orientation. This effect is appearing for horizontally and vertically travelling waves in the same way. Still, an anisotropic influence of the cracks can not be evaluated lower than 1100 m.

4-3 Outlook

Further studies are required to evaluate the seismic anisotropy in more detail:

- Numerical modelling of a seismic tomography survey would achieve a velocity profile with depth of horizontally travelling waves. Combined with the modelled VSP velocities the synthetic anisotropy could be compared to the measured anisotropy distribution.
- A seismic tomography line resulting in a velocity profile reaching deeper than 1100 m would give additional knowledge about the seismic anisotropy at greater depth. A dependency on micro-cracks could be drawn in more detail.
- Numerical modelling with fractures or velocity gradients included in the background model would represent a more realistic case and conclusions about velocity and anisotropy could be drawn in addition to the ones in this study.

For more realistic modelling cracks would have to be included in the initial geological model. Due to the very high complexity, it might already be a huge advantage to include a velocity gradient. This gradient adjusts for the pressure gradient that implies a closure of open pore space.

For the further investigations within the COSC-2 project, the planned second borehole in the COSC program (Juhlin et al., 2015), these conclusions should be considered. Not only is the anisotropy introduced by preferential alignments of minerals but also by cracks. Investigations about the influence of cracks on anisotropy below 1100 m were not conducted. This might be a part of subsequent studies. The missing tomography measurements below this depth prohibited further investigations. Additionally, no velocity profile of horizontally travelling waves was modelled during this work. This would also be a chance for the future, in order to gain more knowledge about the anisotropic behaviour of the rocks around the COSC drillholes.

Bibliography

Alford, R. M., Kelly, K. R., and Boore, D. M. (1974). Accuracy of finite-difference modeling of the acoustic wave equation. *Geophysics*, 39(6):834–842.

Bamford, D. and Nunn, K. R. (1979). In situ seismic measurements of crack anisotropy in the carboniferous limestone of northwest England. *Geophysical Prospecting*, 27:322–338.

Barton, N. (2007). *Rock quality, seismic velocity, attenuation and anisotropy.* Taylor & Francis.

Boadu, F. K. and Long, L. T. (1996). Effects of fractures on seismic-wave velocity and attenuation. *Geophysical Journal International*, 127:86–110.

Corfu, F., Andersen, T. B., and Gasser, D. (2014a). The Scandinavian Caledonides: main features, conceptual advances and critical questions. *The Geological Society of London.* From: Corfu, F., Gasser, D., Chew, D. M. (eds) 2014. New Perspectives on the Caledonides of Scandinavia and Related Areas. Geological Society, London, Special Publications, 390, 943.

Corfu, F., Gasser, D., and Chew, D. M. (2014b). New perspectives on the Caledonides of Scandinavia and related areas: introduction. *The Geological Society of London.* From: Corfu, F., Gasser, D., Chew, D. M. (eds) 2014. New Perspectives on the Caledonides of Scandinavia and Related Areas. Geological Society, London, Special Publications, 390, 1-8.

Courant, R., Friedrichs, K., and Lewy, H. (1928). Über die partiellen Differenzengleichungen der mathematischen Physik. *Mathematische Annalen*, 100:32–74.

Danek, T., Lesniak, A., and A., P. (2000). Numerical modeling of seismic wave propagation in selected anisotropic media. *Theses Dissertations Monographies of Mineral and Energy Economy Research Institute Polish Academy of Sciences, Poland*, page 88. ISBN 978-83-60195-48-2.

Engquist, B. and Majda, A. (1977). Absorbing Boundary Conditions for the Numerical Simulation of Waves. *Mathematics of Computation*, 31(139):629–651.

Fichtner, A. (2011). *Full Seismic Waveform Modelling and Inversion*. Springer, Heidelberg.

Gaillot, P., Brewer, T., Pezard, P., and Yeh, E.-C. (2007). Contribution of Borehole Digital Imagery in Core-Log-Seismic Integration. *Scientific Drilling*, 5. 2009 SEG Annual Meeting.

Gee, D. G. (1975). A tectonical model for the central part of the Scandinavian Caledonides. *American Journal of Science*, 275A:468–515. Sveriges geologiska undersökning.

Gee, D. G., Fossen, H., Henriksen, N., and Higgins, A. (2008). From the early Paleozoic platforms of Baltica and Laurentia to the Caledonide Orogen of Scandinavia and Greenland. *Episodes*, 31(1):4451.

Gee, D. G., Juhlin, C., Pacsal, C., and Robinson, P. (2010). Collisional Orogeny in the Scandinavian Caledonides (COSC). *GFF*, 132(1):24–44. doi: 10.1080/11035891003759188.

Gee, D. G. and Sturt, B. A. (1985). The Caledonide Orogen - Scandinavia and Related Areas. *John Wiley and Sons Ltd.*, page 1266 pp. ISBN 0-471-10504-X.

Geologging, R. (2016). High Resolution Acoustic Televiewer. *Acoustic Televiewer Data Sheet*. www.geologging.com.

Hayman, A. J., Parent, P., Cheung, P., and Verges, P. (1998). Improved Borehole Imaging by Ultrasonics. *Society of Petroleum Engineers*, 13(01). SPE Production and Facilities.

Hedin, P., Juhlin, C., and Gee, D. G. (2012). Seismic imaging of the Scandinavian Caledonides to define ICDP drilling sites. *Tectonophysics*, 554-557:30 – 41. doi: 10.1016/j.tecto.2012.05.026.

Hedin, P., Melehmir, A., Gee, D. G., Juhlin, C., and Dyrelius, D. (2014). 3d interpretation by integrating seismic and potential field data in the vicinity of the proposed COSC-1 drill site, central Swedish Caledonides. *Geological Society, London, Special Publications*. In: Corfu, F., Gasser, D., Chew, D.M. (Eds.), New Perspectives on the Caledonides and Related Areas. Geol. Soc. London, Spec. Publ. 390,301319. doi:10.1144/SP390.15.

Hedin, P., Melehmir, A., Gee, D. G., Juhlin, C., and Dyrelius, D. (2015). 3d reflection seismic imaging at the 2.5 km deep COSC-2 scientific borehole, central Scandinavian Caledonides. *Tectonophysics*. doi: 10.1016/j.tecto.2015.12.013.

Juhlin, C. (1995). Finite-Difference elastic wave propagation in 2D heterogeneous transversely isotropic media. *Geophysical Prospecting*, 43:843–858. European Association of Geoscientists & Engineers.

Juhlin, C., Hedin, P., Gee, D. G., Lorenz, H., Kalscheuer, T., and Yan, P. (2015). Seismic imaging in the eastern Scandinavian Caledonides: Siting the 2.5 km deep COSC-2 borehole, central Sweden. *Solid Earth*. doi: 10.5194/se-2015-129.

Klonowska, I., Janák, M., Majka, J., Froitzheim, N., and Gee, D. G. (2015). Discovery of microdiamond in the Åreskutan Nappe of the Seve Nappe Complex, overlying the COSC-1 drillhole. 17.

Krauß, F., Simon, H., Giese, R., Buske, S., Hedin, P., Juhlin, C., and Lorenz, H. (2015). Zero-offset VSP in the COSC-1 borehole. *Geophysical Research Abstracts*, 17(EGU3255). EGU General Assembly 2015.

Lorenz, H., Rosberg, J. E., Juhlin, C., Bjelm, L., Almquist, B., Berthet, T., Conze, R., Gee, D., Klonowska, I., Pascal, C., Pedersen, K., Roberts, N., and Tsang, C. F. (2015a). Operational report about phase 1 of the collisional orogeny in the Scandinavian Caledonides scientific drilling project (COSC-1). *GFZ German Research Centre for Geosciences*. doi: 10.2312/ICDP.2015.002.

Lorenz, H., Rosberg, J. E., Juhlin, C., Bjelm, L., Almqvist, B. S. G., Berthet, T., Conze, R., Gee, D. G., Klonowska, I., Pascal, C., Pedersen, K., Roberts, N. M. W., and Tsang, C.-F. (2015b). COSC-1 drilling of a subduction-related allochthon in the Palaeozoic Caledonide orogen of Scandinavia. *Scientific Drilling*, 19:1–11.

Mavko, G., Mukerji, T., and Dvorkin, J. (2009). *The Rock Physics Handbook - Tools for Seismic Analysis of Porous Media*. Cambridge University Press. ISBN-13 978-0-521-86136-6.

McKerrow, W. S., Mac Niocaill, C., and Dewey, J. F. (2000). The Caledonial Orogeny redefined. *Journal of the Geological Society of London*, 157(6):1149–1154. ISSN: 0016-7649 2041-479X.

Milloy, S. F., McLean, K., and McNamara, D. D. (2015). Comparing Borehole Televiewer Logs with Continuous Core: An Example from New Zealand. *Proceedings World Geothermal Congress 2015*.

Moczo, P., Robertsson, J. O. A., and Eisner, L. (2007). The Finite-Difference Time-Domain Method for Modeling of Seismic Wave Propagation. *Advances in Geophysics*, 48:421–516. doi: 10.1016/S0065-2687(06)48008-0.

Rosberg, J. E. and Lorenz, H. (2012). A new scientific drilling infrastructure in Sweden. *Geophysical Research Abstracts*, 14. doi: EGU2012-7379.

Schijns, H., Schmitt, D. R., Heikkinen, P. J., and Kukkonon, I. T. (2012). Seismic ainsotropy in the crystalline upper crust: observations and modelling from the Outokumpu scientific borehole, Finland. *Geophysical Journal International*. doi: 10.1111/j.1365-246X.2012.05358.x.

Simon, H., Buske, S., Krauß, F., Giese, R., Hedin, P., and Juhlin, C. (2016). The derivation of an anisotropic velocity model from a combinded surface and borehole seismic survey at the COSC-1 borehole, central Sweden. *Geophysical Journal International*. submitted manuscript.

Strömberg, A. G. B., Karis, L., Zachrisson, E., Sjöstrand, T., and Skogland, R. (1994). Bedrock Geological Map of Jämtland County (Caledonides). *Sveriges Geologiska Undersökning, Ca 53*, scale 1:200000.

Thomsen, L. (1986). Weak elastic anisotropy. *Geophysics*, 51. doi: 10.1190/1.1442051.

Tsvankin, I. (1997). Anisotropic parameters and P-wave velocity for orthorhombic media. *Geophysics*, 62(4):1292–1309.

Tsvankin, I., Gaiser, J., Grechka, V., van der Baan, M., and Thomsen, L. (2010). Seismic anisotropy in exploration and reservoir characterization: An overview. *Geophysics*, 75(5):75A15–75A29.

Upadhyay, S. K. (2004). *Seismic Reflection Processing - With Special Reference to Anisotropy*. Springer-Verlag Berlin Heidelberg GmbH, Heidelberg. ISBN 978-3-642-07414-1.

Ureel, S., Momayez, M., and Oberling, Z. (2013). Roch core orientation for mapping discontinuities and slope stability analysis. *IJRET: International Journal of Research in Engineering and Technology*, 2(07). eISSN: 2319-1163 , pISSN: 2321-7308.

Virieux, J., Etienne, V., Cruz-Atienz, V., Brossier, R., and Chaljub, E. (2012). Modelling Seismic Wave Propagation for Geophysical Imaging. *Seismic Waves - Research and Analysis*. ISBN 978-953-307-944-8, doi: 10.5772/30219.

Weiss, R. M. and Shragge, J. (2013). Solving 3D Anisotropic Elastic Wave Equations on Parallel GPU Devices. *Geophysics*, 78. Madagascar reproducibility.

Wenning, Q. C. (2015). Physical rock property and borehole stress measurements from the COSC-1 borehole å re, Sweden. *Master Thesis*. Swiss Federal Institute of Technology Zurich.

Wenning, Q. C., Almquist, B., Hedin, P., and Zappone, A. (2016). Seismic anisotropy in mid to lower orogenic crust: Insights from from laboratory measurements of v_p and v_s in drill core from central Scandinavian Caledonides. *Tectonophysics*. Manuscript.

Yan, J. and Sava, P. (2009). 3d elastic wave mode separation for TTI media. *Society of Exploration Geophysics*, 2009. 2009 SEG Annual Meeting.

Yang, P. (2014). A numerical tour of wave propagation. *Madagascar reproducibility*.

Appendix A

Geological background model

A-1 Raw input data

Table A-1: Lithology summarized in 6 m sections

Top Depth [m]	Bottom Depth [m]	nz	Lithology
0	6	1	gneiss
6	12	2	gneiss
12	18	3	gneiss
18	24	4	gneiss
24	30	5	gneiss
30	36	6	gneiss
36	42	7	gneiss
42	48	8	gneiss
48	54	9	gneiss
54	60	10	gneiss
60	66	11	gneiss
66	72	12	gneiss
72	78	13	gneiss
78	84	14	gneiss
84	90	15	gneiss
90	96	16	gneiss
96	102	17	gneiss
102	108	18	gneiss
108	114	19	gneiss
114	120	20	gneiss
120	126	21	gneiss
126	132	22	gneiss
132	138	23	gneiss

Continued on next page

Table A-1 – *Lithology summarized in 6 m intervals.*

Start Depth [m]	**End Depth [m]**	**nz**	**Lithology**
138	144	24	amphibole gneiss
144	150	25	gneiss
150	156	26	amphibolite
156	162	27	amphibole gneiss
162	168	28	amphibole gneiss
168	174	29	calc-silicate
174	180	30	gneiss
180	186	31	gneiss
186	192	32	gneiss
192	198	33	gneiss
198	204	34	gneiss
204	210	35	gneiss
210	216	36	gneiss
216	222	37	gneiss
222	228	38	gneiss
228	234	39	gneiss
234	240	40	gneiss
240	246	41	gneiss
246	252	42	mica schists
252	258	43	gneiss
258	264	44	mica schists
264	270	45	mica schists
270	276	46	mica schists
276	282	47	gneiss
282	288	48	gneiss
288	294	49	gneiss
294	300	50	gneiss
300	306	51	gneiss
306	312	52	gneiss
312	318	53	gneiss
318	324	54	gneiss
324	330	55	gneiss
330	336	56	gneiss
336	342	57	gneiss
342	348	58	gneiss
348	354	59	gneiss
354	360	60	gneiss
360	366	61	gneiss
366	372	62	gneiss
372	378	63	gneiss
378	384	64	gneiss
384	390	65	gneiss
390	396	66	gneiss
396	402	67	gneiss

Continued on next page

Table A-1 – *Lithology summarized in 6 m intervals.*

Start Depth [m]	End Depth [m]	nz	Lithology
402	408	68	gneiss
408	414	69	gneiss
414	420	70	gneiss
420	426	71	gneiss
426	432	72	gneiss
432	438	73	gneiss
438	444	74	gneiss
444	450	75	gneiss
450	456	76	calc-silicate
456	462	77	calc-silicate
462	468	78	calc-silicate
468	474	79	calc-silicate
474	480	80	gneiss
480	486	81	calc-silicate
486	492	82	gneiss
492	498	83	gneiss
498	504	84	gneiss
504	510	85	gneiss
510	516	86	amphibolite
516	522	87	amphibolite
522	528	88	amphibolite
528	534	89	gneiss
534	540	90	gneiss
540	546	91	gneiss
546	552	92	amphibole gneiss
552	558	93	gneiss
558	564	94	gneiss
564	570	95	gneiss
570	576	96	gneiss
576	582	97	gneiss
582	588	98	gneiss
588	594	99	amphibolite
594	600	100	gneiss
600	606	101	gneiss
606	612	102	gneiss
612	618	103	gneiss
618	624	104	gneiss
624	630	105	gneiss
630	636	106	gneiss
636	642	107	amphibolite
642	648	108	amphibolite
648	654	109	gneiss
654	660	110	gneiss
660	666	111	calc-silicate

Continued on next page

Table A-1 – *Lithology summarized in 6 m intervals.*

Start Depth [m]	**End Depth [m]**	**nz**	**Lithology**
666	672	112	amphibolite
672	678	113	amphibolite
678	684	114	amphibolite
684	690	115	amphibolite
690	696	116	amphibolite
696	702	117	amphibolite
702	708	118	gneiss
708	714	119	gneiss
714	720	120	gneiss
720	726	121	gneiss
726	732	122	amphibolite
732	738	123	amphibolite
738	744	124	amphibolite
744	750	125	amphibolite
750	756	126	amphibolite
756	762	127	amphibolite
762	768	128	amphibolite
768	774	129	calc-silicate
774	780	130	calc-silicate
780	786	131	calc-silicate
786	792	132	gneiss
792	798	133	gneiss
798	804	134	gneiss
804	810	135	gneiss
810	816	136	gneiss
816	822	137	gneiss
822	828	138	gneiss
828	834	139	gneiss
834	840	140	gneiss
840	846	141	amphibolite
846	852	142	amphibolite
852	858	143	gneiss
858	864	144	gneiss
864	870	145	gneiss
870	876	146	gneiss
876	882	147	gneiss
882	888	148	gneiss
888	894	149	gneiss
894	900	150	gneiss
900	906	151	amphibolite
906	912	152	amphibolite
912	918	153	gneiss
918	924	154	amphibolite
924	930	155	amphibolite

Continued on next page

Table A-1 – *Lithology summarized in 6 m intervals.*

Start Depth [m]	End Depth [m]	nz	Lithology
930	936	156	amphibolite
936	942	157	amphibolite
942	948	158	amphibolite
948	954	159	gneiss
954	960	160	gneiss
960	966	161	gneiss
966	972	162	gneiss
972	978	163	gneiss
978	984	164	gneiss
984	990	165	gneiss
990	996	166	gneiss
996	1002	167	gneiss
1002	1008	168	gneiss
1008	1014	169	gneiss
1014	1020	170	gneiss
1020	1026	171	amphibole gneiss
1026	1032	172	gneiss
1032	1038	173	gneiss
1038	1044	174	amphibolite
1044	1050	175	amphibolite
1050	1056	176	gneiss
1056	1062	177	gneiss
1062	1068	178	gneiss
1068	1074	179	gneiss
1074	1080	180	gneiss
1080	1086	181	gneiss
1086	1092	182	gneiss
1092	1098	183	gneiss
1098	1104	184	gneiss
1104	1110	185	gneiss
1110	1116	186	gneiss
1116	1122	187	gneiss
1122	1128	188	gneiss
1128	1134	189	gneiss
1134	1140	190	gneiss
1140	1146	191	gneiss
1146	1152	192	gneiss
1152	1158	193	gneiss
1158	1164	194	gneiss
1164	1170	195	gneiss
1170	1176	196	gneiss
1176	1182	197	amphibolite
1182	1188	198	gneiss
1188	1194	199	gneiss

Continued on next page

Table A-1 – *Lithology summarized in 6 m intervals.*

Start Depth [m]	**End Depth [m]**	**nz**	**Lithology**
1194	1200	200	gneiss
1200	1206	201	gneiss
1206	1212	202	gneiss
1212	1218	203	gneiss
1218	1224	204	gneiss
1224	1230	205	gneiss
1230	1236	206	gneiss
1236	1242	207	gneiss
1242	1248	208	gneiss
1248	1254	209	gneiss
1254	1260	210	gneiss
1260	1266	211	amphibole gneiss
1266	1272	212	gneiss
1272	1278	213	gneiss
1278	1284	214	gneiss
1284	1290	215	gneiss
1290	1296	216	gneiss
1296	1302	217	gneiss
1302	1308	218	gneiss
1308	1314	219	gneiss
1314	1320	220	gneiss
1320	1326	221	gneiss
1326	1332	222	gneiss
1332	1338	223	gneiss
1338	1344	224	gneiss
1344	1350	225	gneiss
1350	1356	226	gneiss
1356	1362	227	gneiss
1362	1368	228	gneiss
1368	1374	229	gneiss
1374	1380	230	gneiss
1380	1386	231	gneiss
1386	1392	232	gneiss
1392	1398	233	amphibolite
1398	1404	234	gneiss
1404	1410	235	gneiss
1410	1416	236	gneiss
1416	1422	237	gneiss
1422	1428	238	gneiss
1428	1434	239	gneiss
1434	1440	240	amphibole gneiss
1440	1446	241	amphibole gneiss
1446	1452	242	gneiss
1452	1458	243	amphibole gneiss

Continued on next page

Table A-1 – *Lithology summarized in 6 m intervals.*

Start Depth [m]	End Depth [m]	nz	Lithology
1458	1464	244	amphibole gneiss
1464	1470	245	amphibole gneiss
1470	1476	246	gneiss
1476	1482	247	gneiss
1482	1488	248	gneiss
1488	1494	249	calc-silicate
1494	1500	250	calc-silicate
1500	1506	251	calc-silicate
1506	1512	252	calc-silicate
1512	1518	253	gneiss
1518	1524	254	gneiss
1524	1530	255	amphibole gneiss
1530	1536	256	amphibole gneiss
1536	1542	257	amphibolite
1542	1548	258	amphibole gneiss
1548	1554	259	amphibolite
1554	1560	260	gneiss
1560	1566	261	gneiss
1566	1572	262	amphibole gneiss
1572	1578	263	amphibole gneiss
1578	1584	264	calc-silicate
1584	1590	265	gneiss
1590	1596	266	gneiss
1596	1602	267	amphibolite
1602	1608	268	amphibolite
1608	1614	269	gneiss
1614	1620	270	mica schists
1620	1626	271	mica schists
1626	1632	272	mica schists
1632	1638	273	gneiss
1638	1644	274	gneiss
1644	1650	275	gneiss
1650	1656	276	gneiss
1656	1662	277	amphibole gneiss
1662	1668	278	gneiss
1668	1674	279	gneiss
1674	1680	280	gneiss
1680	1686	281	amphibolite
1686	1692	282	amphibolite
1692	1698	283	gneiss
1698	1704	284	gneiss
1704	1710	285	gneiss
1710	1716	286	gneiss
1716	1722	287	gneiss

Continued on next page

Table A-1 – *Lithology summarized in 6 m intervals.*

Start Depth [m]	**End Depth [m]**	**nz**	**Lithology**
1722	1728	288	gneiss
1728	1734	289	gneiss
1734	1740	290	amphibole gneiss
1740	1746	291	mica schists
1746	1752	292	amphibole gneiss
1752	1758	293	amphibolite
1758	1764	294	amphibole gneiss
1764	1770	295	gneiss
1770	1776	296	amphibolite
1776	1782	297	mica schists
1782	1788	298	mica schists
1788	1794	299	mica schists
1794	1800	300	mica schists
1800	1806	301	mica schists
1806	1812	302	mica schists
1812	1818	303	mica schists
1818	1824	304	mica schists
1824	1830	305	mica schists
1830	1836	306	mica schists
1836	1842	307	mica schists
1842	1848	308	mica schists
1848	1854	309	mica schists
1854	1860	310	mica schists
1860	1866	311	mica schists
1866	1872	312	mica schists
1872	1878	313	mica schists
1878	1884	314	mica schists
1884	1890	315	mica schists
1890	1896	316	mica schists
1896	1902	317	amphibole gneiss
1902	1908	318	mica schists
1908	1914	319	amphibole gneiss
1914	1920	320	mica schists
1920	1926	321	mica schists
1926	1932	322	mica schists
1932	1938	323	amphibole gneiss
1938	1944	324	amphibole gneiss
1944	1950	325	mica schists
1950	1956	326	mica schists
1956	1962	327	mica schists
1962	1968	328	amphibole gneiss
1968	1974	329	mica schists
1974	1980	330	mica schists
1980	1986	331	mica schists

Continued on next page

Table A-1 – *Lithology summarized in 6 m intervals.*

Start Depth [m]	End Depth [m]	nz	Lithology
1986	1992	332	gneiss
1992	1998	333	mica schists
1998	2004	334	amphibole gneiss
2004	2010	335	amphibole gneiss
2010	2016	336	gneiss
2016	2022	337	mica schists
2022	2028	338	mica schists
2028	2034	339	amphibole gneiss
2034	2040	340	amphibole gneiss
2040	2046	341	amphibole gneiss
2046	2052	342	mica schists
2052	2058	343	mica schists
2058	2064	344	gneiss
2064	2070	345	mica schists
2070	2076	346	mica schists
2076	2082	347	mica schists
2082	2088	348	mica schists
2088	2094	349	mica schists
2094	2100	350	mica schists
2100	2106	351	gneiss
2106	2112	352	mica schists
2112	2118	353	mica schists
2118	2124	354	mica schists
2124	2130	355	mica schists
2130	2136	356	mica schists
2136	2142	357	mica schists
2142	2148	358	gneiss
2148	2154	359	gneiss
2154	2160	360	gneiss
2160	2166	361	mica schists
2166	2172	362	mica schists
2172	2178	363	mica schists
2178	2184	364	mica schists
2184	2190	365	mica schists
2190	2196	366	mica schists
2196	2202	367	mica schists
2202	2208	368	gneiss
2208	2214	369	gneiss
2214	2220	370	mica schists
2220	2226	371	gneiss
2226	2232	372	gneiss
2232	2238	373	gneiss
2238	2244	374	gneiss
2244	2250	375	gneiss

Continued on next page

Table A-1 – *Lithology summarized in 6 m intervals.*

Start Depth [m]	**End Depth [m]**	**nz**	**Lithology**
2250	2256	376	gneiss
2256	2262	377	gneiss
2262	2268	378	mica schists
2268	2274	379	gneiss
2274	2280	380	gneiss
2280	2286	381	gneiss
2286	2292	382	mica schists
2292	2298	383	mica schists
2298	2304	384	gneiss
2304	2310	385	gneiss
2310	2316	386	gneiss
2316	2322	387	gneiss
2322	2328	388	gneiss
2328	2334	389	gneiss
2334	2340	390	gneiss
2340	2346	391	gneiss
2346	2352	392	gneiss
2352	2358	393	gneiss
2358	2364	394	gneiss
2364	2370	395	gneiss
2370	2376	396	mylonite
2376	2382	397	gneiss
2382	2388	398	gneiss
2388	2394	399	gneiss
2394	2400	400	gneiss
2400	2406	401	mylonite
2406	2412	402	mylonite
2412	2418	403	mylonite
2418	2424	404	mylonite
2424	2430	405	gneiss
2430	2436	406	mylonite
2436	2442	407	mylonite
2442	2448	408	gneiss
2448	2454	409	mylonite
2454	2460	410	mylonite
2460	2466	411	mylonite
2466	2472	412	mylonite
2472	2478	413	mylonite
2478	2484	414	mylonite
2484	2490	415	mylonite

A-2 Matlab script for creating geological model in rsf- and rsf@-format

```
clc; clear all; close all;

%%%%%%%%%%% Build model %%%%%%%%%%%%%%%%%%%%%%%%%%%%%%%%%%%%%%%%%%%%%%%%%%%%%
%%%%%%%%%%% Example for building the 3D Vp-velocity model %%%%%%%%%%%%%%%%

% Dimensions
nx = 501;
ny = 501;
nz = 416;

% 1D vector
vp1d=zeros(nz,1);

% Load data from .txt
formatSpec='%f%f%f%C%C';
data=readtable('Lithology1D.txt','Delimiter','\t','Format',formatSpec);

% 4th coloum includes lithology
litho=table2array(data(:,4));

% Set Vp-velocity in km/s for each lithology
for i=1:length(litho);
    if litho(i)=='gneiss';
        vp1d(i)=5.927;
    end
end
for i=1:length(litho);
    if litho(i)=='amphibolite';
        vp1d(i)=6.349;
    end
end
for i=1:length(litho);
    if litho(i)=='amphibole gneiss';
        vp1d(i)=6.454;
    end
end
for i=1:length(litho);
    if litho(i)=='Calc-silicate';
        vp1d(i)=6.281;
    end
end
for i=1:length(litho);
    if litho(i)=='mica schists';
        vp1d(i)=5.121;
    end
end
for i=1:length(litho);
    if litho(i)=='mylonite';
        vp1d(i)=5.917;
    end
end

% extend 1D vector in 3D matrix (horizontal layers)
vp3d=repmat(vp1d,1,nx,ny);

%%%%%%%%%%% Convert to rsf and rsf@ %%%%%%%%%%%%%%%%%%%%%%%%%%%%%%%%%%%%%%%%

% Parameters
n1 = nz;
n2 = nx;
n3 = ny;
n4 = 1;
d1 = 0.006;
d2 = 0.006;
d3 = 0.006;
o1 = 0;
o2 = 0;
o3 = 0;
unit1 = 'km';
unit2 = 'km';
unit3 = 'km';
label1 = 'z';
label2 = 'x';
label3 = 'y';

vp_name = 'vp-3d'; % name of velocity model file
datapath = ...
'C:\Users\Luisa\Desktop\MATLAB\FINAL\';
% path for the rsf@ files
% % when saved in the madagascar working directory later, change the path
% % in the rsf-file to the location of the rsf@ file

% Write model in madagascar rsf format(header file)
fidh = fopen([vp_name '.rsf'],'w');
```

```
fprintf(fidh,'%s\n',['n1=' num2str(n1)]);
fprintf(fidh,'%s\n',['n2=' num2str(n2)]);
fprintf(fidh,'%s\n',['n3=' num2str(n3)]);
fprintf(fidh,'%s\n',['n4=' num2str(n4)]);
fprintf(fidh,'%s\n',['d1=' num2str(d1)]);
fprintf(fidh,'%s\n',['d2=' num2str(d2)]);
fprintf(fidh,'%s\n',['d3=' num2str(d3)]);
fprintf(fidh,'%s\n',['o1=' num2str(o1)]);
fprintf(fidh,'%s\n',['o2=' num2str(o2)]);
fprintf(fidh,'%s\n',['o3=' num2str(o3)]);
fprintf(fidh,'%s\n',['unit1="' unit1 '"']);
fprintf(fidh,'%s\n',['unit2="' unit2 '"']);
fprintf(fidh,'%s\n',['unit3="' unit3 '"']);
fprintf(fidh,'%s\n',['label1="' label1 '"']);
fprintf(fidh,'%s\n',['label2="' label2 '"']);
fprintf(fidh,'%s\n',['label3="' label3 '"']);
fprintf(fidh,'%s\n','data_format="native_float"');
fprintf(fidh,'%s\n','esize=4');
fprintf(fidh,'%s\n',['in="' datapath vp_name '.rsf@"']);
fclose(fidh);

% Data for the rsf@ file
fidd = fopen([datapath vp_name '.rsf@'],'w');
for i=1:n3
    for j=1:n2
        for k=1:n1
            fwrite(fidd,vp3d(k,j,i),'single');
        end
    end
end
fclose(fidd);
```

Appendix B

FD modelling

B-1 SConstruct for modelling in Madagascar

```
from rsf.proj import *
import fdmod,stiffness

# This is the SConstruct for modelling using the ewefd3d code by Madagascar.
# Partly adapted from "2D and 3D Seismic Modeling with Madagascar" by Kyle Shalek and Jeff Daniels (
    The Ohio State University).

# . . Modelling parameters
par = {
    # Space parameters
    'nx':501, 'ox':0, 'dx':0.006,  'lx':'x', 'ux':'km',
    'ny':501, 'oy':0, 'dy':0.006,  'ly':'y', 'uy':'km',
    'nz':416, 'oz':0, 'dz':0.006,  'lz':'z', 'uz':'km',

    # Time Parameters
    'nt':3500, 'ot':0, 'dt':0.00045, 'lt':'t', 'ut':'s',
    'kt':100,'frq':50,

    # Modelling parameters
    'snap':'y','jsnap':350,'nb':90, 'verb':'y',
    'nbell':5, 'jdata':50,'ssou':'y',

    # Output
    'height':5,
    }

# . . Initialize parameters in fdmod module
fdmod.param(par)
par['nframe']=5
par['iframe']=4
par['dabc']='y'

# . . 3D model - load in and plot velocities, density and Thomsen parameters

#################### load-vp ###################################################################
Plot('vp-3d','vp-3d','''
    byte allpos=y bar=y color=j|
    grey3 flat=n color=j frame1=0 frame2=501 frame3=501 wanttitle=y title='P-wave velocity' scalebar
        =y barlabel='Vp [km/s]' barlabelsz=6
    label1="Depth z" label2="x" label3="y"
    ''')
Flow('vp-3d.par','vp-3d','attr want=all')

#################### load-vs ###################################################################
Plot('vs-3d','vs-3d','''
    byte allpos=y bar=y color=j|
    grey3 flat=n color=j frame1=0 frame2=501 frame3=501 wanttitle=y title='S-wave velocity' scalebar
        =y barlabel='Vs [km/s]' barlabelsz=6
    label1="Depth z" label2="x" label3="y"
    ''')
Flow('vs-3d.par','vs-3d','attr want=all')
```

```
##################### load-ro ######################################################################
Plot('ro-3d','ro-3d','''
     byte allpos=y bar=y color=j|
     grey3 flat=n color=j frame1=0 frame2=501 frame3=501 wanttitle=y title='Density' scalebar=y
          barlabel='Rho [kg/ckm]' barlabelsz=6
     label1="Depth z" label2="x" label3="y"
     ''')
Flow('ro-3d.par','ro-3d','attr want=all')

##################### load-eps #####################################################################
Plot('eps1-3d','eps1-3d','''
     byte allpos=y bar=y color=j|
     grey3 flat=n color=j frame1=0 frame2=501 frame3=501 wanttitle=y title='Thomsen parameter Epsilon
          ' scalebar=y barlabel='Epsilon' barlabelsz=6
     label1="Depth z" label2="x" label3="y"
     ''')
Flow('eps1-3d.par','eps1-3d','attr want=all')

##################### load-del #####################################################################
Plot('del1-3d','del1-3d','''
     byte allpos=y bar=y color=j|
     grey3 flat=n color=j frame1=0 frame2=501 frame3=501 wanttitle=y title='Thomsen parameter Delta'
          scalebar=y barlabel='Delta' barlabelsz=6
     label1="Depth z" label2="x" label3="y"
     ''')
Flow('del1-3d.par','del1-3d','attr want=all')

##################### load-gam #####################################################################
Plot('gam1-3d','gam1-3d',''' 
     byte allpos=y bar=y color=j|
     grey3 flat=n color=j frame1=0 frame2=501 frame3=501 wanttitle=y title='Thomsen parameter Gamma'
          scalebar=y barlabel='Gamma' barlabelsz=6
     label1="Depth z" label2="x" label3="y"
     ''')
Flow('gam1-3d.par','gam1-3d','attr want=all')

####################################################################################################

# . . Source Section
# . . Wavelet
fdmod.wavelet('wav_',par['frq'],par)

# . . 3D Elastic source
Flow('souz','wav_','math output=input*1')
Flow('soux','wav_','math output=input*0')
Flow('souy','wav_','math output=input*0')

Flow('wave-3d',['souz','soux','souy'],
     '''
      cat axis=2 space=n ${SOURCES[1:3]} |
      transp plane=12 |
      transp plane=23 |
      transp plane=12
     ''')
# . . plot source wavelet
fdmod.ewavelet3d('wave-3d','',par)

####################################################################################################

# . . Coordinate Section
# . . Surface-based seismic approach
# . . Locate source position
xsou=par['ox']+par['dx']*10
ysou=par['oy']+par['dy']*10
zsou=par['oz']+par['dz']*5
#xsou=par['ox']
#ysou=par['oy']
#zsou=par['oz']

# . . 3D Sources
fdmod.point3d('ss-3d',xsou,ysou,zsou,par)

# . . 3D receivers for the surface based seismic acquisition
fdmod.horizontal3d('tt-3d',par['oz']+par['dz']*5,par)

# fdmod.horizontal3d('tt-3d',0.03,par)
Flow('rr-3d','tt-3d','put n2=%(nx)d n3=%(ny)d |'%par
     +'put n2=%d n3=1' %(par['nx']*par['ny']))

####################################################################################################
# . . 3D receivers for the VSP
# fdmod.vertical3d('rr-3d',par['ox']+(par['nx']-1)*par['dx']/2.,par['oy']+(par['ny']-1)*par['dy
     ']/2.,par)

# . . Source position for the VSP simulation
# xsou=par['ox']+(par['nx']-1)*par['dx']/2
# ysou=par['oy']+(par['ny']-1)*par['dy']/2
# zsou=par['oz']+par['dz']*5
####################################################################################################
```

```
# . . Create a 3D point location for plotting
par['zlook'] = 0
par['nzcut'] = par['nz']/2

center=fdmod.center3d(xsou,ysou,par['zlook'],par)

##############################################################################################

# . . Make 3D stiffness matricies
stiffness.vti3d('Ic-3d','vp-3d','vs-3d','ro-3d','eps1-3d','del1-3d','gam1-3d',par)
stiffness.cplot3d('Ic-3d',1,1,1,par)
Flow('Ic-3d.par','Ic-3d','attr want=all')

##############################################################################################
# . . Elastic Modeling Section
fdmod.ewefd3d('Id-3d','Iw-3d','wave-3d','Ic-3d','ro-3d','ss-3d','rr-3d','ssou=n free=n opot=n',par)

##############################################################################################

# . . Plotting section
# . . Plotting the shot record in 3D
Result('Id-3d',
       '''
           window n2=1 |
           put
           n1=%(nx)d o1=%(ox)g d1=%(dx)g label1=%(lx)s unit1=%(ux)s
           n2=%(ny)d o2=%(oy)g d2=%(dy)g label2=%(ly)s unit2=%(uy)s
           n3=%(nt)d o3=%(ot)g d3=%(dt)g label3=%(lt)s unit3=%(ut)s |
           transp plane=23 memsize=1|
           transp plane=12 memsize=1|
       ''' % par
       + fdmod.dgrey3d('pclip=98 flat=y title="Model Response 3D" '+center+' frame1=%d' % (par['nt'
           ]) ,par))

# . . Prepare data for 2D plot
Flow('Id2-3d','Id-3d',
       '''
          window n2=1 |
           put
           n1=%(nx)d o1=%(ox)g d1=%(dx)g label1=%(lx)s unit1=%(ux)s
           n2=%(ny)d o2=%(oy)g d2=%(dy)g label2=%(ly)s unit2=%(uy)s
           n3=%(nt)d o3=%(ot)g d3=%(dt)g label3=%(lt)s unit3=%(ut)s |
           transp plane=23 memsize=1|
           transp plane=12 memsize=1
       ''' %par)

# . . Plot 2D shot record
Plot('Idplot-2d','Id2-3d', '''window min3=0.06 n3=1 | grey pclip=98''')

# . . Output shot record in 2D. Input for conversion in SEGY/SGY
Flow('Id-2d','Id2-3d', '''window  n3=1 min3=0.06| transp plane=13 | transp plane=12 ''')

##############################################################################################

# . . VSP section
# . . Prepare data for 2D plot
#Flow('Id-2d','Id-3d',
#       '''
#           window n2=1 |
#           put
#           n1=249 o1=0 d1=0.01
#           n2=%(ny)d o2=%(oy)g d2=0.01 label2=%(ly)s unit2=%(uy)s
#          n3=%(nt)d o3=%(ot)g d3=%(dt)g label3=%(lt)s unit3=%(ut)s
#       ''' %par)

# . . Plot 2D shot record
#Plot('Idplot-2d','Id2-3d', '''window min3=1.5 n3=1 | grey pclip=98''')

# . . Output shot record in 2D. Input for conversion in SEGY/SGY
#Flow('Id-2d','Id2-3d', '''window  n2=1 min2=1.5''')

##############################################################################################

# . . Wave field movie for the surface-based seismic method
Plot('Iw-3d',
    '''
    byte gainpanel=all bar=y |
    grey4 scalebar=y barlabel='amplitude' bg=l o1=0 o2=0 o3=0 label1=z unit1=km label2=x unit2=km
        label3=y unit3=km
    flat=y screenratio=1 frame1=95 frame2=100 frame3=100
    title="Wave Propagation"
    ''',view=1)

End()
```

B-2 Raw shot data in GLOBE Claritas

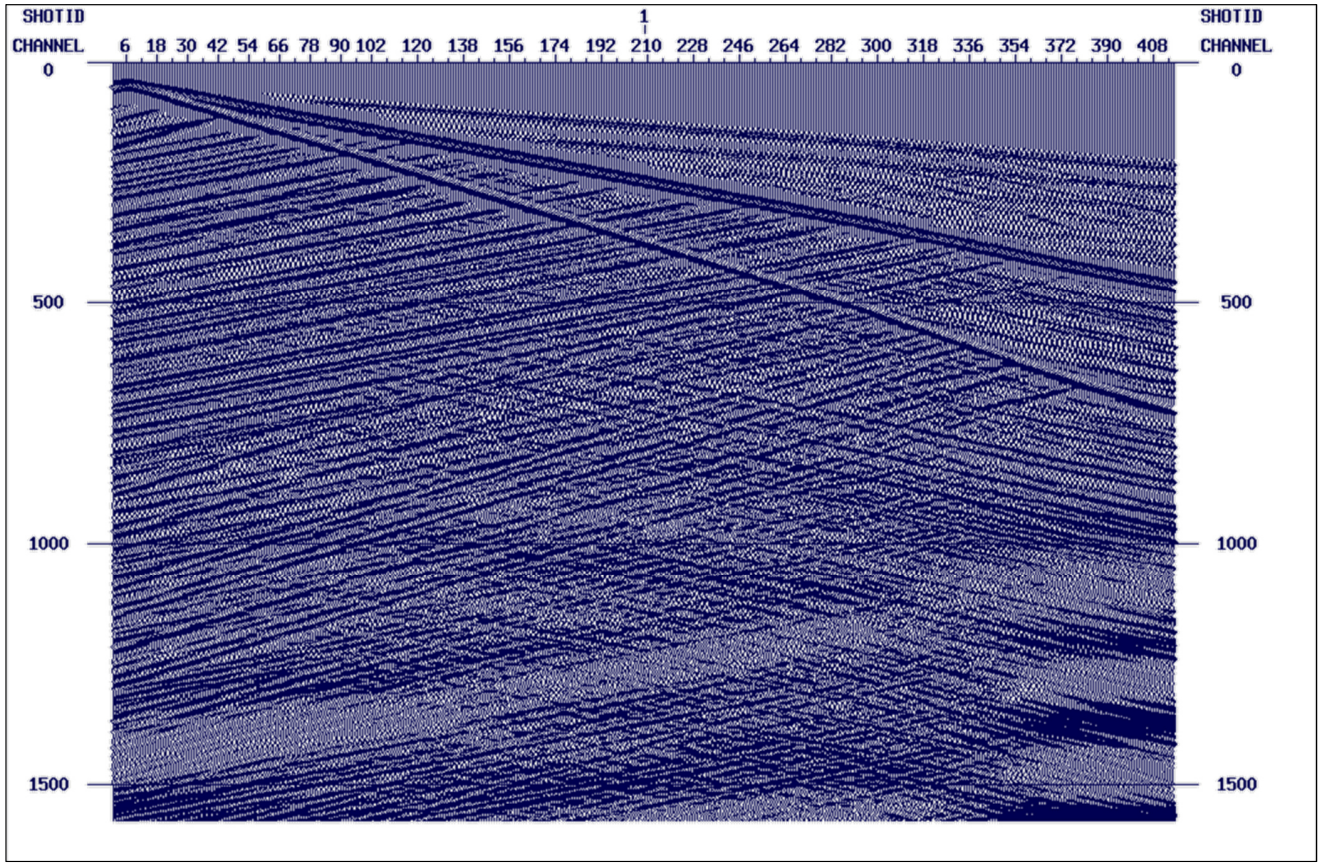

Figure B-1: Surface-based seismic shot record with applied AGC.

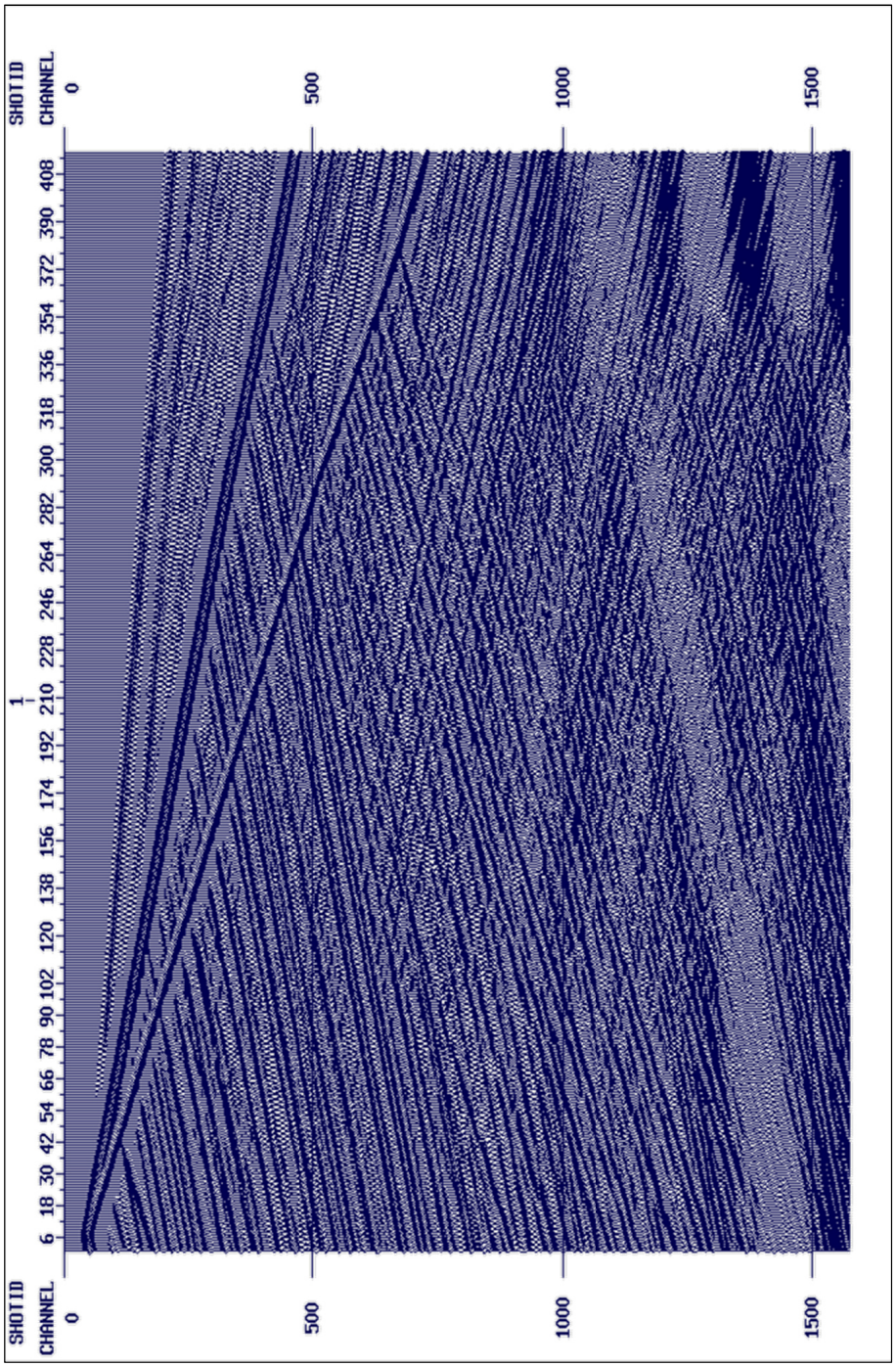

Figure B-2: VSP shot record with applied AGC.

B-3 Raw velocity data and smoothed velocity profiles

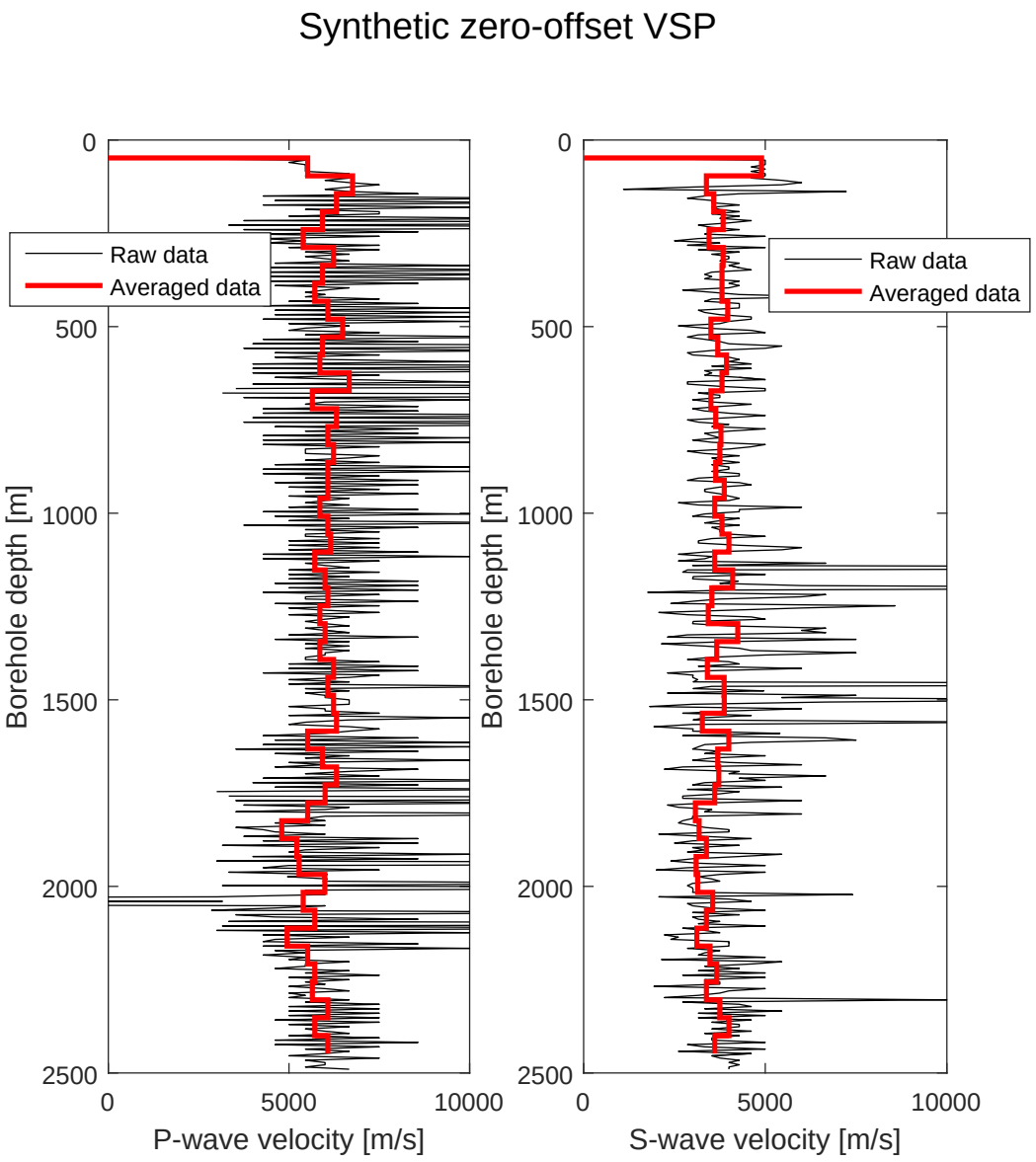

Figure B-3: Synthetic VSP velocity profiles. Raw data in black and velocity profile for 48 m depth intervals in red.

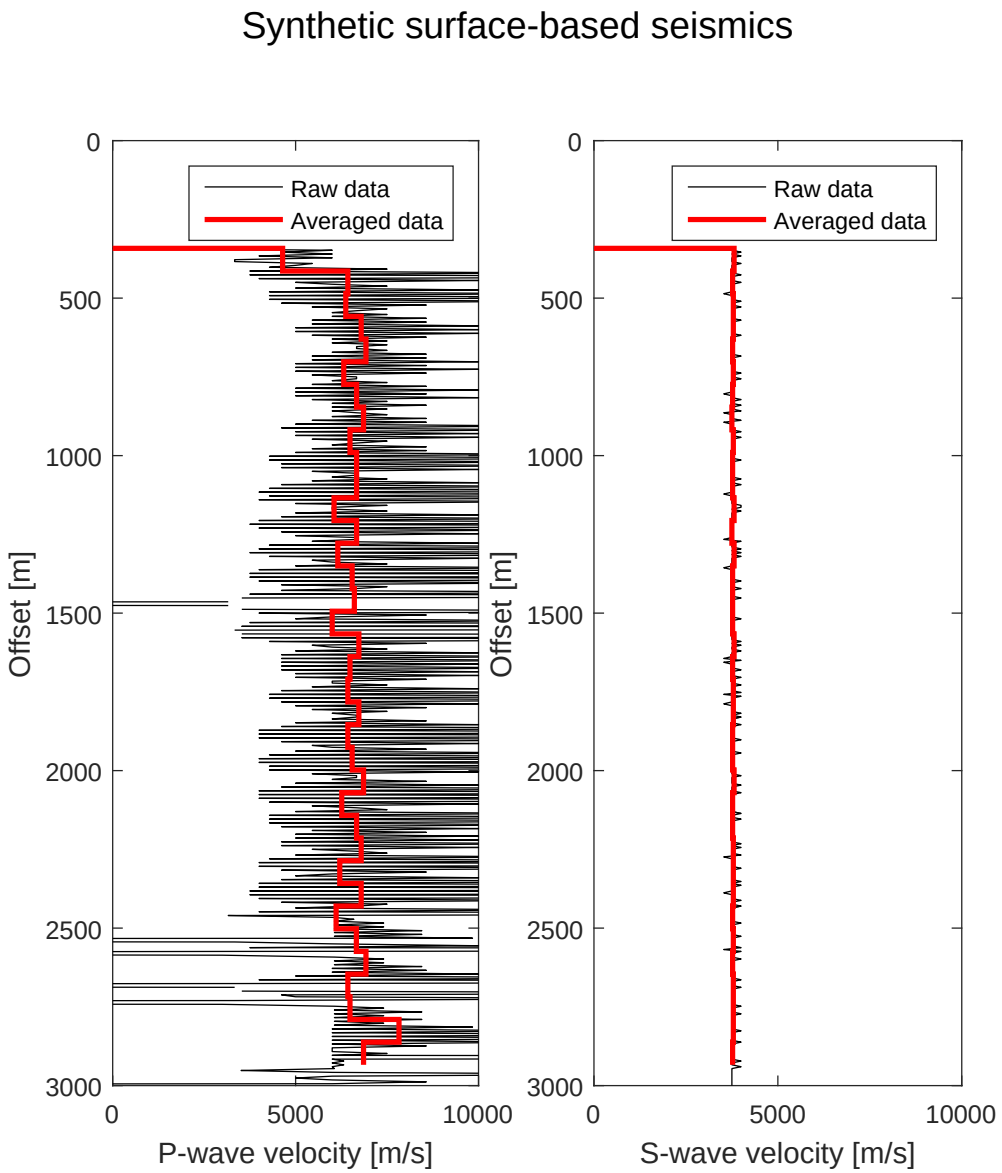

Figure B-4: Synthetic velocity profiles generated from the surface-based seismic acquisition. Raw data in black and interval velocity profile with offset for intervals of 8 receiver spacings in red.